UNIVERSIDADE DE SÃO PAULO

FACULDADE DE FILOSOFIA CIÊNCIAS E LETRAS DE RIBEIRÃO PRETO

Mariana Chaves Micheletto

Ativação de proteínas fotossensíveis com nanopartículas radioluminescentes e raios-X

(Activation of photosensitive proteins with radioluminescent nanoparticles and X-rays)

Ribeirão Preto

2023

MARIANA CHAVES MICHELETTO

Ativação de proteínas fotossensíveis com nanopartículas radioluminescentes e raios-X

Versão Corrigida

Tese apresentada ao Departamento de Física da FFCLRP-USP como parte das exigências para obtenção de título de Doutora em Ciências.

Área de concentração: Física Aplicada a medicina e Biologia

Orientador: Antonio José da Costa Filho

Coorientador: Éder José Guidelli

Ribeirão Preto

2023

Ficha Catalográfica

Mariana Chaves Micheletto

Ativação de Proteínas Fotossensíveis com Nanopartículas Radioluminescentes e Raios-X, Ribeirão Preto, 2023. 98 p.

Tese de doutorado apresentada à Faculdade de Filosofia Ciências e Letras de Ribeirão Preto/USP – Área de concentração: Física Aplicada a Medicina e Biologia.

Janus

Universidade de São Paulo

ATA DE DEFESA

Aluno: 59135 - 6789105 - 2 / Página 1 de 1

Ata de defesa de Tese do(a) Senhor(a) Mariana Chaves Micheletto no Programa: Física Aplicada à Medicina e Biologia, do(a) Faculdade de Filosofia, Ciências e Letras de Ribeirão Preto da Universidade de São Paulo.

Aos 28 dias do mês de novembro de 2023, no(a) Bloco B2, sala 220, Física realizou-se a Defesa da Tese do(a) Senhor(a) Mariana Chaves Micheletto, apresentada para a obtenção do título de Doutora intitulada:

"Ativação de proteínas fotossensíveis com nanopartículas radioluminescentes e raios-X"

Após declarada aberta a sessão, o(a) Sr(a) Presidente passa a palavra ao candidato para exposição e a seguir aos examinadores para as devidas arguições que se desenvolvem nos termos regimentais. Em seguida, a Comissão Julgadora proclama o resultado:

Nome dos Participantes da Banca	Função	Sigla da CPG	Resultado
Antônio José da Costa Filho	Presidente	FFCLRP - USP	Não Votante
Mauricio da Silva Baptista	Titular	IQ - USP	APROVADA
Alessandro Lauria	Titular	ETH ZÜRICH - Externo	APROVADA
Koiti Araki	Suplente	IQ - USP	APROVADA
Rosangela Itri	Suplente	IF - USP	APROVADA
Adriana Fontes	Suplente	UFPE - Externo	APROVADA

Resultado Final: APROVADA

Parecer da Comissão Julgadora *

Após exposição clara pela aluna e arguição com respostas seguras, a banca considerou a aluna plenamente apta e aprovada com louvor.

Eu, Cesar Pereira Brites _____, lavrei a presente ata, que assino juntamente com os(as) Senhores(as). Ribeirão Preto, aos 28 dias do mês de novembro de 2023.

Mauricio da Silva Baptista

Alessandro Lauria

Koiti Araki

Rosangela Itri

Adriana Fontes

Antônio José da Costa Filho
Presidente da Comissão Julgadora

* Obs: Se o candidato for reprovado por algum dos membros, o preenchimento do parecer é obrigatório.

A defesa foi homologada pela Comissão de Pós-Graduação em _____ e, portanto, o(a) aluno(a) _____ jus ao título de Doutora em Ciências obtido no Programa Física Aplicada à Medicina e Biologia.

_____
Presidente da Comissão de Pós-Graduação

Dedico este trabalho a todos os bisnetos da Nilza Chaves, herdeiros de uma história repleta de perseverança e amor incondicional.

A vocês, jovens promessas, ofereço este trabalho na esperança de que ele inspire em seus corações a mesma paixão pela vida que sua bisavó. Que cada desafio enfrentado e cada triunfo celebrado neste estudo sirva para lembrá-los de que, dentro de cada um de vocês, reside a força e a sabedoria de muitas gerações e que o melhor ainda está por vir.

Agradecimentos

Durante os cinco anos em que trabalhei nesta tese de doutorado tantas coisas se passaram. E eu jamais chegaria ao fim sem o suporte de tantas pessoas que estiveram comigo nesse período. Gostaria de expressar meus mais profundos agradecimentos a todos que se envolveram e contribuíram para a realização deste projeto, direta ou indiretamente.

Primeiramente, agradeço a Deus, por me dar forças para superar os percalços e coragem para buscar sempre novos desafios.

À minha família, meu lugar de acolhimento e conforto, para onde sei que sempre posso voltar para ganhar novo folego. Em especial às mulheres: minha avó Nilza, minha mãe Rozalina e minha irmã Ana Maria que são a fonte das minhas forças e inspiração. Essas três poderosas e meu irmão Bernardo são os tijolos da minha fortaleza intercontinental.

Ao meu companheiro Felipe, que sempre me desafia e muitas vezes acreditou mais em mim do que eu mesma. Ninguém esteve mais perto de mim por essa jornada que você cujo amor e paciência foram imprescindíveis para a minha persistência e sucesso. Seu incentivo e companheirismo me catapultaram muito mais longe do que eu jamais poderia imaginar.

Agradeço ao meu cachorrinho, agora anjinho, Einstein, que foi meu companheiro de estudo desde a graduação aos dias intermináveis de pandemia; me ensinou tanto sobre doação e dedicação, e fez muita falta no meu colo durante a redação desta tese.

Ao meu orientador Jabah, que sempre incentivou seus alunos à desenvolverem o melhor de si e aproveitarem todas as oportunidades. Comigo não foi diferente e por isso cheguei tão longe. Ao meu coorientador, Éder por sua sabedoria, paciência, incentivo e dedicação à minha formação foram inestimáveis. E ao Alessandro, que me recebeu no ETH–Zurique, por me guiar no caminho do conhecimento científico, me desafiar a pensar além e por expandir meus horizontes. Aos três, expresso meu mais sincero agradecimento.

Agradeço também aos meus amigos e colegas, que partilharam comigo a jornada acadêmica nos três laboratórios em que passei, LBM, NanoDose e MMF, compartilhando ideias, conselhos e muitos momentos de solidariedade e amizade. As trocas realizadas foram um pilar fundamental na evolução deste trabalho.

A todos os outros grupos e Professores que abriram as portas de seus laboratórios para que eu pudesse desfrutar um pouco de seus recursos e conhecimentos, e contribuíram enriquecendo esta tese grandemente.

À Faculdade de Filosofia, Ciências e Letras de Ribeirão Preto e à FAMB.

À Nilza pelos salvamentos e Dona Fátima pela limpeza e conversas inspiradoras.

Às agências de fomento tão fundamentais para o desenvolvimento deste projeto CNPq, CAPES e especialmente a FAPESP através dos processos 2018/13016-6 e 2021/12632-8.

Por fim, agradeço a todos que, de alguma maneira, contribuíram para a realização deste trabalho. Cada um de vocês ocupa um lugar especial nesta jornada e no meu coração. Este é um feito de muitos, e sou imensamente grata por ter vocês ao meu lado.

Obrigada!

"Não se pode tornar alguém grandiloquente que fica deprimido porque seu trabalho não resultou na queda do capitalismo. Como disse uma vez a alguém, é como se fosse uma formiga atravessando a estrada com muitos caminhões passando, não dá para ficar deprimido! Como ser humano, você tem de entender que está em uma escala diferente das coisas sobre as quais escreve. E todos nós encontramos motivos para rir e amar."

(Arundhati Roy – entrevista ao El país, 2020)[1]

"If science is to yield technological benefits, history shows that we need a robust enterprise of basic, *un*directed science, in addition to more practically oriented research and development. Dwindling regard — and shrinking resources — for basic science today may well threaten our chances at moonshots in the future."

(M. Anthony Mills and Mark P. Mills – The Science Before the War, 2020)[2]

Resumo

Ativação de proteínas fotossensíveis com nanopartículas radioluminescentes e raios-X

A terapia fotodinâmica (PDT) é tradicionalmente limitada devido à baixa penetração da luz ultravioleta-visível (UV-vis) nos tecidos humanos. No entanto, tecnologias avançadas permitem a excitação de fotossensibilizadores (PS) em diferentes comprimentos de onda, oferecendo oportunidades para a descoberta de cintiladores compatíveis. Um complexo mais eficiente de nanopartículas e fotossensibilizadores pode ser projetado através de um entendimento mais completo das propriedades de cada componente do sistema. Esta pesquisa foca na aplicação inovadora dos raios-X como uma alternativa à luz UV-vis para uma excitação mais profunda de tumores na PDT. Nanopartículas cintilantes (ScNP) são necessárias como intermediárias para converter a energia dos raios-X em luz visível. O papel de PS é cumprido por proteínas geneticamente codificadas. Exploramos a interação das proteínas eGFP, KillerOrange e KillerRed com ScNP de $LaF_3:Tb^{3+}$ em termos de suas propriedades físico-químicas e de transferência de energia, enquanto também investigamos a estrutura, estabilidade e função de tais proteínas em condições fisiológicas adversas e sob irradiação de raios-X. Em um segundo sistema de interesse do projeto, dopamos nanopartículas de Óxido de Háfnio (HfO_2) com titânio (Ti) para realçar suas propriedades de luminescência e criamos uma dispersão estável em tampão PBS. Para estabilizar as nanopartículas em PBS, revestimo-las com ácido cítrico (CA). Como PS neste caso, usamos a proteína miniSOG com seu C-terminal modificado pela inserção de uma sequência de glutamatos (E), formando miniSOG-PolyE. A sequência de PolyE procurou mimetizar a interação do CA com as nanopartículas de HfO_2. As proteínas exibiram estabilidade sob condições severas experimentadas durante as terapias do câncer. A caracterização biofísica das proteínas, combinada com testes usando radiação ionizante, revelou uma interação mínima da proteína com raios-X. Demonstramos a transferência de energia de ScNP para eGFP, KO, e KR. O sistema constituído por eGFP, KO and KR conjugadas às nanopartículas de $LaF_3:Tb^{3+}$ se mostrou eficiente na prevenção do crescimento de culturas bacterianas, provavelmente via geração de espécies reativas de oxigênio. A modificação genética que resultou na miniSOG-PolyE aumentou a ligação com a nanopartícula de HfO_2 e estabilizou a dispersão coloidal em ambientes semelhantes aos sistemas biológicos. Propomos esses sistemas como vias promissoras para o uso de PS codificados geneticamente em aplicações de PDT com raios-X. Pesquisas adicionais sobre este tema podem abrir caminho para terapias contra o câncer mais eficazes e esclarecer sobre a interação de nanopartículas cintilantes e proteínas para criar um nanocomposto conjugado com maior estabilidade na dispersão em meios biológicos.

Palavras-chave: Fotossensibilizadores geneticamente codificados. Nanopartículas cintilantes. Irradiação de raios-X. Terapia fotodinâmica. Tratamento do câncer.

Abstract

Activation of photosensitive proteins with radioluminescent nanoparticles and X-rays

Photodynamic therapy (PDT) is traditionally limited due to the poor penetration of ultraviolet-visible (UV-vis) light in human tissues. However, advanced technologies allow the excitation of photosensitizers (PS) at different wavelengths, providing opportunities to discover compatible scintillators. A more efficient complex of nanoparticles and photosensitizers can be designed through a further understanding of the properties of each component of the system. This research focuses on the innovative application of X-rays as an alternative to UV-vis light for deeper tumor excitation in PDT. Scintillating nanoparticles (ScNP) are required as intermediates to convert the energy of X-rays into visible light. The role of PS is fulfilled by genetically encoded proteins. We explore the interaction of the eGFP, KillerOrange, and KillerRed proteins with ScNP $LaF_3:Tb^{3+}$ in terms of their physicochemical properties and energy transfer, while also investigating the structure, stability, and function of such proteins under adverse physiological conditions and X-ray irradiation. In a second system of project interest, we doped Hafnium Oxide (HfO_2) nanoparticles with titanium (Ti) to enhance their luminescence properties and created a stable dispersion in PBS buffer. To stabilize the nanoparticles in PBS, we coated them with citric acid (CA). As the PS in this case, we used the miniSOG protein with its C-terminal modified by the insertion of a glutamate (E) sequence, forming miniSOG-PolyE. The proteins exhibited stability under harsh conditions experienced during cancer therapies. Biophysical characterization of the proteins, combined with tests using ionizing radiation, revealed minimal protein interaction with X-rays. We demonstrated the energy transfer from ScNP to eGFP, KO, and KR. The system consisting of eGFP, KO, and KR conjugated to $LaF_3:Tb^{3+}$ nanoparticles proved efficient in preventing bacterial culture growth, likely through the generation of reactive oxygen species. The genetic modification that resulted in miniSOG-Poly-E increased the binding with the HfO_2 nanoparticle and stabilized the colloidal dispersion in environments similar to biological systems. We propose these systems as promising pathways for the use of genetically encoded photosensitizers in PDT applications with X-rays Further research on this topic could pave the way for more effective cancer therapies and shed light on the interaction of scintillating nanoparticles and proteins to create a conjugated nanocomposite with greater dispersion stability in biological media.

Keywords: Genetically encoded photosensitizer. Scintillating nanoparticles. X-ray irradiation. Photodynamic therapy. Cancer treatment

List of figures

List of tables

Abbreviations and Acronyms

$^1O_2$	Singlet oxigen
AFM	Atomic force microscopy
ATR	Attenuation total reflection
CA	Citric acid
CD	Circular dichroism
CFU	Colony-forming units
DLS	Dynamic light scattering
DSC	Differential scanning calorimetry
FMN	Flavin mononucleotide
FRET	Förster resonance energy transfer
FTIR	Fourier transform infrared
GFP	Green fluorescent protein
IR	Infraredra
KO	Killer orange
KR	Killer red
LOV	Light, oxygen, and voltage
miniSOG	Mini–singlet oxygen generator
NIR	Near infrared
OD	Optical density
PAGE	Polyacrylamide gel electrophoresis
PBS	Phosphate-buffer saline
PDI	Polydispersity
PDT	Photodynamic therapy
PE	Poly glutamate
PL	Photoluminescence
PLE	Photoluminescence excitation
PS	Photosensitizers
RET	Resonance energy transfer
ROS	Reactive oxygen species
ScNP	Scintillating nanoparticles
SEM	Scanning electron microscopy
SOSG	Singlet oxygen sensor green
TEM	Transmission electron microscopy
TGA	Thermogravimetric analysis
UV	Ultraviolet
Vis	Visible
XRD	X-ray diffraction

List of manuscript published during the Ph.D.

EVANGELISTA, NATHAN N.; **MICHELETTO, MARIANA C.**; MENDES, LUÍS F. S.; COSTA-FILHO, ANTONIO J..Biomolecular condensates of Chlorocatechol 1,2-Dioxygenase as enzymatic microreactors for the degradation of polycyclic aromatic hydrocarbons. BioRxiv, p. 2023.05.29.542454, 2023.

FERREIRA, ISABELLA N.; ISIKAWA, MILENE M.; NUNES, LUIS H. S., **MICHELETTO, MARIANA C.**, GUIDELLI, ÉDER J.. Magnetic Nanoparticles Covered with Polycyclic Aromatic Hydrocarbons as Singlet Oxygen Carriers for Combining Photodynamic Therapy and Magnetic Hyperthermia. Journal of Photochemistry and Photobiology A: Chemistry, v. 444, p. 114902, 2023.

MENDES, LUÍS F. S.; BATISTA, MARIANA R. B.; KAVA, EMANUEL; BLEICHER, LUCAS; **MICHELETTO, MARIANA C.**; COSTA-FILHO, ANTONIO J.. Resurrecting Golgi proteins to grasp Golgi ribbon formation and self-association under stress. International Journal of Biological Macromolecules, v. 194, p. 264-275, 2022

MICHELETTO, MARIANA C.; GUDELLI, ÉDER J.; COSTA-FILHO, ANTONIO J.. Interaction of Genetically Encoded Photosensitizers with Scintillating Nanoparticles for X-ray Activated Photodynamic Therapy. ACS Applied Materials & Interfaces, v. 13, p. 2289-2302, 2021

Contents

Chapter 1 – Introduction and scope of the thesis

The emergence of photomedicine is directly linked to the beneficial/harmful interactions of nonionizing electromagnetic radiation with living organisms. The absorbed radiation excites chromophores' molecules, leading to specific physicochemical perturbations in the neighbouring biomolecules. Therefore, the controlled use of UV and visible radiation offers the possibility of selecting specific target molecules and causing a specific/desired effect[3]. The desired effects can be used for diagnostic or therapeutic purposes. The therapeutic applications of light date back thousands of years when plants were used to enhance the healing effects of light in ancient Egypt and India. It was only in the late twentieth century that photomedicine had its technology leveraged due to a demand for effective and less invasive treatment[4, 5]

Advancements in optical tools have expanded the applications of photomedicine. Technologies like optical coherence tomography[6], super-resolved fluorescence microscopy[7], multiphoton microscopy[8], photoacoustic scanning microscopy[9], and confocal micro-Raman spectroscopy[10] have emerged as powerful tools for research and diagnostics, utilizing light as an information carrier[11]. In clinical practice, light is utilized as an energy carrier through the photothermal and photodynamic effects[11, 12]. Photodynamic therapy (PDT) has become an alternative treatment modality for cancer, skin diseases, and various types of infections[13, 14]. Additionally, the increasing focus on beauty care has contributed to the relevance and popularity of photomedicine[13].

Recent advances in biomedical optics have allowed for integrating photonics with nanotechnology[15], biomaterials[16, 17], and genetic engineering[18, 19]. Nanomaterials for photothermal therapy[20] have also been a subject of great interest, as they enable minimally invasive and selective treatment. The continuous development of optical technology is expected to impact the progress of biomedical research.

1.1 Photodynamic Therapy (PDT)

Drug resistance is a global threat that reduces the effectiveness of medications for antimicrobial and antineoplastic drugs[21] and is a significant challenge to healthcare development[22]. In this sense, PDT is an alternative to inducing oxidative stress simultaneously to various vital molecules and structures such as proteins, nucleic acids, and phospholipids. However, the substantial damage caused by oxidative stress raises the question of whether any

cell (e.g. cancerous, bacteria, or plasmodium) could develop a resistance mechanism[23, 24]. Nevertheless, PDT-resistant cell lines have never been isolated *in vivo*, and the magnitude of resistance developed *in cell* lines *in vitro* is usually less than that reported for drug-resistant cells. Furthermore, no cross-resistance between PDT and chemotherapy has been reported[25].

The PDT treatment involves the administration of a photosensitizer (PS), followed by its illumination with UV–visible light. The PS absorbs the light and produces reactive oxygen species (ROS), such as singlet oxygen, that cause cell. The cytotoxicity results from combining the two agents (PS and light), keeping the PDT damage locally rather than systemically. Thus, PDT is a minimally invasive treatment and can be applied even in elderly and immune-depressed people[26].

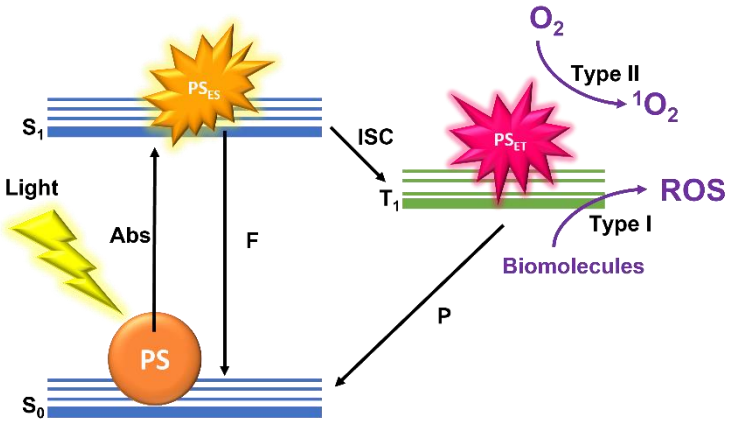

Figure 1: Schematic Jablonski's diagram showing PDT's mechanism of action. Following light absorption (Abs), the photosensitizer (PS) reaches an excited singlet state (S_1) from the ground singlet state (S_0). The return of the excited singlet PS state (PS_{ES}) to S_0 results in fluorescence (F). Alternatively, the PS_{ES} transitions to a triplet excited state (T_1) through an intersystem crossing (ISC). The PS in a triplet excited state (PS_{ET}) can return to S_0 by phosphorescence (P) or reacting with neighbour molecules. Figure adapted from ref. [28].

A schematic of the photosensitization process can be seen in **Figure 1**, where the PS in its electronic singlet ground state (S_0) can reach an excited singlet state (S_1) upon illumination with radiation at an appropriate wavelength. The excited singlet state is characterized by a short lifetime, and, in general, the PS can return to its basal state by emitting the absorbed energy via fluorescence (F) or by transitioning to a triplet excited state (T_1) through intersystem crossing (ISC). Although this is a spin-forbidden transition, an adequate photosensitizer presents a high yield of triplet states[27]. Once in the triplet state, the PS can return to the ground state either by transferring an electron (type I reaction) or energy (type II reaction) to neighboring molecules (water, biomolecules, or oxygen), thus producing ROS (Figure 1). Type I reactions generate

radical and radical anion species (e.g. $O_2^{\bullet-}$, $HO^{\bullet}$), while type II reactions produce singlet oxygen ($^1O_2$). These two competing mechanisms can occur simultaneously, leading to an enhanced PDT response[27]. From the triplet excited state, the PS can also return to the ground state by phosphorescence (P).

1.1.1 Genetically encoded photosensitizer

Photoreceptor proteins are light-sensitive proteins involved in various physiological processes found in nature, such as phototropism, regulation of the circadian cycle, photoperiodism, photosynthesis, vision processes, DNA damage, and bacterial bioluminescence[29, 30]. These photoreceptors allow organisms to adjust their biological functions to light signals. The photoactivation potential of photoreceptors and the frequently observed reversibility of induced structural changes are strong experimental advantages, allowing various studies using time-resolved methods and the application of various spectroscopic techniques[31]. In biomedical sciences, several non-toxic photoreceptors have contributed to advancements in obtaining *in vivo* imaging through different non-invasive labeling methods of cells, organelles, and even other proteins, monitoring their movement inside the cell and trafficking between organelles. Phototoxic fluorescent proteins have been employed for a different purpose to damage target molecules in restricted locations and after photoactivation[29, 30, 32, 33]. Furthermore, the development of advanced techniques in genetic engineering has enabled site-specific alteration of photoreceptors, changing their absorption bands, energy conversion pathways, and other biophysical properties[33].

In this project, we proposed using some phototoxic proteins as PSs. Ideally, the PS should have low levels of cytotoxicity in the dark, preferential accumulation in the target cells, and present no physiological side effects. Also, the drug clearance from the patient should be fast so that the patient is not required to stay in the dark for a long time after the treatment[28]. PDT typically utilizes chemically synthesized cyclic tetrapyrrole molecules as PSs administered topically or intravenously. Due to the low accumulation in the tumor tissues, some PSs have been modified with targeting agents (such as antibody conjugation) or encapsulation into carriers (such as liposomes, micelles, and nanoparticles) to enhance accumulation at the target site[28].

Moreover, when considering an agent for therapeutic purposes, an immediate question arises regarding how to deliver these agents to the target tissue. In the case of proteins, delivery

can be indirectly achieved through the genetic material encoding them. In other words, considering the precise delivery of viral vectors to solid tumors, phototoxic proteins could work as intrinsically generated PS, allowing light-induced tumor destruction[34, 35].

In general, genetically encoded PS have a reduced yield of reactive oxygen species generation compared to other PS[36]. On the other hand, the main advantages of using genetically encoded proteins over synthetic PS are their exclusive expression in the tumor cells and the direct killing of cells through precise damage to the target cell compartment. The damage occurs because, depending on the subcellular location and the dose of UV-vis radiation, reactive oxygen species produced by the PS can lead to a variety of outcomes, ranging from inactivation of partner proteins, DNA damage, mitotic process blockade to cell death[34, 37]. Thus, the intracellular localization of a target PS not only affects the cytotoxic effect but also determines the cell death mechanism, leading to death by apoptosis when PS localizes to the mitochondria and necrosis when it localizes to the membrane[38, 39]. In this context, the discovery and development of phototoxic proteins enable the use of genetically encoded PS, increasing the treatment's specificity.

1.1.2 X-ray as energy source

PDT can be, and generally is, combined with one or more therapies, effectively minimizing side effects while maximizing the benefits of each treatment regimen. For example, combining PDT and chemotherapy reduces the likelihood of tumor recurrence[35]. Other examples of treatments combined with PDT are radiotherapy[40], ultrasound[41], and hyperthermia[42]. However, the limited penetration depth of UV-vis light into the human body restricts the scope of photomedicine applications.

The application of PDT is currently limited to peripheral and endoscopically accessible regions of the human body. Considering the limitations of monotherapy, combining strategies holds promises for clinical applications. The particular combination of PDT with radiotherapy is a powerful strategy in the fight against cancer. In contrast to the effects of UV and visible light on the specific target molecules, high-energy photons, such as X-rays, interact with human tissue and any other matter by relatively indiscriminate ionization of molecules. The highly reactive ionized molecules and chemical bonds may be broken or formed. However, since the absorption is relatively nonspecific, the selection of the target molecules is limited[43]. X-rays have deep penetration in the human body precisely due to the low interaction selectivity.

Since most PS (proteins or regular ones) have high extinction coefficients only in the UV–vis region, X-ray sensitizers generally comprise traditional PS and scintillating nanoparticles (ScNP)[44, 45]. The ScNPs are responsible for the X-ray energy conversion to the respective absorption wavelength of the PS, thus promoting its excitation (**Figure 2**). Consequently, the light emitted by nanoparticles could sensitize the appropriate photoreceptors. Moreover, using nanoparticles with high effective atomic numbers can increase the cross-section for X-ray interaction around the treated region at the expense of the surrounding healthy tissue[46]. With this methodology, we change the scale from macroscopic to microscopic damage control level, in addition to meeting the critical and immediate need for less invasive and deeper applications of PDT. Besides, the application of X-rays as a light source is explored in deep tumor therapy and the integration of diagnostics and therapy for theranostics. In this unique approach, not only can the tumor cure rate be increased, but the radiation dose and radiotherapy side effects can also be decreased.

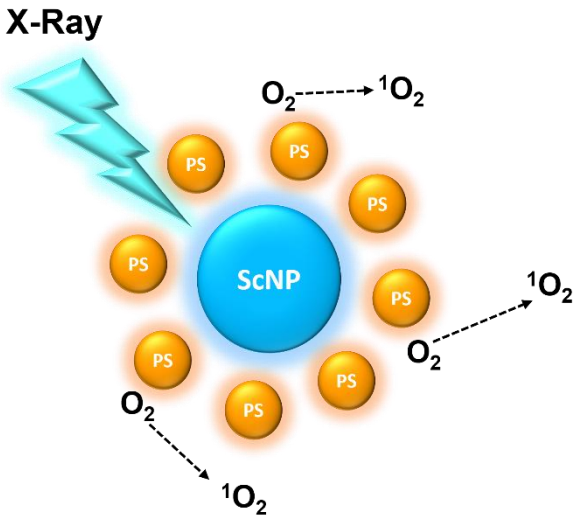

Figure 2: Schematic scintillating nanoparticles (ScNP) covered with photosensitizers (PS). The ScNP absorbs the X-ray high energy and converts it to the visible region, hence exciting the PSs.

It should be noted that X-ray stimulation is considered feasible and safe, given the extensive research on X-ray luminescence imaging in preclinical application[47, 48].

1.1.3 Scintillating Nanoparticles

To perform X-ray excited PDT (X-PDT), X-rays need to be converted into visible light. The scintillation of nanoparticles arises from the excitation of an electron through the absorption of ionizing radiation, where relaxation to the ground state results in luminescence.

Among a list of ScNP[47], lanthanide-doped nanophosphors are an example of nanoparticles that have received significant attention for biological detection and imaging due to their unique optical properties[49-51]. The development of lanthanide-doped nanophosphors that operate in the near-infrared spectral range (NIR - 650-900 nm), ideal for optical transmission through biological tissues, has attracted great interest for *in vivo* bioimaging probes[52-54]. Alternatively, high-energy radiation used in medical imaging modalities such as X-ray computed tomography (CT) or positron emission tomography (PET) can also excite ScNP[49]. ScNPs have been proposed as molecular imaging probes in developing combined X-ray/optical imaging modalities, such as X-ray luminescence computed tomography (XLCT)[55-57]. This innovative imaging technique provides deep tissue penetration and tissue autofluorescence, simplifying imaging through optical reconstruction from planar images[49].

Furthermore, it has been shown that through molecular targeting strategies, the accumulation of ScNPs in specific tissues is possible[58-60]. The synthesis of poly(ethylene glycol) (PEG)-coated ScNPs enables the localization of lesions, such as tumors, by detecting X-ray-induced luminescence. ScNPs can also be activated by radioisotopes, allowing optical detection in radiotherapy or simultaneous molecular target localization. In summary, these nanoparticles can serve as optical probes excited by X-rays or radioisotopes[49].

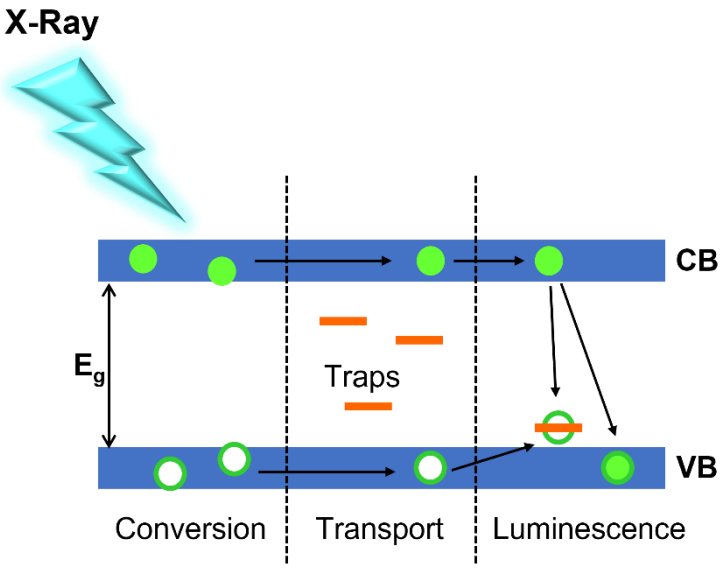

Figure 3: Simplified scheme of the three main stages of the scintillation process. During the *Conversion* stage, the X-ray energy is converted in electrons (solid circles) and holes (hollow circles). In the *Transport* stage, the electrons and holes migrate through the conduction band (CB) and valence band (VB), respectively. *Luminescence* occurs when an excited emitting centre releases its energy by emitting a photon or via non-radiative processes.

The scintillation process, outlined in **Figure 3**, starts with converting the incoming radiation into a large number of electron–hole pairs in the scintillating nanostructure. When the electron energies become less than the ionization threshold, electrons thermalize to the bottom of the conduction band and holes to the top of the valence band. The electrons and holes can remain free or combine to form free or self-trapped excitons. Subsequently, the energy must migrate before transferring to a luminescence centre. The speed and efficiency of the scintillation process are influenced by the properties of the energy carriers[61]. Finally, the electron–hole pairs' energy transfer to luminescent ions leads to emission via luminescence after relaxation. Repeated trapping at defects in the material may occur, and energy losses are probably due to nonradiative recombination and other mechanisms[62].

After the conjugation of PS and ScNP, the energy from the ScNPs can activate the nearby PS either by Förster resonance energy transfer (FRET) or by trivial energy transfer. FRET occurs when the dipolar moments of a donor and acceptor are coupled, provided they are in close proximity (typically 1-10 nm) and their emission and absorption spectra overlap significantly (**Figure 4**). While the trivial energy transfer occurs through separate events of donor emission and acceptor absorption[63], considering the ScNP as the donor and the PS as the acceptor. Many inorganic nanomaterials like oxides, fluorides, silica-based nanostructures, and semiconductor nanocrystals have been combined with organic PS[64].

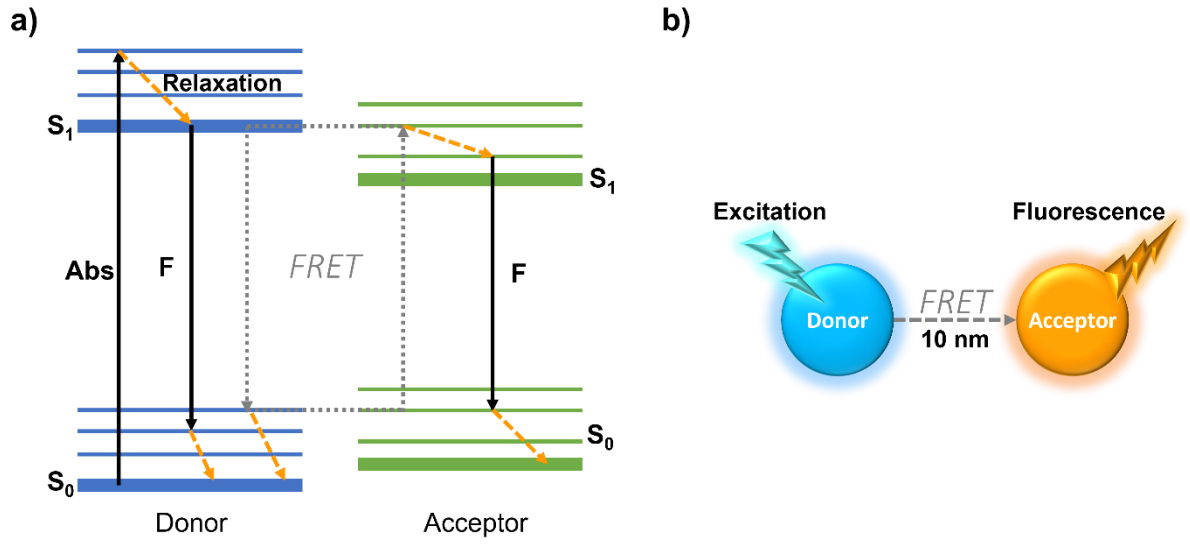

Figure 4: a) A donor chromophore, initially in its electronic excited state, may transfer energy to an acceptor chromophore through nonradiative dipole-dipole coupling. b) The overlapping of the donor emission and the acceptor excitation energies is necessary for the FRET as well as the proximity between donor and acceptor. The efficiency of this energy transfer is inversely proportional to the sixth power of the distance between donor and acceptor, making FRET extremely sensitive to small changes in distance.

1.2 Scope of this thesis

As discussed throughout this introduction, PDT is a captivating technic that merges the powers of light and chemistry to combat disease. It is a targeted approach that offers immense potential in treating various conditions. With its ability to be precisely controlled and localized, PDT stands as a promising alternative or complement to traditional treatment methods. Besides, the discovery and development of phototoxic proteins able to produce ROS allowed the employment of genetically encoded PS as light-activated devices. Light-induced generation of ROS by chromogenic compounds has been used for single-molecule inactivation and cell killing[34].

In this context, miniSOG, KillerOrange, and KillerRed are proteins with a high quantum yield for singlet oxygen generation upon exposure to visible light that had their properties explored in this thesis. Their true potential for *in vivo* applications has been hindered by the limited penetration of UV-visible light into biological tissues. By utilizing ScNP such as HfO_2 and $NaLuF_3$:Tb, we have discovered a way to convert X-ray energy to UV-vis, bridging the gap between these two spectra. Even though ScNPs have been proven effective for imaging purposes, many parameters must be optimized to achieve the desired treatment results. In this thesis, we documented the investigation of the properties that guide the interaction between the proteins and ScNP mentioned above regarding their physicochemical and energy transfer properties. The protein structure, stability, and function were evaluated upon adverse physiological conditions and X-ray irradiation. Optimal parameters for energy transfer from ScNP to the proteins were investigated, paving the way for using genetically encoded photosensitizers for X-PDT applications.

More specifically, as an innovative proposal, this project aimed to use proteins as PS to evaluate the feasibility of X-PDT at the molecular level, considering the necessary conditions for future *in vivo* applications. It was divided into three fronts:

1. *Protein production and characterization:* Proteins with broad potential for biomedical applications, such as miniSOG, GFP, KillerOrange, and KillerRed have been chosen as study targets. First, we implemented heterologous expression methods in bacterial systems. Then, these proteins underwent structural characterization and thermal stability assays using biophysical techniques such as circular dichroism, differential scanning calorimetry, and other spectroscopies. The light intensity required for chromophore sensitization

and consequent activation of the photoreceptors, lifetime, and efficiency in ROS production were determined.

2. *Nanoparticle production and characterization:* Scintillating nanoparticles covering the entire visible spectrum (blue to red) as HfO2 and LaF_3:Tb were synthesized using solvothermal methods and hot-injection, respectively. The ScNP where characterised regarding their structure, morphology, dispersion, and optical properties.
3. *Characterization of nanoparticle-photoreceptor systems:* The system as a whole was tested, evaluating the ScNP-protein bound stability, the energy transfer efficiency, and the cytotoxicity in *E. coli* upon X-ray irradiation.

Chapter 2 – Interaction of Genetically Encoded Photosensitizers with Scintillating Nanoparticles for X-ray Activated Photodynamic Therapy

Abstract

Photodynamic therapy (PDT) applications are limited by the low penetration of UV−visible light into biological tissues. Considering X-rays as an alternative to excite photosensitizers (PS) in a deeper tumor, an intermediate particle able to convert the X-ray energy into visible light (scintillating nanoparticle, ScNP) is necessary. Moreover, accumulation of PS in the target cells is also required. Genetically encoded proteins could be used as a photosensitizer, allowing the exclusive expression of PS inside the tumor cells. Here, the interaction of eGFP, KillerOrange, and KillerRed proteins with LaF3:Tb^{3+} ScNP was investigated, for the first time, in terms of its physicochemical and energy transfer properties. The protein structure, stability, and function were evaluated upon adverse physiological conditions and X-ray irradiation. Optimal parameters for energy transfer from ScNP to the proteins were investigated, paving the way for using genetically encoded photosensitizers in X-ray-activated photodynamic therapy applications.

Based on the manuscript published in ACS Applied Materials & Interfaces 2021.[65]

DOI: 10.1021/acsami.0c19041

2.1 Introduction

Genetically encoded PS are proteins that trigger cellular toxicity when exposed to light. Within this category of optogenetic tools, toxicity typically arises from ROS produced upon light absorption by a specific aromatic component within the protein structure, known as the chromophore[66]. Genetically encoded photosensitizers can be classified into two groups based on the origin of their chromophores: those belonging to the green fluorescent protein (GFP) family, which generate their chromophores through autocatalytic processes, and those that bind external ubiquitous cofactors (such as flavins) as chromophores. Both groups have found successful applications in biological research, including cell population ablation[67-69], target protein inactivation, activating signalling cascades through ROS[70], and serving as tags for electron microscopy[66, 71].

Each group presents distinct advantages and disadvantages. Proteins with exogenous chromophores primarily generate singlet oxygen, leading to higher phototoxicity[72]. However, since they rely on the presence of cofactors, these proteins may not always function effectively in tumours or specific cellular compartments[73]. In contrast, GFP-like phototoxic fluorescent proteins do not encounter these limitations but generally exhibit lower phototoxicity levels[66]. During the Ph.D., we studied the application of both PS protein groups, and in this chapter, we are focusing on the GFP family.

GFP was discovered by Osamu Shimomura in the 1960s[74]. Later, in 1988, Martin Chalfie succeeded in colouring six individual cells that could then be tracked by inserting the GFP gene into then[75]; while, in 1990, Roger Y. Tsien elucidated how GFP produces its shimmering light, and his team succeeded in varying the colour of the light so that different proteins and multiple simultaneous biological processes could be tracked[76]. The combination of these works leveraged GFP as an important tool for studying biological processes *in cells*[77] and rendered the three scientists the Nobel Prize in Chemistry in 2008.

Since its discovery from *Aequorea victoria*[74] and subsequent use as a genetic protein tag[75], protein engineering has enhanced GFP folding efficiency, stabilized protein structure in physiological conditions, and controlled its excitation and emission wavelength[78]. One of the first engineered versions of wild-type GFP was enhanced GFP (eGFP)[79, 80], which is still one of the most widely utilized GFP variants[81]. Due to its importance and luminescent properties, eGFP is one of the proteins involved in this work. Along with eGFP, the photosensitizer protein variants KillerRed (KR) and KillerOrange (KO) were also studied.

The chromophore of eGFP is buried deeply inside a protein β-barrel and shielded from the surrounding solvent (**Figure 5a**), explaining its much lower level of phototoxicity compared to small organic dyes[32, 82]. However, in KR, the β-barrel structure maintains a path through the protein that reaches the chromophore and is accessible by the water and oxygen molecules[83, 84]. KR was designed by Bulina *et al*. from the jellyfish chromoprotein anm2CP by directed evolution[38], and it was the first genetically encoded photosensitizer reported. KR protein stands out for its remarkable phototoxicity, exceeding at least 1,000 times that of other fluorescent proteins[38]. According to the literature, KR undergoes Type I and Type II reactions to generate ROS[36, 85]. GFP and KR form an intrinsic chromophore through cyclization and oxidation of SYG, and QYG, respectively (**Figure 5b**)[86, 87]Additionally, few mutations in KR, including the exchange of chromophore-forming tyrosine for a tryptophan (Y66W), resulted in KO with the chromophore formed by the sequence QWG (**Figure 5b**). KO was the first reported GFP family protein in which the chromophore is formed by a tryptophan residue[83]. This mutation causes chromophore structure changes that shift the absorption and emission wavelengths to higher energies without significantly affecting their toxicity, compared to KR. The mechanism of oxidative production for KO is thought to be the same as for KR, but further characterization is still necessary.

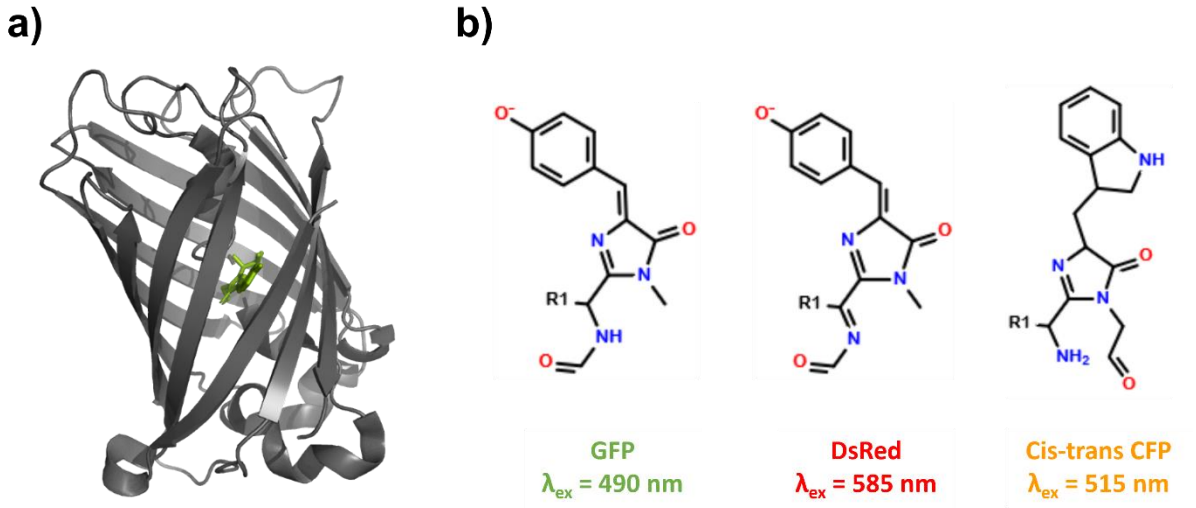

Figure 5: a) eGFP structure (PDB ID 3EVP). b) Chromophore of the proteins eGFP (GFP), excited at 490 nm; KR (DsRed), excited at 585 nm and KO (Cis-trans CFP), excited at 515 nm.

The three proteins mentioned above are excited at different wavelengths, covering the visible spectrum from blue to red. In this sense, using Terbium (Tb) as a scintillator perfectly matches our purpose due to its wide possibility of overlapping excitation/absorption wavelength for donor–acceptor energy transfer. Under UV or X-ray irradiation, Tb^{3+} has four intense

luminescence emission peaks (489, 543, 584, and 620 nm), corresponding to the $^5D_4 \rightarrow {}^7F_j$ (j = 3−6) transitions (**Figure 6**)[88, 89]. Lanthanide ions also have typically long emission lifetimes, in the order of $10^{-4} - 10^{-3}$ s, which is desired for enhanced energy transfer[90, 91]. Besides their excellent luminescent properties, lanthanides are high-Z elements. In cancer therapy, X-ray-activated high-*Z* nanoplatforms have been demonstrated to increase local dose deposition and enhance the clinical efficacy of X-ray radiation[92-94]. In this framework, we have reported, for the first time, the successful use of $LaF_3:Tb^{3+}$ ScNP as a mediator for transferring energy from X-rays to three different genetically encoded PS.

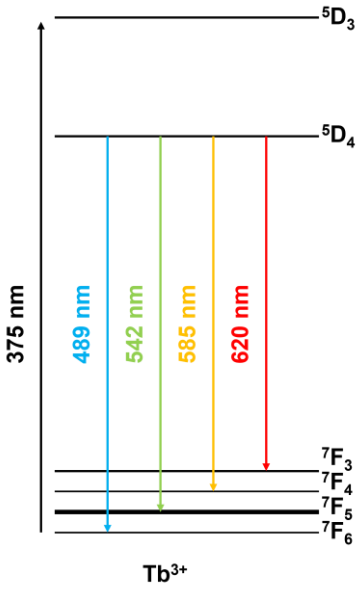

Figure 6: Partial energy level diagram of trivalent terbium ion and the emission wavelength during depopulation of $^5D_4$.

2.2 Methods

2.2.1 DNA Constructs and Heterologous Expression

The original DNA encoding the protein eGFP, KO, and KR were in pWaldo-GFPe and pQE-30 vectors, respectively. All DNA sequences were cloned into the pET28a vector using standard protocols. The restriction enzymes used were BamHI and HindIII for eGFP, and BamHI and EcoRI for KO and KR. The results were checked by DNA restriction analyses and automatic DNA sequencing. Recombinant proteins were expressed in *E. coli* Rosetta (DE3) cells. Bacterial cells were grown at 37 °C in LB medium containing kanamycin (50 µg/ mL), and cultures were induced at OD 0.8 with isopropyl-β-D-thiogalactopyranoside (0.5 mM) and

incubated for an additional 16h at 20 °C. The cells were harvested by centrifugation, and the pellets were stored at −80 °C prior to use. The cells were resuspended in PBS and lysed by sonication. Insoluble material was removed by centrifugation (11000g for 25 min at 8 °C). Recombinant proteins were loaded on to Ni-NTA superflow columns (QIAGEN) previously equilibrated with buffer and eluted in imidazole (15 mL, 500 mM). The remaining contaminants and imidazole were removed by size exclusion chromatography onto a Superdex 75 10/300 GL gel filtration column (GE Healthcare Life Sciences). Proteins were concentrated using an Amicon Ultra-15Centrifugal Filter with an NMWL of 10 kDa (Merck Millipore). The quality of the purified proteins was checked by SDS-PAGE.

2.2.2 Synthesis of $LaF_3:Tb^{3+}$

Terbium-doped lanthanum fluoride nanoparticles were prepared by a thermal decomposition method, in which 207.9 mg of $La(NO_3)_36H_2O$ (Dynamics) and 55.0 mg of $Tb(NO_3)_35H_2O$ (Sigma-Aldrich) were dissolved in 19 mL of ethylene glycol (anhydrous, 99.8%) at room temperature under vacuum and, subsequently, in nitrogen atmosphere. Following a hot-injection protocol, the temperature was then increased to 194 °C when 1 mL of 2.1 mol/1 NH_4F was added to the solution. The temperature and stirring were kept for 15 min. The final dispersion was separated by centrifugation at 11000g for 30 min and then washed with 1 mL of water. The sample was then placed in a furnace for 16h at 100 °C. After that, the samples were calcined at 200, 400, and 1000 °C for an additional 8h. For the experiments performed in suspension, the $LaF_3:Tb^{3+}$ were resuspended in 2.0 mL of water with the help of ultrasound and this emulsion was kept as the stock sample. The synthesized nanoparticles were later subjected to characterization.

2.2.3 Circular Dichroism (CD)

Far-UV (190−260 nm) CD experiments were carried out on a Jasco J-815 CD spectrometer (JASCO Corporation, Japan) equipped with a Peltier temperature control and using a quartz cell with a path length of 1 mm. The experimental parameters were the following: scanning speed, 50 nm min^{-1}; spectral bandwidth, 1 nm; and response time, 0.5s. Prior to the measurements, the proteins were diluted from a high-concentration stock solution into a 25 mM sodium phosphate buffer, pH 7.4. Thermal denaturation was performed by increasing the

temperature at 1 °C/min from 20 to 95 °C. The measurements were performed with three samples for each condition.

2.2.4 Absorption Spectroscopy

Nanoparticle and protein absorption measurements were performed using an Ultrospec 2100pro UV/ visible spectrophotometer (Biochrom) in a 10 mm optical path quartz cuvette. For the experiments with pH variation, protein stock solutions were at a concentration where the dilution in any desired buffer (20 mM) was at least 20-fold. The used buffers were glycine HCl (pH 3.0), sodium acetate/acetic acid (pH 4.0), sodium phosphate (pH 5.0−8.0), or glycine NaOH (pH 9.0 and 10.0) with an incubation time of 10 min at 25 °C. The measurements were performed with three samples for each condition.

2.2.5 Steady-State Fluorescence Spectroscopy

Fluorescence was monitored using a Hitachi F-7000 fluorescence spectrophotometer (Hitachi, Japan) equipped with a 150 W xenon arc lamp. The slit widths of the excitation and emission monochromators were set at 2.5 nm for measurements with GFP and 5 nm for other measurements. The photomultiplier voltage was 700 V, and the time response 0.1 s. Excitation wavelengths were 490 nm for eGFP, 515 nm for KO, 585 nm for KR, and 385 for $LaF_3:Tb^{3+}$. All measurements were performed at 25 °C. The protein emissions were normalized by their 280 nm absorption. The measurements were performed with three samples for each condition.

2.2.6 Time-Resolved Fluorescence Spectroscopy

Time-resolved emission spectra were collected with a FluoroLog-3 Horiba Jobin Yvon spectrofluorometer (HORIBA Scientific, Japan), equipped with a phosphorimeter accessory and Xe-pulsed lamp, changing the delay time. The $LaF_3:Tb^{3+}$ excitation wavelength was 285 nm, and the luminescence lifetimes were monitored for the four Tb^{3+} peaks (489, 543, 584, and 620 nm). For variation in salt concentration experiments, the suspensions were prepared in water, PBS (NaCl 137 mM), and PBS plus 150 mM NaCl. Data analyses were performed using a nonlinear least-squares formalism inserted in Origin software (OriginLab). Data were analyzed according to the reduced-χ^2 values and the residual distribution. The measurements were performed with three samples for each condition.

2.2.7 Differential Scanning Calorimetry (DSC)

DSC experiments were performed on a Microcal VP-DSC microcalorimeter (Malvern Instruments, U.K.) in a temperature range corresponding to the thermal transitions of the protein, from 10 to 98 °C. Heating scan rates of 63.6 °C/h and 33.4 °C/h were selected to monitor protein denaturation. Instrumental buffer (PBS) baselines were recorded prior to the experiments and used for data analysis. The measurements were performed with three samples for each condition.

2.2.8 IR

(FTIR) Spectroscopy

FTIR spectra were recorded on a Shimadzu IR Prestige-21 spectrophotometer (Shimadzu, Japan) from 4000 to 400 cm^{-1}. The vibrational modes of the nanoparticles were monitored in three different stages of preparation: first, after the nucleation reaction still in suspension of ethylene glycol; second, from the sample washed with water (×4) and dried for 16 h at 100 °C; and third, after calcination for 8 h at 400 °C.

2.2.9 Thermogravimetric Analysis (TGA)

TGA curves were obtained on a Simultaneous TGA−DTA−DSC SDTQ600 (TA Instruments, France) equipment from 25 to 1300 °C with a heating rate of 10 °C/min. A nitrogen flow of 100 mL/min was applied for inert atmosphere measurements.

2.2.10 X-ray Diffraction

The nanoparticles' crystalline properties and phase identity were verified by X-ray diffraction analysis, using a D5005 diffractometer (Bruker) equipment with a graphite monochromator, employing Cu Kα radiation (λ = 0.1540 nm). A step of 0.02 s^{-1} was used in the range of $10° < 2\theta < 80°$ angular domain.

2.2.11 Transmission Electron Microscopy (TEM)

Microscopy imaging was performed on a JEM-100 CXII TEM (JEOL, Japan) equipment by drying a drop of the same sample 1,000 times diluted from the stock sample on a copper grid covered with a conductive polymer. The images were processed using ImageJ open-source software[95].

2.2.12 Dynamic Light Scattering (DLS)

The hydrodynamic radius and ζ-potential of the nanoparticles were determined by the dynamic light scattering (DLS) equipment Zeta Sizer system (Malvern Instruments, U.K.). Data were collected at a fixed angle and wavelength of 173° and 633 nm (He−Ne laser), respectively. The measurements were performed with three samples for each condition.

2.2.13 Radioluminescence

Radioluminescence measurements were performed under irradiation using an X-ray tube (Magnum−Moxtek), operating at 48 kVp and 0.2 mA. The emitted light was collected and analyzed using a fiber optic spectrometer. The X-ray dose rate at the sample position was about 9 Gy/min. With the same tube, the proteins were also irradiated with doses of 100 Gy, and their fluorescence was subsequently analyzed. For the LaF_3:Tb^{3+} protein energy transfer measurements, 100 μL of LaF_3:Tb^{3+} was aliquoted from the stock suspension and mixed with a protein volume gradient. The final volume was adjusted to 200 μL with the addition of buffer to an appropriate concentration of PBS(×1), NaCl, and imidazole. The measurements were performed with three samples for each condition.

2.2.14 Bacterial Growth

E. coli Rosetta (DE3) cells were grown at 37 °C in LB medium containing chloramphenicol (34 μg/mL) to an OD of 1.0. A small volume was diluted in 50 mL of new LB medium to the OD of 0.02 and divided into five volumes for five irradiation conditions: dark, 1.5 h and 3 h in UV-A lamp, and 25 and 50 Gy X-rays (same tube used for radioluminescence). After irradiation, bacterial growth was measured by turbidity (absorbance at 600 nm) during constant agitation at 37 °C for 16h. A Multiskan Go (Thermo Scientific, EUA) was employed.

Each sample was assayed four times, and the results were normalized according to the maximum OD. The measurements were performed with four samples for each condition.

2.3 Results and Discussions

2.3.1 Heterologous Expression and Biophysical Characterization

The heterologous expression procedure described in the experimental session resulted in high-yield expression of the three proteins (eGFP, KO, and KR). The recombinant proteins were purified using a two-step chromatography protocol from which highly purified samples (>95%, according to SDS-PAGE, **Figure 7**) were obtained. At the end of the purification, the KR and KO proteins still carried a 6×His-tag at their N terminus, and the eGFP maintained a 6×His-tag at both ends. The maintenance of the 6×His-tag at the ends of the polypeptide chains represents a coordinating motif of metal ions that can provide a binding region between the biomolecule and the nanoparticle. Protein theoretical parameters were estimated via ExPASy[96] and can be found in **Table 1**.

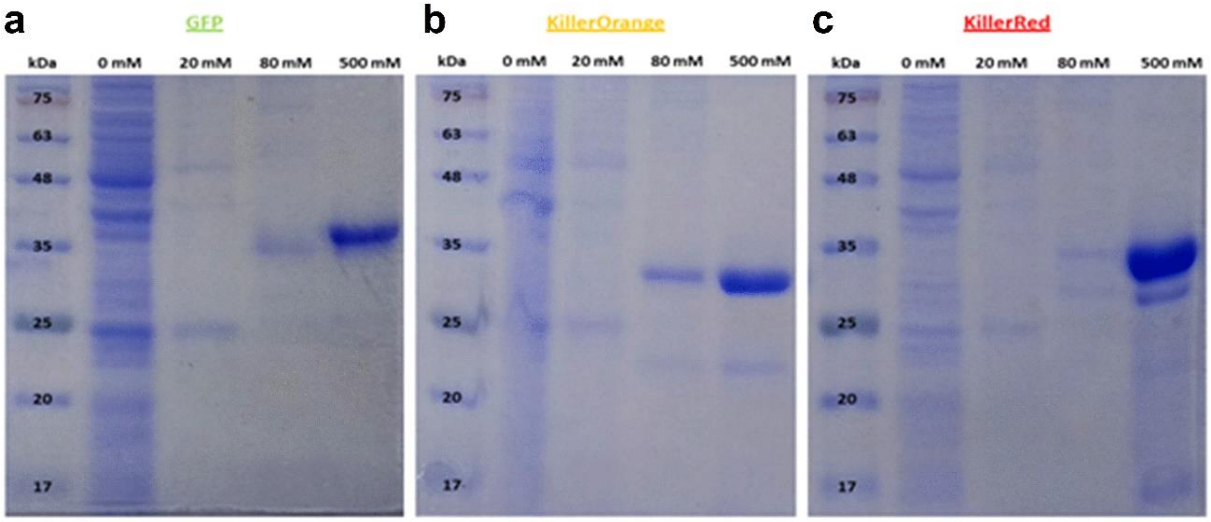

Figure 7: Results of SDS-PAGE for a) GFP, b) KillerOrange, and c) KillerRed purification in liquid chromatography upon an increased imidazole concentration gradient. Protein elution occurred with 500 mM Imidazole.

Table 1: Extinction coefficients at 280 nm wavelength, and theoretical pI of GFP, KillerOrange, and KillerRed estimated via ExPaSy[96].

Protein	$\varepsilon_{280\ nm}$ ($g.l^{-1}$)	pI
GFP	0.765	6.95
KillerOrange	0.476	6.09
KillerRed	0.308	7.07

The subsequent biophysical characterization focused on evaluating the protein viability in adverse conditions possibly found in clinical applications such as low pH, hyperthermia, and exposition to ionizing radiation. CD spectroscopy was used to monitor the protein secondary structures under those conditions. The obtained spectra (**Figure 8**a-c) presented a negative peak with a minimum around 215 nm, characteristic of structures with the predominance of β-sheets[97], which agrees with the known 3D structures of the proteins. The positive peak with maximum at wavelengths below 200 nm could not be acquired due to the high absorption of the sample in this region.

The UV-Vis and fluorescence spectroscopy were performed to evaluate the chromophore maturation (**Figure 8**d-f)[98-100]. The structure of the chromophores is essential because it is responsible for protein activity. The correct chromophore maturation implies higher fluorescence quantum yield and, consequently, higher ROS production. In general, fluorescence competes with intersystem crossing to the excited triplet state so that fluorescence quantum yield and ROS generation are inversely correlated[101, 102]. Nevertheless, the fluorescence phenomenon indicates that the chromophore was able to be excited and is easier to measure than the generation of ROS. For this reason, the fluorescence intensity is considered here as an indirect measurement of the chromophore excitation and, consequently, ROS generation. The CD and UV-vis results (**Figure 8**) showed that the proteins were correctly folded and the chromophores properly matured.

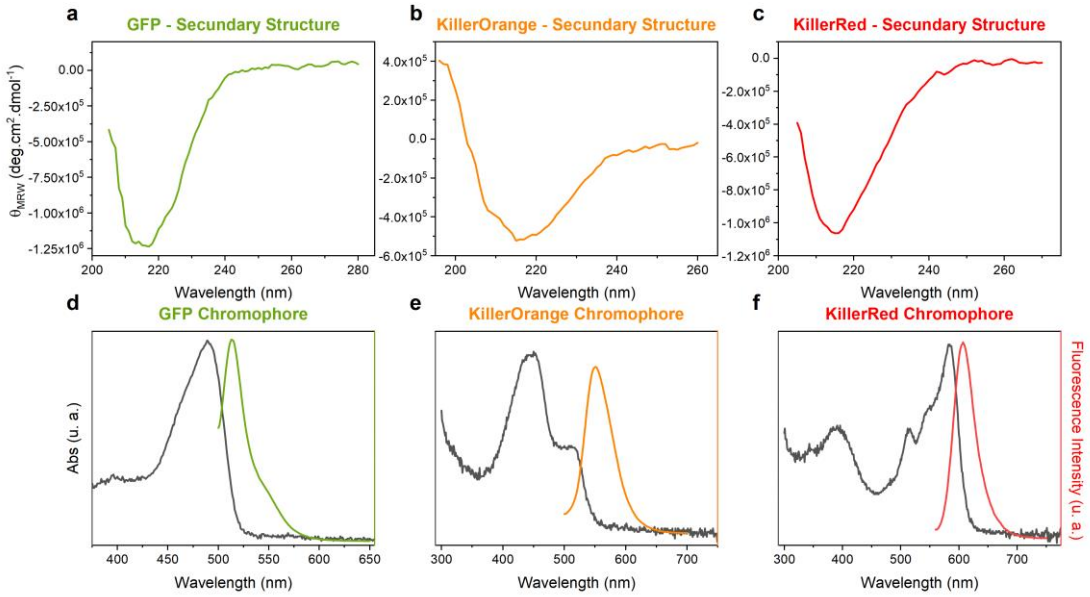

Figure 8: Top – Monitoring secondary structure of a) eGFP, b) KO and c) KR using circular dichroism (CD). Bottom – Optical characterization of d) eGFP, e) KO and f) KR. The black lines show the absorbances and the coloured lines show the fluorescence of the proteins.

Thermal denaturation tests were performed by CD and DSC. The DSC profiles (**Figure 9**a-c) indicated the proteins were thermally stable with melting temperatures around 80 ºC. eGFP denaturation occurred in a single endothermic event, whereas the other two proteins had two or more distinct peaks. This difference is probably associated with the fact that the Killer proteins, unlike monomeric eGFP, tend to form dimers[103, 104]. CD measurements (**Figure 10**) revealed no spectral changes up to 60 °C when a disturb in the secondary structure arrangement could be observed for eGFP and KR, as indicated by the onset of intensity change. These results corroborate the high thermal stabilities of the proteins. However, the few amino acid residues that differentiate KO from KR[105] do not affect their thermotropic behaviour in a way that impairs the proposed application. Optical therapies usually result in hyperthermia, which is tissue heating within the 42-46 °C range. According to the literature, The apoptosis ratio for temperatures 43 °C and 50 °C was approximately 0.8[106], which is still far below the melting temperatures (T_M) of any of the proteins involved in this study (T_M GFP = 82.0 °C, T_M KO = 78.9 °C, T_M KR = 84.7 °C).

Another situation found during *in vivo* applications is pH variations. This could be caused by a significant decrease in extracellular and intracellular pH, commonly observed in tumour cells where pH values as low as 5.7 can be found (compared to a pH of 7.4 in normal tissues)[107]. Acidic microenvironments arise in tumours due to their altered vascularization, causing insufficient delivery of metabolites, such as oxygen, to many areas within the tumour.

Hence, there is an increase in lactic acid production under anaerobic conditions and adenosine triphosphate (ATP) hydrolysis, contributing to the increased acidity in tumour microenvironments[107, 108]. When subjected to pH variation, proteins can have not only their structure but also their function affected. This happens because, with the pH variation, the chromophore protonation changes, thus affecting the resonance of their conjugated double bonds. During this process, the absorption bands can shift to regions that do not correspond to the excitation of the chromophore, leading to the inactivation of protein's fluorescence[109]. To study such behaviour, the absorption of the chromophores of each protein was monitored according to the pH variation.

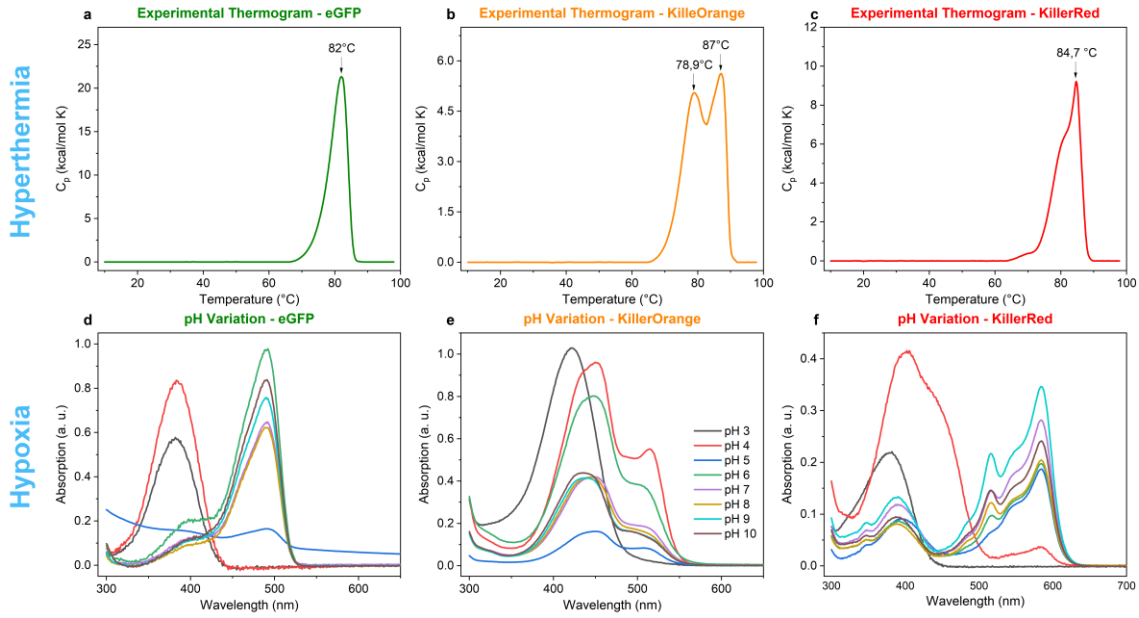

Figure 9: The thermal stability of (a) eGFP, (b) KO and (c) KR was monitored by DSC, and protonation state of (d) GFP, (e) KO, and (f) KR chromophores due to pH variation was monitored by optical absorption spectroscopy.

The eGFP, KR, and KO absorbance spectra in buffer solutions at different pH values demonstrated similar behaviours for the three proteins (Figure 9d-f). At pH 3, the absorption peaks at excitation wavelength were completely suppressed for the three investigated proteins. At pH 4, this condition was maintained except for KO, suggesting that its chromophore is less sensitive to acidic environments. At pH 5, the protein structures were mostly disturbed (it was possible to observe precipitation), and the absorption spectra had their intensities reduced in all their extensions, indicating the proximity to the isoelectric point (pI) of the three proteins. For higher pH values, no relevant variations in the spectra were observed. The chemical equilibrium shift of the chromophore from a protonated state to a deprotonated state for pH > 5 indicates that proteins remain active in adverse physiological conditions.

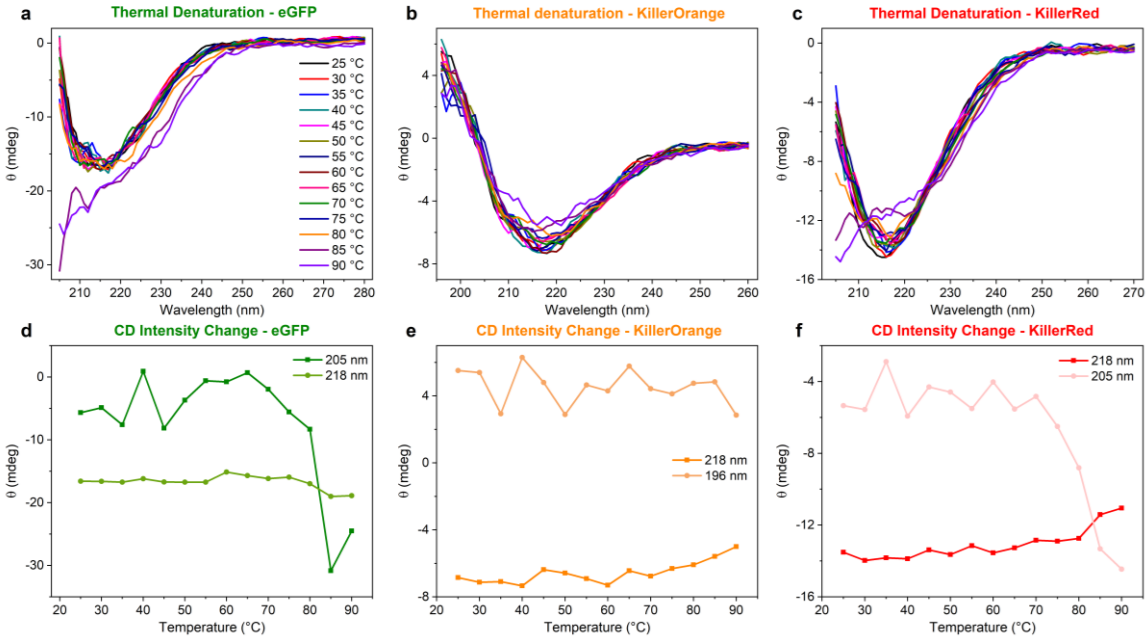

Figure 10: The three proteins had their secondary structure thermal stability monitored CD upon temperature increasing from 25 ˚C to 90 ˚C. a), b), and c) show the CD spectra of eGFP, KO, and KR, respectively. The intensity variation at 205 and 218 nm due to temperature variation are shown in d) eGFP, e) KO, and f) KR.

Besides hyperthermia and low-pH environments, exposition to ionizing radiation is also common during cancer treatments. The use of ionizing radiation in the treatment of tumors is based on tumor destruction by absorbing radiation energy. The effects of radiation are proportional to the absorbed dose. However, the doses required to eradicate the tumor are still very high, ranging from 50 to 100 Gy[110]. The absorbed dose has notorious effects on the biological macromolecules, which are modified by direct ionization and reactivity of species derived from water radiolysis (indirect effects of ionizing radiation). Direct radiation damage consists of breaking S–H, O–H, N–H, and C–H bonds. The biomolecular damage induced by water radiolytic products begins with thiol depletion and rupture of C–C and C–N bonds[111]. Therefore, to verify systematic breaks in the peptide bonds or side chains of amino acid residues, two polyacrylamide gel electrophoreses were performed with protein aliquots before and after irradiation with 100 Gy: one under SDS denaturing condition and another under native condition. The results are shown in **Figure 11**, and no significant changes in the gel displacement patterns were observed.

Finally, the effects of ionizing radiation on the optical activity of the proteins were tested. The luminescence of the three proteins revealed no detectable scintillation during radiation exposure. After being irradiated with up to 100 Gy, neither variation in their absorbance nor in their fluorescence spectra were observed (data not shown). The results

described above show that eGFP, KO, and KR meet structural stability requirements against variations in physicochemical parameters and irradiation, thus becoming potential candidates for the designated application, but still requiring a ScNP to form a X-ray excitable system.

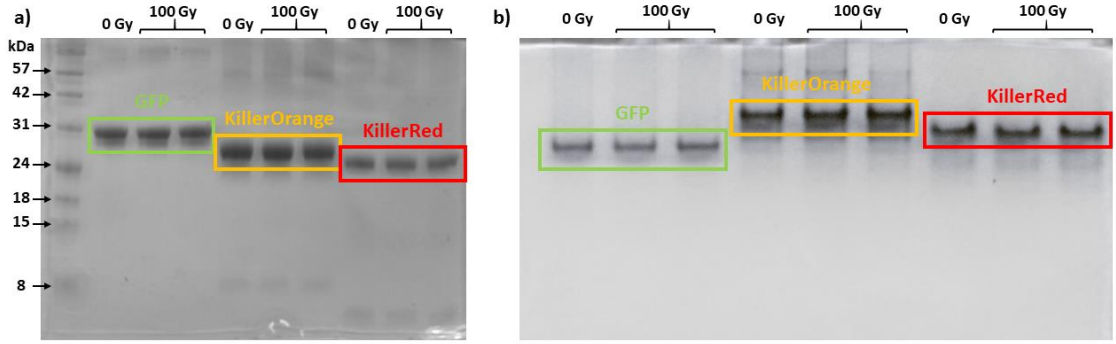

Figure 11: Polyacrylamide gel electrophoresis in (a) denaturing condition and (b) native condition for eGFP, KO, and KR proteins after receiving an equivalent dose to 100 Gy X-ray in air. The assessment aimed to observe structural damage due to ionizing radiation.

2.3.2 $LaF_3:Tb^{3+}$ Synthesis and Characterization

Aiming at increasing the amount of energy delivered in deeper tissues by optical therapies and the efficacy of radiation therapy treatments, we sought a scintillating nanostructure that could efficiently transfer the energy of ionizing radiation to the proteins/PS described above. Due to their high atomic number, rare-earth nanoparticles, such as $LaF_3:Tb^{3+}$, promote enhanced interaction with ionizing radiation, besides presenting low toxicity and the possibility of suspension in water[112].

The protocol used was adapted from reference 113 to optimize the synthesis of $LaF_3:Tb^{3+}$ in terms of the particle suspension's homogeneity with high scintillation intensity. The solvent was changed from water to ethylene glycol for a higher temperature reaction. This together with the addition of NH_4F by hot injection was intended to cause rapid and homogeneous nucleation. Then, the samples were washed four times with water to eliminate the remaining reactional residues. Several techniques were used to characterize the $LaF_3:Tb^{3+}$ nanoparticles. The incorporation of terbium into the crystal structure was assessed by steady-state fluorescence with excitation at 283 nm. The four expected emission peaks attributed to the electronic transitions of Tb^{3+} $4f^8 \rightarrow 4f^7\ 5d^1$ were observed (**Figure 12**a).

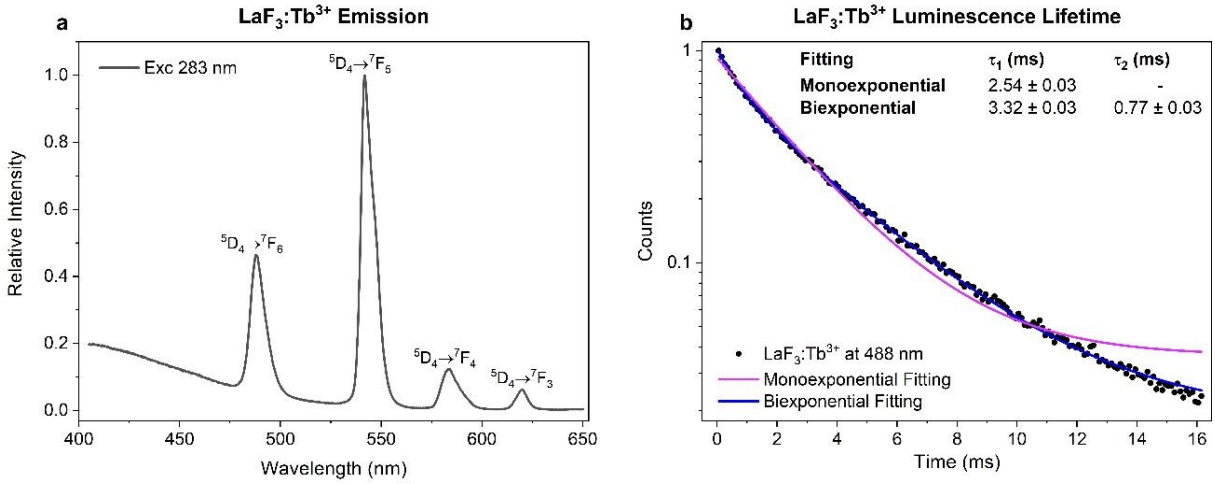

Figure 12: The $LaF_3:Tb^{3+}$ spectral profile and luminescent lifetime were acquired. a) PL spectrum of $LaF_3:Tb^{3+}$. b) Luminescence lifetimes recorded at 488 nm for $LaF_3:Tb^{3+}$ in water and mono and biexponential fitting. The errors in the calculated parameters include the standard deviation from curve fitting.

FTIR measurements (**Figure 13**a) were performed at three different steps of the synthesis. The first was at the end of the synthesis reaction itself. At this point, the sample was still suspended in ethylene glycol. The second point was dried $LaF_3:Tb^{3+}$ (powdered) after three washings with water before calcination. A broad band centered at 3,414 cm^{-1} attributed to O–H stretching was observed for both samples[114, 115]. Another band at 1,634 cm^{-1}, attributed to the angular bending of H–O–H, was observed only for the washed and dried sample. The presence of two vibrational modes of the hydroxyl group is probably due to the residual water still adsorbed on the surface of the nanoparticles. In addition, the washed sample still had characteristic bands of the ethylene glycol solvent, which are: 1,080 cm^{-1} corresponding to the C–O stretching vibration coordinating to metal cations[116], 2,920 cm^{-1}, and 2,955 cm^{-1} corresponding to symmetrical and asymmetrical stretching of the H–C–H groups. Based on these results, we concluded that ethylene glycol molecules are bound on the surface of $LaF_3:Tb^{3+}$ nanoparticles, revealing their role as a binder besides acting as a solvent.

As evidenced by **Figure 13**a, ethylene glycol was not completely removed with a simple washing protocol. Functional groups on the surface of nanoparticles are important for their biological applications. However, these groups may also contribute to a non-radiative decay, thus quenching the luminescence. In this sense, high-temperature thermal annealing could be an alternative to remove the remaining ethylene glycol from the nanoparticle surface.

To determine the optimal calcination temperature, the thermal behavior of our complex was investigated by thermogravimetric analysis under air and N_2 atmosphere (**Figure 14**). There were three weight losses in the thermal decomposition curves. The first loss (1.4 % and 1.6%

approximately for air and N_2 atmosphere, respectively) occurred at temperatures below 150 ºC and were probably related to the evaporation of adsorbed water. In the second transition, 6.1% of the mass was lost for the sample in contact with atmospheric air when it reached approximately 400 °C. Under nitrogen flow, the mass loss was slower and reached 5.6% of weight at temperatures around 500 °C. The transitions observed were likely due to the thermal decomposition of organic residues, probably related to the remaining ethylene glycol. Above 700 °C, the mass loss was pronounced for $LaF_3:Tb^{3+}$ in contact with oxidizing atmosphere (9.9%), compared to the loss observed in an inert atmosphere (6.8%).

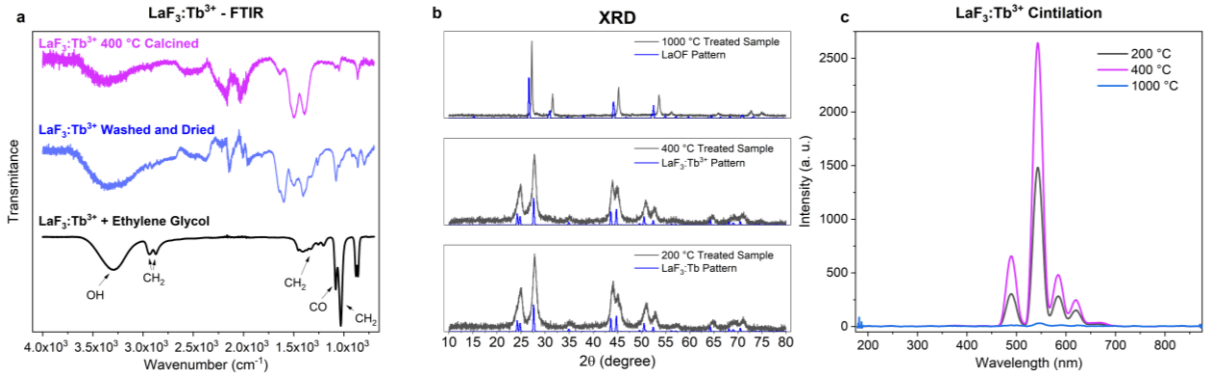

Figure 13: Spectroscopic characterization during the synthesis of $LaF_3:Tb^{3+}$. a) FTIR spectra of $LaF_3:Tb^{3+}$ nanoparticles suspended in ethylene glycol (black), in powder before (blue), and after (purple) calcination. b) XRD of $LaF_3:Tb^{3+}$ after heat treatment for 8 h at 1000 °C (top), 400 °C (middle) and 200 °C (bottom). c) Evaluation of the effect of calcination on radioluminescence of $LaF_3:Tb^{3+}$ nanoparticles.

After obtaining the TGA data, X-ray diffraction (XRD) was used to analyze the crystalline phase of three nanoparticle samples that underwent different calcination temperatures in atmospheric air. The result can be seen in **Figure 13**b. The samples consisted of $LaF_3:Tb^{3+}$ after heat treatments for 8 h at 200 °C, 400 °C and 1,000 °C. In the diffractogram of the sample treated at 200 °C, the X-ray peaks agreed with COD-9009994, which shows the presence of the LaF_3 crystal structure in a hexagonal phase. However, for $LaF_3:Tb^{3+}$ nanoparticles reported here, a slight shift of the diffraction peaks was observed compared to those of LaF_3 nanoparticles, which could be related to the differences between the LaF_3 and TbF_3 lattices. The same peaks were observed in the diffractogram of the sample treated at 400 °C, showing no changes in the crystalline arrangement. The X-ray diffractogram of the sample treated at 1,000 °C had a distinct profile, which might be associated with the emergence of a different phase and/or compound due to the heat treatment. Indeed, the diffraction patterns revealed the production of tetragonal lanthanum oxyfluoride (LaOF). It has been previously reported that heat treatments at temperatures above 700 °C in the presence of oxygen lead to a transformation from LaF_3 to LaOF[117, 118]. This could explain the differences found in TGA in

the presence of O_2 or N_2: variations in transition temperatures and the exchange of two fluorine ions for only one oxygen atom.

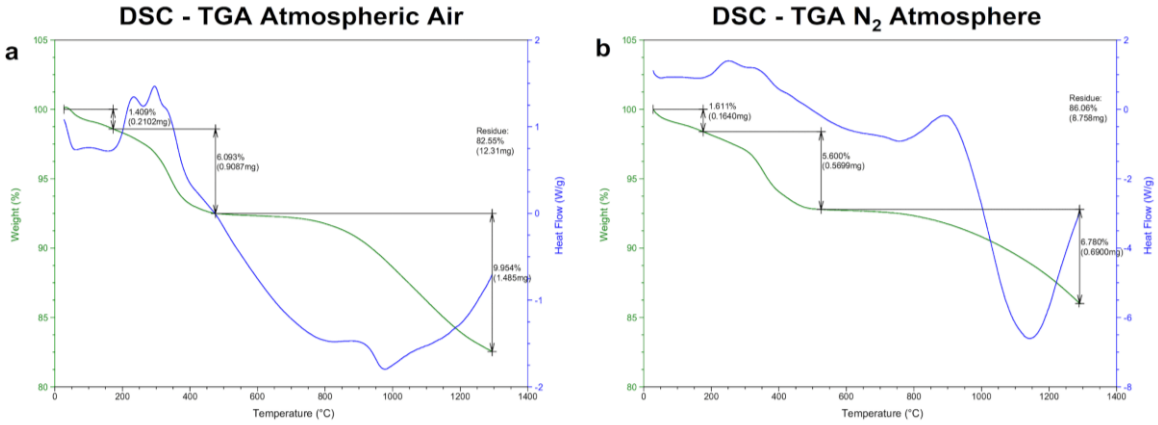

Figure 14: $LaF_3:Tb^{3+}$ thermal decomposition in air and inert atmosphere were evaluated with TGA curve of the $LaF_3:Tb^{3+}$ nanoparticles in (a) atmospheric air and (b) N_2 atmosphere.

For practical purposes, it is important to investigate the effect of calcination on the scintillation of $LaF_3:Tb^{3+}$ (**Figure 13**c). While ScNP treated at 400 °C showed an incredible 80 % increase in their scintillation compared to the sample treated at 200 °C, the luminescence peaks of the sample treated at 1,000 °C disappeared entirely. FTIR analysis of the calcined nanoparticles at 400 °C (**Figure 13**a) revealed a drastic decrease in O–H, C–O, and H–C–H vibrational mode intensities, suggesting the increase in temperature caused the loss of remaining organic compounds from the synthesis, eliminating some vibrational modes and crystalline defects in the sample. These changes in the crystal lattice provide greater efficiency in the radiative electronic transitions, leading to enhanced luminescence emission. Rising the calcination temperature above 700 °C extinguished those transitions. Therefore, the adopted $LaF_3:Tb^{3+}$ calcination temperature for subsequent characterizations was 400 °C.

The nanoparticle hydrodynamic radius also plays an important role in biomedical applications. **Figure 15**a reveals that $LaF_3:Tb^{3+}$ calcined at 400 ºC and resuspended in water had a hydrodynamic diameter of 91 nm and a polydispersity index of 0.249. TEM images (**Figure 15**b) of the same sample depicted an average size of (23 ± 2) nm. The observed agglomeration probably occurred during the drying of the sample on the copper grid. The difference in sizes and dispersed measurements are expected for such distinct techniques. TEM images showed the clustered particles but allowed also the individual particles to be distinguished, showing a more accurate measurement of the individual particle size[119], whereas the hydrodynamic radius measured by DLS showed more accurately the behaviour of nanoparticles in solution, as indeed they are applied here.

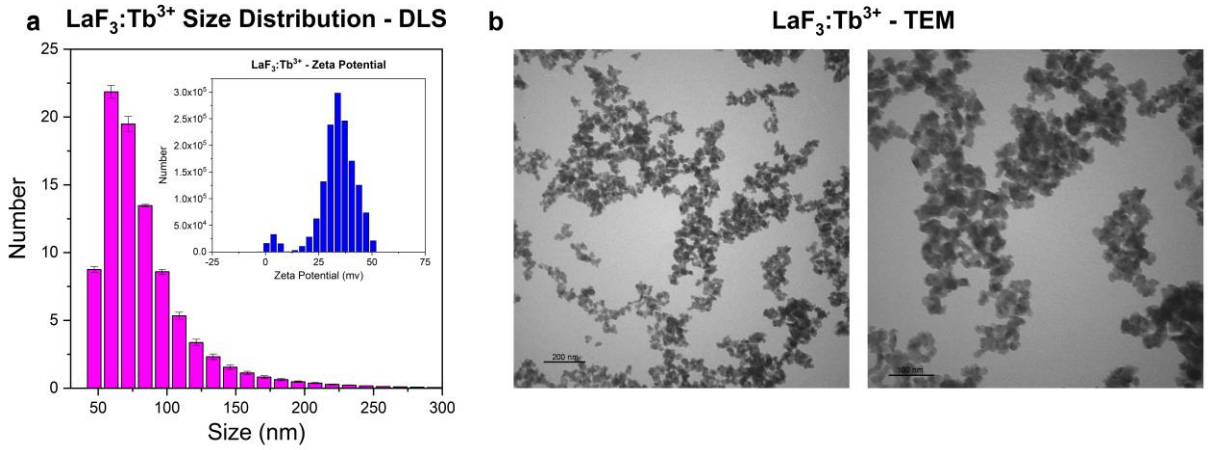

Figure 15: a) $LaF_3:Tb^{3+}$ Size distribution obtained by the DLS and the respective ζ-potential (inset). b) TEM images of the $LaF_3:Tb^{3+}$ nanoparticles after 400 °C calcination for 8 h.

The nanoparticle surface charge was obtained by ζ-potential measurements (**Figure 15**a, inset). The ζ-potential measured for $LaF_3:Tb^{3+}$ in water was +30.0 mV. A high value of ζ-potential is important because the electrostatic interactions due to the surface charge of the nanoparticles favour the stability of the suspension by repulsion as well as promote strong attraction with molecules of opposite charges[120]. In fact, when the nanoparticles were suspended in a solution with 150 mM of NaCl, DLS indicated an increase in size and polydispersity, and particle precipitation was visible. Therefore, these results suggest that the nanoparticle-protein interaction could occur via electrostatic interactions as well as by chemical coordination/binding of the 6xHis-tag to the metal ions at the nanoparticle surface.

2.3.3 Spectroscopic Characterization

The ScNP luminescence upon excitation in both UV and X-ray ranges resulted in the expected Tb^{3+} emissions at 489, 543, 584, and 620 nm (**Figure 12**a and **Figure 13**c). The broad spectral lines of the emission spectrum indicated the inhomogeneity of the sites occupied by the terbium in the lattice[121]. The lifetime of the excited state of the Tb^{3+} ions in the $LaF_3:Tb^{3+}$ suspension is also shown in **Figure 12,** and the calculated lifetimes of the excited state for the nanoparticles in water are displayed in **Table 2**. The biexponential shape (**Figure 12**b) of the curve indicates that the rare earth ions are in two different environments. Laporte-prohibited transitions of the Tb^{3+} ions generally show lifetimes in the millisecond time scale[114]. The longer lifetime agrees with that reported for Tb^{3+} ions in the literature. However, the shorter component leads to the hypothesis of a surface effect (multiphonon relaxation) and suggests migration coupled with defects or self-quenching of Tb^{3+} in the proximity[122, 123]. The nanoparticle

luminescence in solution also showed multiphonon relaxation by the solvent. In aqueous solutions, the dominant quenching pathway occurs by coupling the excited states of lanthanide ions to the O–H oscillators from water molecules coordinated to the cation. As a result, energy is transferred from the emitter excited states to the O–H oscillators of bound water molecules[114].

Table 2: Luminescence lifetimes of $LaF_3:Tb^{3+}$ nanoparticle. Luminescence lifetime of the nanoparticles in different suspensions.

Solvent	488 nm		585 nm	
	τ_1 (ms)	τ_2 (ms)	τ_1 (ms)	τ_2 (ms)
H_2O	3.43 ± 0.05	0.75 ± 0.03	3.44 ± 0.04	0.87 ± 0.03
PBS	3.27 ± 0.04	0.64 ± 0.04	4.01 ± 0.11	1.06 ± 0.09
PBS + NaCl	3.32 ± 0.03	0.77 ± 0.03	3.29 ± 0.04	0.49 ± 0.05

The luminescence lifetimes of the nanoparticles in PBS and PBS enriched with 150 mM NaCl were also acquired. Although in these conditions the nanoparticles suspensions were less stable, the decay time was not affected by the salt concentration, suggesting that the luminescent centers were not influenced by the distribution of charges in the medium and were, somehow, protected against collisional losses.

2.3.4 ScNP-PS Interaction

The results obtained so far were very promising considering the applications initially proposed. First, the proteins were shown to resist the harsh conditions that could be found during future *in vivo* applications. Furthermore, the scintillation of the nanoparticles was increased and the four Tb^{3+} emission peaks completely, or at least partially, overlapped with the eGFP, KO, and KR excitation bands (**Figure 16**a, **Table 3**). The high positive ζ-potential could also be an advantage to promote a strong electrostatic interaction between ScNP and negative sites of the protein, thus increasing the energy transfer. However, analyzing the charge distribution on the protein surface, the presence of sites with positive charges was also observed (**Figure 16**b). Subsequent experiments sought to investigate whether nanoparticles and proteins would interact, which physicochemical principle would promote their binding, and whether there would be energy transfer.

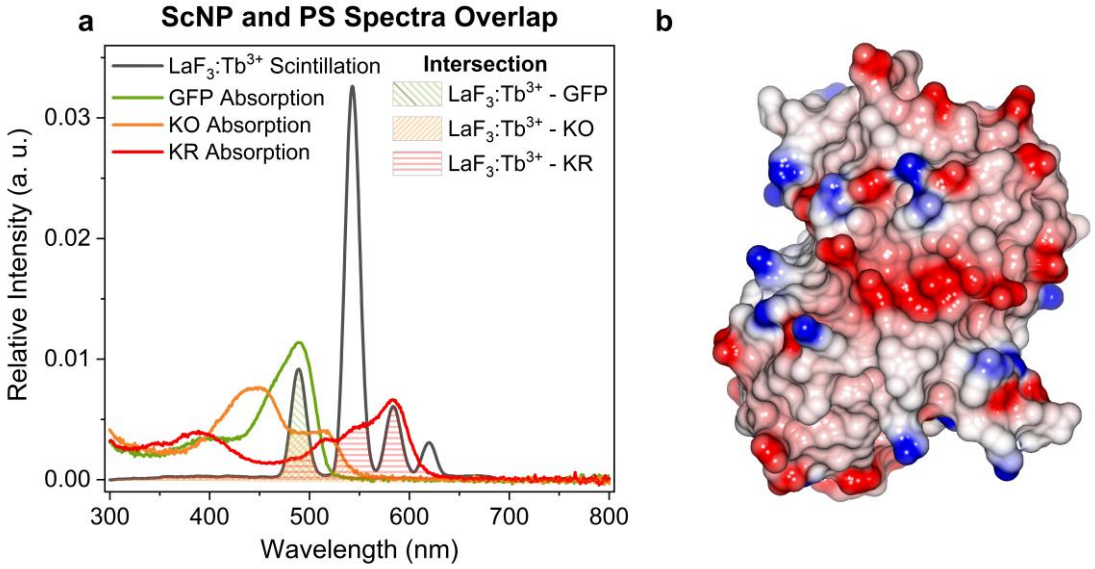

Figure 16: a) Spectral overlap of $LaF_3:Tb^{3+}$ scintillation and the GFP, KO, and KR absorption. The areas of all spectra were normalized to 1. The hatched regions highlight the intersections between the nanoparticle scintillation and protein absorption spectra. b) eGFP Electrostatic Surface. eGFP surface charge distributions. Positive and negative electrostatic potentials are indicated in blue (þ50 kTe1) and red (50 kTe1), respectively. eGFP was chosen to represent the three proteins with similar charge distribution.

Table 3: Relative areas of intersection between the nanoparticle scintillation and protein absorption spectra. The respective values correspond to the hatched areas in **Figure 16**.

	Intersection Area (a.u.)
$LaF_3:Tb^{3+}$ - GFP	0.22
$LaF_3:Tb^{3+}$ - KO	0.20
$LaF_3:Tb^{3+}$ - KR	0.39

To evaluate the binding between the proteins and the ScNP, mixtures of nanoparticles with proteins were prepared and, after allowing 20 min for protein-nanoparticle interactions to occur, these suspensions were centrifuged for 5 min at 13,000 rpm. This condition can cause ScNP to precipitate but should not be enough to separate protein aggregates, which requires at least 40 min centrifugation at 20,000×g at 4 ºC. At the end of centrifugation, the precipitates of the mixture turned into the color of the protein (**Figure 17**a), whereas the supernatant became colorless and translucid. This result indicates that $LaF_3:Tb^{3+}$ were able to carry proteins to the bottom of the tube, suggesting their binding.

TEM images of the nanoparticles mixed with the proteins were also acquired. **Figure 17**b of the ScNP prepared with KO was selected as an example, given that the behavior is similar for the three biomolecules. The $LaF_3:Tb^{3+}$ nanoparticles showed a tendency to form clusters,

which was enhanced in the presence of proteins, giving rise to larger and denser clusters. This could be due to the formation of protein aggregates during the drying of the sample for image acquisition. The aggregates led to the formation of polymeric matrices that expelled the nanomaterials, and, according to the literature, this expulsion depends on the size and concentration of the nanoparticles[115, 124, 125]. The polymer matrices are usually able to accommodate only a small percentage of nanoparticles, leading to segregation when high nanoparticle concentrations are employed. It should be emphasized that the low atomic number of the polypeptide chain leads to a low contrast image, making it difficult to observe the protein envelope surrounding the high atomic number/electronic density nanoparticles. In fact, proteins were not observed in any region of the TEM grid, reinforcing this hypothesis[116].

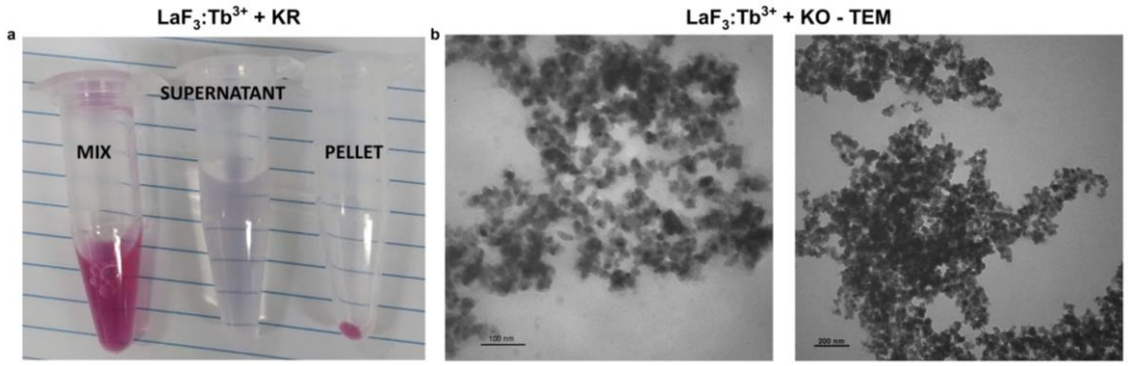

Figure 17: a) KR separation from the solution by interaction with $LaF_3:Tb^{3+}$: KR and $LaF_3:Tb^{3+}$ mixture before centrifugation (left), supernatant (center), and precipitate (right) of the mixture after centrifugation. b)TEM images of $LaF_3:Tb^{3+}$ mixed with KillerOrange. All experiments were performed with the three proteins and presented similar results.

The next step was to test whether the protein-nanoparticle complex resulted in energy transfer from ScNP to PS upon stimulation with X-rays. Promising results were found in the scintillation assays of $LaF_3:Tb^{3+}$-protein composites (**Figure 18**). Comparing the scintillation spectra of $LaF_3:Tb^{3+}$ with the spectra from mixtures of protein/nanoparticles upon increasing the protein concentration, we observed clear spectral changes for samples containing eGFP and KR. First, there was a relative reduction in the intensity of nanoparticle emission peaks coinciding with the absorption/excitation wavelengths of the proteins: 489 nm for eGFP and 584 nm for KR. In addition, there was a new emission peak at 512 nm in the eGFP mixture, which coincides with the emission wavelength of this protein. KR fluorescence also caused changes in the radioluminescence spectrum, increasing the relative intensity of the peak that coincides with its own emission (610 nm). This is a typical behavior of donor quenching and acceptor enhancement, characteristic of RET (resonance energy transfer)[63]. Based on the

radioluminescence spectra, the donor quenching showed a maximum RET efficiency of (0.52 ± 0.02) and (0.24 ± 0.03) for eGFP and KR, respectively.

Killer Orange presented once again a distinct behavior when compared with the other two proteins. Although the increase in KO concentration caused a reduction in peak intensity centered at 490 and 542 nm, with maximum RET efficiency of (0.66 ± 0.02), it was not possible to observe the contribution of its emission to the spectra. Allosteric interactions between the donor and acceptor sites could alter the donor emission by the enhancement of other decay processes[101], but it is suspicious that the affected peaks coincide with acceptor excitation. The most likely explanation for this result is the fact that KO displays a low fluorescence quantum yield and, therefore, its emission is masked by the nanoparticle scintillation. Although the Killer proteins have fluorescence quantum yields that are very close to each other[104, 105] (but much smaller compared to the eGFP quantum yield), the KR fluorescence can still be noted during X-ray irradiation because its emission wavelength coincides with a region of local maximum emission in the terbium spectrum and adds to it. In contrast, KO emission cannot be detected because it coincides with a spectral region of local minimum.

The decreased scintillation intensity of the donor (observed for ScNP in the presence of eGFP, KO, and KR) and the simultaneously increased photoluminescence intensity of the acceptor emission peak (observed for eGFP and KR) followed a linear behavior when plotted as a function of protein concentration until it reached a saturation plateau (**Figure 18**d-f). When the plateau was reached, the protein concentration was considered surplus, and the inflection region of the curve (highlighted in the graph) was considered the optimal concentration for energy transfer. eGFP had the lowest saturation concentration (0.75 mg/ml), followed by KO and KR with 1.8 mg/ml and 3.36 mg/ml, respectively. This indicates that the 6×His-tag acts as a binding site once the protein that reaches the saturation of energy transfer in the lowest concentration (eGFP) is the one with 6×His-tag at both ends of the polypeptide chain. The Killer proteins, which have the 6×His-tag only at the N terminus, require higher concentrations to effectively bind to the ScNP and optimize the energy transfer mechanism. It has already been shown that the presence of two or three 6×His-tags can increase the binding strength and control the position of proteins on the surface of nanoparticles in order to decrease the number of proteins bound and increase the energy transfer since the disposition of the acceptor chromophore to the donor can affect the efficiency of this phenomenon[126].

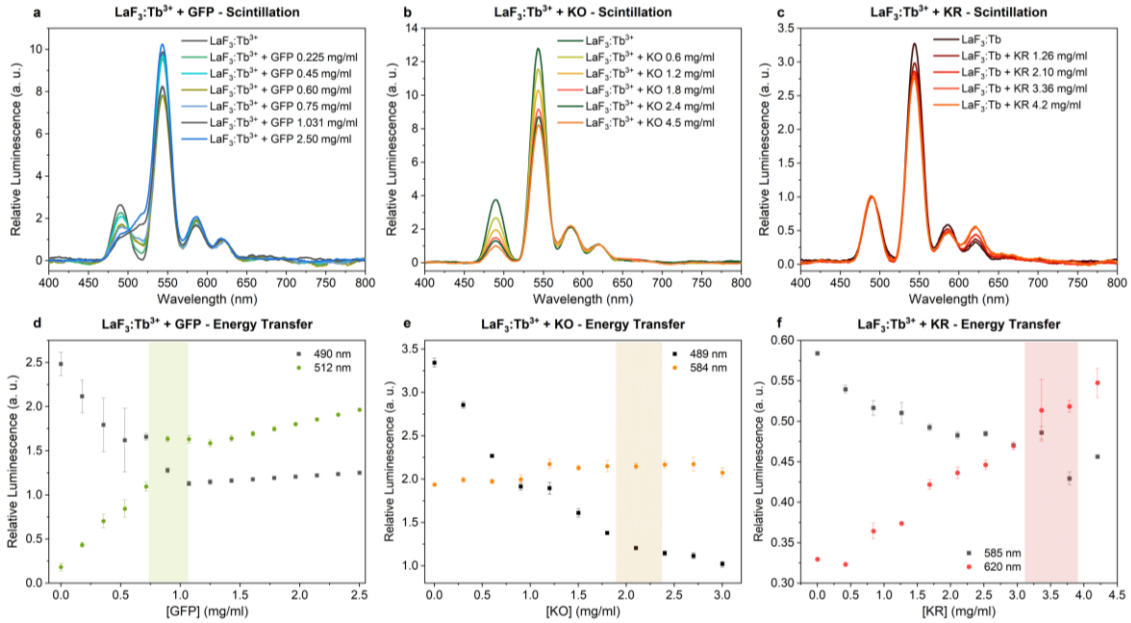

Figure 18: Study of the energy transfer from $LaF_3:Tb^{3+}$ to the proteins. Distortions in the scintillation spectra due to interaction with proteins a) eGFP, b) KO, and c) KR. Monitoring the excitation and emission peaks of d) GFP, e) KO, f) and KR in the $LaF_3:Tb^{3+}$ scintillation spectra as the protein concentration increased.

Table 4: Luminescence lifetimes of $LaF_3:Tb^{3+}$ nanoparticle and protein (GFP and KO) mixture at 488 nm.

	Solvent	τ_1 (ms)	τ_2 (ms)	τ_3 (ms)
GFP	H_2O	3.03 ± 0.04	0.72 ± 0.02	0.033 ± 0.003
	PBS	3.38 ± 0.04	0.84 ± 0.03	0.041 ± 0.003
	PBS + NaCl	3.56 ± 0.07	1.01 ± 0.04	0.042 ± 0.003
KO	H_2O	3.49 ± 0.08	1.11± 0.07	0.16 ± 0.03
	PBS	3.22 ± 0.05	0.79 ± 0.04	
	PBS + NaCl	3.29 ± 0.04	0.71 ± 0.03	

Table 5: Luminescence lifetimes of $LaF_3:Tb^{3+}$ nanoparticle and KR mixture at 585 nm.

	Solvent	τ_1 (ms)	τ_2 (ms)	τ_3 (ms)
KR	H_2O	3.7 ± 0.6	1.2 ± 0.2	0.062 ± 0.009
	PBS	3.3 ± 0.3	0.9 ± 0.2	0.13 ± 0.03
	PBS + NaCl	3.5 ± 0.2	0.8 ± 0.1	--

The energy transfer was also assessed by measuring the fluorescence lifetime of the donor's emission peaks. As previously shown in **Table 2**, nanoparticles show a multi-

exponential decay with two distinct lifetimes. The long lifetime, on the order of ms, is characteristic of the Tb^{3+} incorporated within the nanoparticle, and the shorter lifetime results from the rare earth ions found on the surface[114]. When proteins were added to suspensions of nanoparticles in water, a third component was found in the multi-exponential (best fit) decay (**Table 4 and Table 5**). This new lifetime, on the order of µs, is possibly originated by the decay of Tb^{3+} ions that are now transferring energy to the chromophores. From **Figure 19**a and d, it is clear that energy transfer happens for eGFP, KO and KR due to the significant decrease in the luminescence decay lifetime (**Figure 19**).

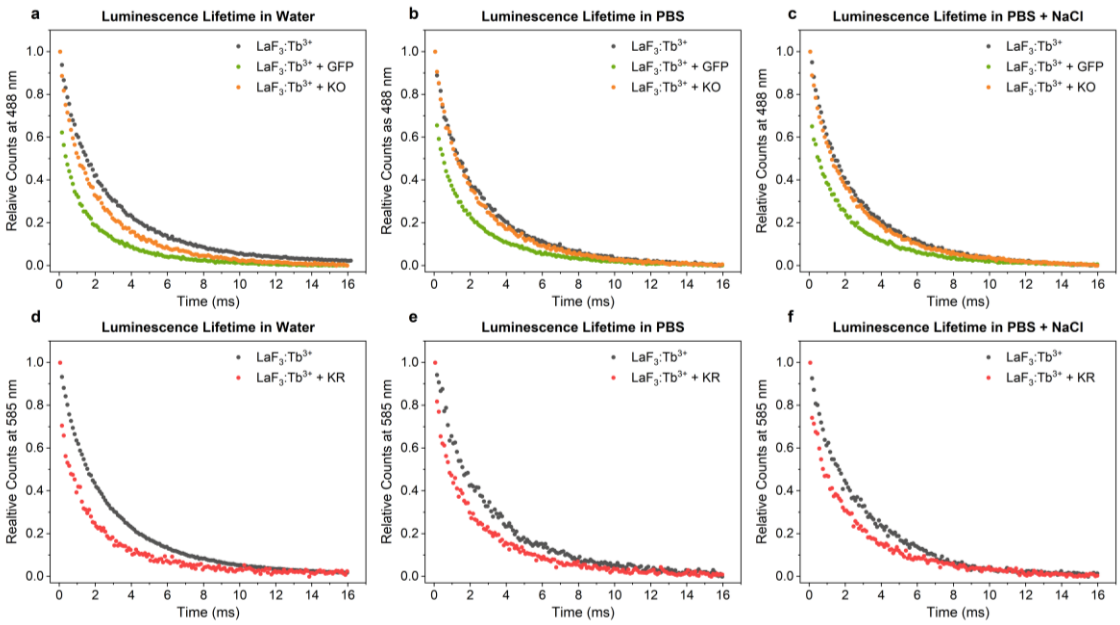

Figure 19: Luminescence lifetime of $LaF_3:Tb^{3+}$ with protein recorded at 488 nm (a-c) and 585 nm (d-f) following 285 nm excitation.

In order to further verify the role of 6×His-tag on ScNP-protein binding, two extra experiments were performed. First, the separation by centrifugation of the $LaF_3:Tb^{3+}$ and eGFP was prepared in suspensions with an increasing gradient of imidazole concentration. The concentration of protein in the supernatant, monitored by absorption at 490 nm (**Figure 20**a), increased according to the increased concentration of imidazole in solution, showing that this compound works as a competitor for the interaction with the nanoparticles. For the other experiment, eGFP mixture with the highest protein concentration but still in the linear energy transfer region (0.75 mg/ml) (**Figure 18**d) was diluted several times in PBS, and the scintillation spectrum was recorded for each dilution. Upon dilution, the ScNP-protein distance would increase if the parts were not bound. This would result in a decreased efficiency of the energy

transfer process, leading to a decreased protein emission and recovery of the scintillation intensities. However, this behaviour was not observed: the ratio between the emission peaks of the donor and acceptor remained constant for all dilutions (**Figure 20**b), indicating a fixed distance between proteins and ScNP and, consequently, proving the stability of the complex. Repeating the same procedure for dilutions in PBS enriched with 100 mM imidazole, a decrease in the emission intensity ratio 512 nm/490 nm was observed. These results show that, indeed, 6×His-tag is largely responsible for the ScNP-PS binding, while the electrostatic interaction seems to have a secondary role (as shown by the luminescence lifetime). In addition, the decrease in energy transfer with the separation of the two molecules is another characteristic behaviour of energy transfer via RET and not by a trivial mechanism, corroborating the hypothesis raised earlier.

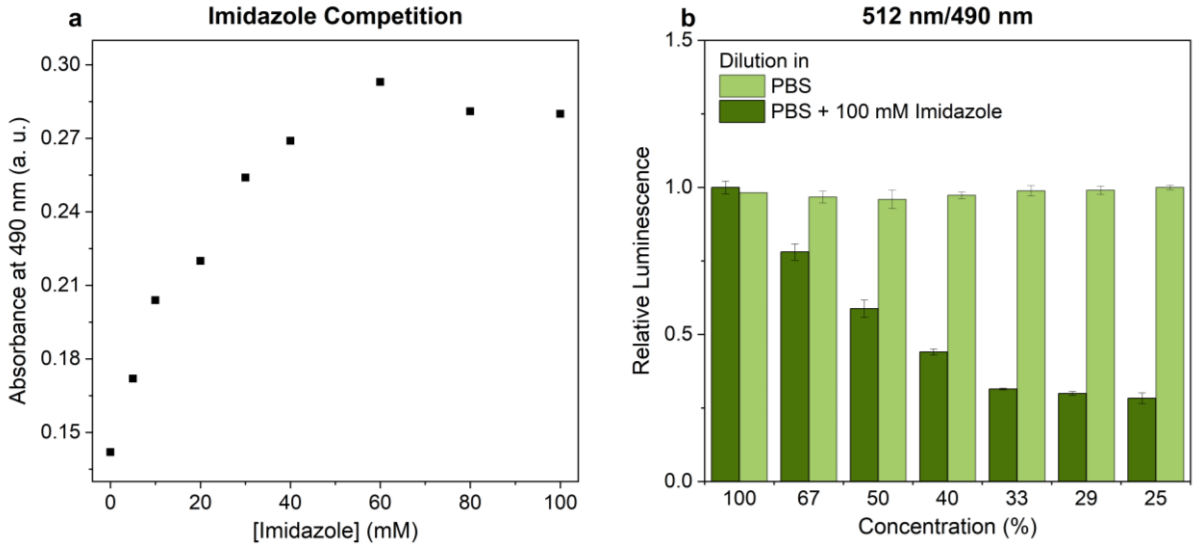

Figure 20: Evaluation of the role of 6xHis-tag at ScNP-PS binding. a) Increasing protein concentration at supernatant with the imidazole concentration. b) Ratios between the absorption and emission wavelengths of the GFP protein, after stimulation with X-ray, for several dilutions of the LaF_3:Tb^{3+} + GFP complex in water.

2.3.5 Cytotoxicity

To consolidate the KR-LaF_3:Tb^{3+} complex as a new alternative for the use of genetically encoded PS in X-PDT, the toxicity of this complex was evaluated by monitoring the *E. coli* growth curve in the presence and absence (negative control) of the conjugate KR-LaF_3:Tb^{3+}upon irradiation with UV-A and X-ray (**Figure 21**). Because both UV-A and X-ray can excite the lanthanide nanoparticle but not the KR, it is expected that any toxicity of the conjugates would be due to the generation of ROS by the KR as a result of the absorption of energy from the radiation beam by the nanoparticles and the subsequent energy transfer from

the LaF_3:Tb^{+3} nanoparticles to the protein. A conventional bacterial growth curve is divided into four distinct phases: the lag phase that precedes growth, the log phase characterized by cell division, the stationary phase when growth is environmentally limited, and finally, the death phase.

By tracking the absorption of the culture medium after irradiation, three different profiles were observed for the bacteria growth in the presence of KR-LaF_3:Tb^{3+}. (i) The first profile, observed for the samples kept in the dark, is the same for all samples with and without KR-LaF_3:Tb^{3+}, which starts in the log phase. The same profile (i) was observed for samples irradiated without KR-LaF_3:Tb^{3+} (negative control). (ii) A second profile is characterized by slow bacterial growth within the first 3 hours, followed by the log phase. This profile was observed for the samples with KR-LaF_3:Tb^{3+} and irradiated with UV-A. (iii) In a third profile, any growth was observed before 3 hours of incubation (lag-phase) followed by the log-phase of growth. This profile is only observed for samples with KR-LaF_3:Tb^{3+} and irradiated with X-rays. After 10 hours, all samples were in the stationary phase irrespective of the irradiation conditions or presence/absence of the conjugates.

Those data suggest that the slow or absent bacterial growth during the first 3 h after irradiations, as observed in profiles (ii) and (iii), results from the cell death caused by the exposition to radiation, thereby reducing the number of viable cells in suspension. In this sense, the initial growth is slower, requiring longer periods to enter the log phase. By extrapolating the curve in the log phase, concentrations of colony-forming units (CFU) found in each condition at zero growth time were estimated (**Table 6),** confirming our hypothesis. Finally, to eliminate any chance that the cell death is caused solely by KR or LaF_3:Tb^{3+} upon irradiation, control samples containing only KR and only LaF_3:Tb^{3+} nanoparticles were investigated (**Figure 22**), revealing no difference in the growth profiles in the presence of KR alone. For the samples containing LaF_3:Tb^{3+}, the bacterial growth is impaired for the highest doses of UV-A and X-ray, although the cell death is significantly superior when in the presence of the KR-LaF_3:Tb^{3+} conjugates. The higher toxicity observed for the KR-LaF_3:Tb^{3+} under UV-A or X-ray irradiation evidences that the energy transfer from the LaF_3:Tb^{3+} to the KR increases ROS generation, allowing for protein activation using X-ray photons. Therefore, the KR-LaF_3:Tb^{3+} are strong candidates to combine radiation and photodynamic therapies in a single simultaneous treatment.

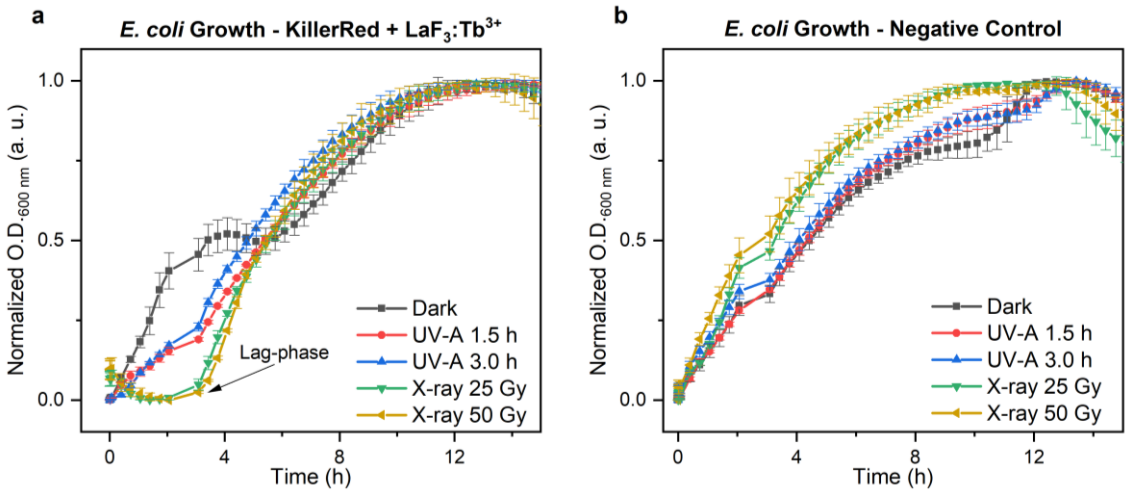

Figure 21: Growth course of *E. coli* Rosetta (DE3) in LB media upon UV-A and X-ray irradiation in (a) presence and (b) absence of the complex KR-LaF_3:Tb^{3+}.

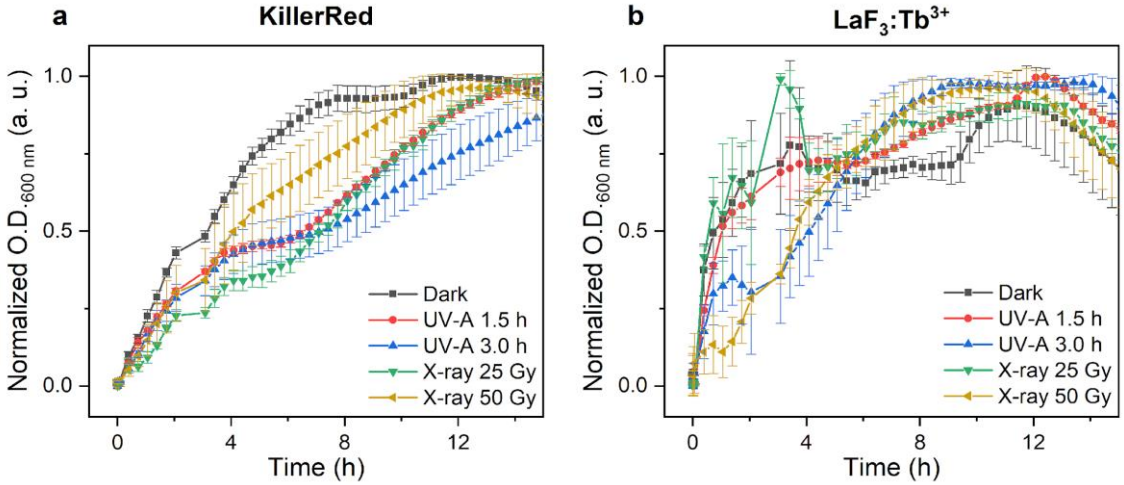

Figure 22: Growth course of *E. coli* Rosetta (DE3) in LB media upon UV-A and X-ray irradiation in the presence of (a) KillerRed and (b) LaF_3:Tb^{3+}. The error bars are the standard deviations from measuring four different samples in each condition.

Table 6: Estimation of CFU concentration. Estimation of colony-forming units at zero growth time after the different irradiation conditions of *E. coli* crops in the presence of the KR-LaF complex. The errors are the standard deviations obtained from counting colonies in four different plaques of each sample.

Condition	Bacterial concentration (unit/ml)
Dark	18.915 ± 0.004
UV-A 1.5 h	18.674 ± 0.005
UV-B 3.0 h	18.783 ± 0.006
X-ray 25 Gy	18.1 ± 0.1
X-ray 50 Gy	17.01 ± 0.06

2.4 Conclusion

Here, we reported the successful use of LaF_3:Tb^{3+} ScNP as a mediator for transferring energy from X-rays to genetically encoded photosensitizers. The exchange of the expression vectors of the eGFP, KO, and KR proteins to pET28a resulted in a significant improvement in the expression yield. The new condition did not affect the folding or oligomeric state of the proteins. The biophysical characterization sought to study the behavior of proteins under extreme adverse conditions to which they would be subjected *in vivo* during cancer therapies. The condition of hyperthermia pointed to thermally stable proteins and with TM above ca. 80 °C. pH variations can directly affect the protonation of chromophores, so it has a high potential for protein inactivation. Tests with ionizing radiation evidenced low interaction of proteins with X-rays and the absence of protein scintillation. Regarding nanoparticle scintillation, the synthesis protocol and thermal treatment were optimized to increase the particle size homogeneity and enhance the scintillation intensity of LaF_3:Tb^{3+}. The high value of ScNP ζ-potential suggested electrostatic interaction in the nanoparticle−protein system. Energy transfer from the ScNP to the three proteins is confirmed by scintillation (upon X-ray excitation) and by time-resolved fluorescence. Results also revealed that RET efficiency is higher for KO, GFP, and KR. However, eGFP and KR form stable compounds with the ScNPs, whereas KO dissociates readily. It was also shown that 6×His-tag acts as a linker for protein in nanoparticles doped with Tb^{3+}, promoting the formation of stable complexes. The KR− LaF_3:Tb^{3+} complex toxicity upon irradiation was demonstrated by assays monitoring *E. coli* death, thus suggesting ROS generation and confirming the energy transfer from the LaF_3:Tb^{3+} to the KR. In summary, the energy transfer between the scintillating nanoparticles and the proteins resulted in a conjugated nanocompound with radiation-exposure-dependent toxicity that opens a new avenue for the use of genetically encoded photosensitizers for applications in X-ray photodynamic therapy.

Chapter 3 – Combining Biophysics and Nanotechnology for the Applications of Blue Scintillators in Photomedicine

Abstract

In traditional applications of PDT, it may seem unappealing to excite a PS in the UV range due to its limited penetration into human tissues. However, the advent of new technologies for scintillator synthesis paves the way to excite the PS at wavelengths compatible with biomedical applications. Furthermore, a thorough understanding of the properties of each part of the system allows for the design of a more efficient complex of nanoparticles and photosensitizers. This chapter introduces innovative methods to attach proteins to blue luminescent nanoparticles, forming a stable dispersion in a solution like PBS. We enhance the luminescent properties of Hafnium Oxide (HfO_2) nanoparticles by doping them with titanium (Ti). The structural analysis confirmed the successful integration of Ti ions into the HfO_2 structure without forming any extra phase. While the Ti-doped nanoparticles were slightly larger than their undoped counterparts, they were effectively dispersed in water. However, these nanoparticles precipitated in PBS due to pH and ionic strength changes. We coated the nanoparticles with citric acid (CA) and miniSOG protein to create a stable dispersion in PBS. We also modified miniSOG's C-terminal to create miniSOG-PE, increasing the binding to the nanoparticles, stabilizing the colloidal dispersion in environments similar to biological systems. The effective attachment of miniSOG-PE to the nanoparticles is promising for future biomedical applications that require energy transfer in a top-quality colloidal system.

3.1 Introduction

Detecting radicals generated by GFP, KO, and KR was a big challenge, even though we proved their toxicity in *E. coli* culture[65]. In the search for more efficient genetically encoded PS, miniSOG appeared as a promising alternative due to its higher yield in generating reactive species, especially when compared with the GFP protein family[101]. Its photosensitizer potential has been confirmed *in vitro* by efficient induction of cell death and tumor growth inhibition under different irradiation conditions[65, 127-129].

Mini–Singlet Oxygen Generator (miniSOG) (**Figure 23a**) is a 106-residues long (~14 kDa), soluble, monomeric protein. It absorbs maximally at 448 nm with a shoulder at 473 nm with extinction coefficients of $(16.7 \pm 0.7)\times10^3$ and $(13.6 \pm 0.)\times10^3$ $M^{-1}cm^{-1}$, respectively[130] (**Figure 25**). Excitation of miniSOG leads to green emission with peaks at 500 and 528 nm and $^1O_2$ quantum yield of (0.47 ± 0.05)[130]. It was engineered from the LOV2 (light, oxygen, and voltage) domain of *Arabidopsis thaliana* phototropin 2 (AtPhot2) by DNA shuffling and random mutagenesis[130]. LOV domains are photosensors conserved in bacteria, archaea, plants, and fungi that detect blue light via a flavin cofactor.[131] Proteins based on LOV domains are blue-light photoreceptors that form a light-induced and reversible flavin-cysteine covalent adduct that consumes the energy of the excited state[132, 133]. The crystal structures of LOV domains show flavin mononucleotide (FMN) deeply buried inside the protein core[134]. Upon blue-light absorption, a covalent bond between the flavin chromophore and an adjacent reactive cysteine residue of the apo-protein is formed in the LOV2 domain. In phototropin, the excited state energy of FMN is consumed to form a covalent bond with a cysteine[135]. This subsequently induces a signal in the organism through phototropin 2 autophosphorilation[136].

The competition between oxygen quenching and protein quenching of the flavin triplet state seems to be a general feature of flavin-binding proteins[133, 137]. However, miniSOG contains six mutations as compared to its precursor, two of them involving residues surrounding the chromophore FMN [130, 133], which by itself is an efficient singlet oxygen photosensitizer[138] (**Figure 23b**). MiniSOG is initially moderately efficient towards $^1O_2$ generation due to limited oxygen accessibility and FMN triplet quenching by electron-rich side chains. Prolonged irradiation with blue light leads to photodegradation of FMN, which liberates the access of molecular oxygen to the alloxazine ring and reduces protein quenching of the triplet state, while oxidized electron-rich side chains cannot quench the triplet state of the chromophore. Hence, miniSOG presents increasing $^1O_2$ quantum yield[133]. Besides the high quantum yield for singlet

oxygen generation, miniSOG can generate other reactive oxygen species upon exposure to blue light[130].

The need for a cofactor is not a limitation for miniSOG since FMN is ubiquitous in cells and performs indispensable biological functions such as mitochondrial electron transport, fatty acid oxidation, and vitamin metabolism[139]. Furthermore, overexpression of miniSOG in HEK293 cells caused the FMN content to increase ~3-fold, presumably to keep miniSOG nearly saturated with FMN, but caused no obvious toxicity in the absence of light[130].

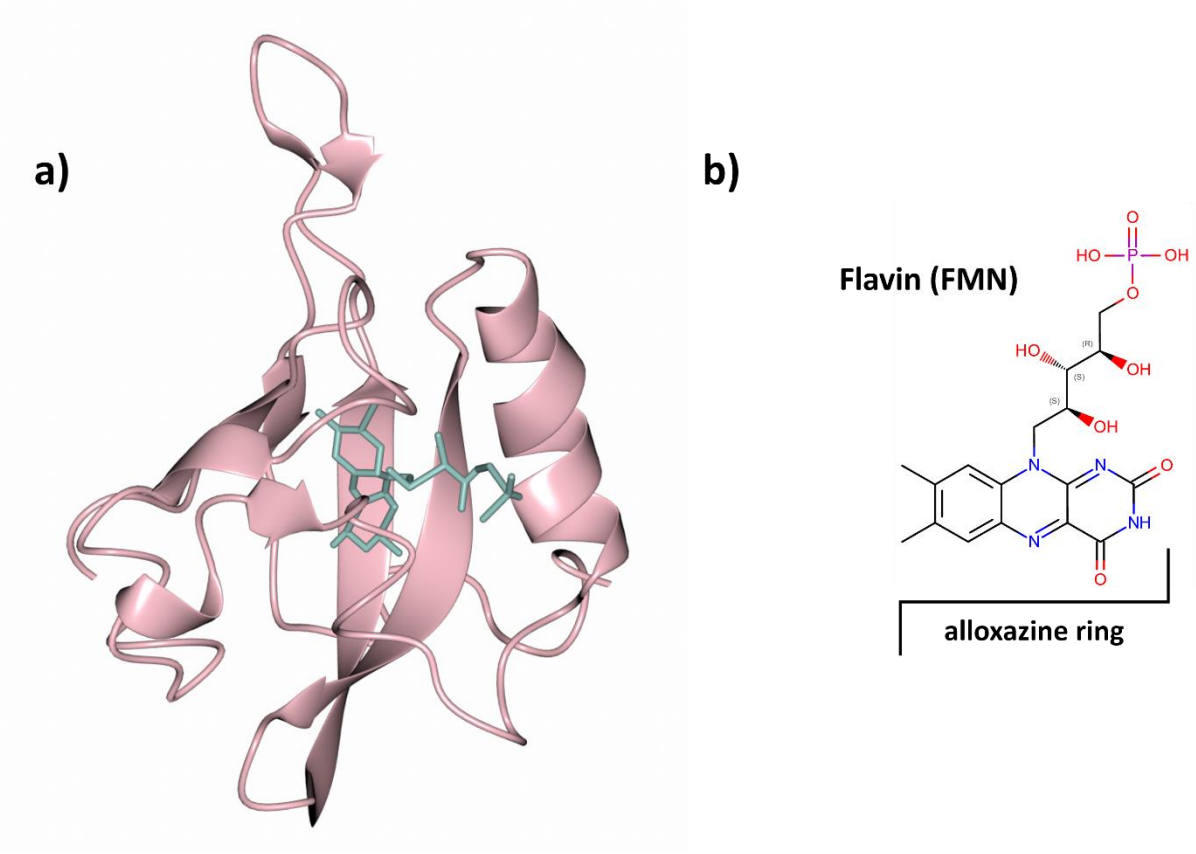

Figure 23: a) miniSOG structure (PDB ID 6GPU). b) miniSOG cofactor Flavin Mononucleodite (FMN), highlighting its alloxazine ring. Adapted from [133].

Besides miniSOG, Porphyrins and Chlorins are among the blue-absorbing PS commonly used for PDT *in vivo*. Red light is most often used to activate them due to several Q-bands extending as far as 630 nm. Nevertheless, they are most efficiently activated at the Soret band (~400 nm). The synthetic dye Phenalenone, often used as a reference standard for generating singlet oxygen and as an antimicrobial PS, is excited at 380 nm. Evidence shows that some transition metal coordination compounds can act as a PS when excited at ~450 nm. Most naturally occurring PS, such as Hypocrellin, Riboflavin, and Curcumin, have their absorption maxima above 470 nm[140]. It has also been shown that an organoiridium-albumin

bioconjugate works as a nucleus-targeted vehicle for anticancer PDT after photo-irradiation at 340 nm[141].

UV, violet, and deep blue radiations are the least transparent to human tissues, and therefore, their use in therapeutic strategies would benefit the most from an adequate ScNP-PS system[142]. Even though the terbium luminescence (between 489 and 620 nm)[65] has only a small intersection with the therapeutic window (600 to 800 nm)[143], it can still be used with a range of new photosensitizers that would not be viable due to the low penetration of visible light into the body.

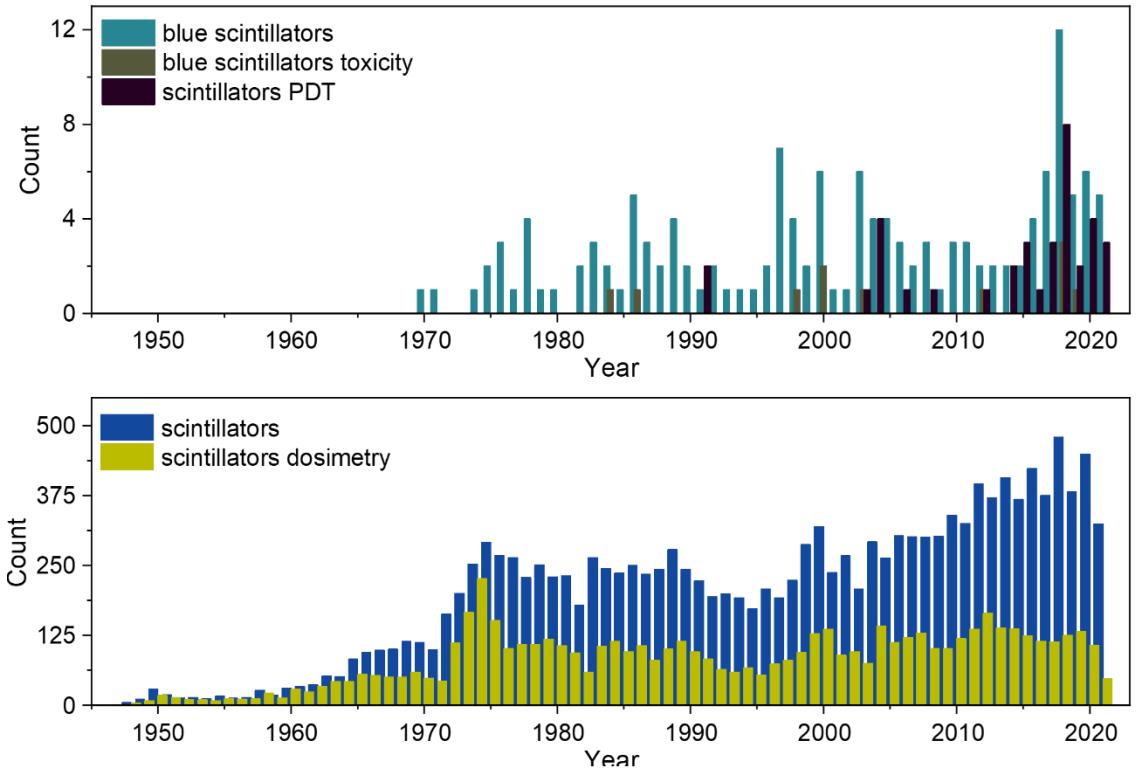

Figure 24: Number of publications for each year since 1940 of the search carried out on September 24, 2021, at the PubMed data base [144] with the keywords "Blue Scintillators", "Blue Scintillators Toxicity" and "Scintillators PDT" (top), "Scintillators" and "Scintillators Dosimetry" (bottom).

Given the promising applications of blue absorbing PS mentioned above (miniSOG among them) and the constant development of new and more efficient PS, we believe in a crescent demand for new scintillators capable of efficiently emitting in this region. A keyword search on the PubMed website shows that the science of scintillating materials is a highly developed area with a remarkable increase in publications in the last decade (**Figure 24**). At the same time, it is possible to notice that most of those publications are related to the discovery

and development of materials for dosimetry, with the development of materials for biological applications left out (**Table 7**). Notably, the only publication that resulted from the search for "Blue + Scintillators + PDT" refers not to a blue-scintillator but a blue-photosensitizer (methylene blue).

Table 7: Total number of results of the search carried out on August 21, 2023, at the PubMed data base [144] with the keywords "Blue Scintillators", "Blue Scintillators Toxicity", "Scintillators PDT", "Scintillators" and "Scintillators Dosimetry".

Search	Results
Scintillators	15,127
Blue + Scintillators	158
Blue + Scintillators + Toxicity	11
Scintillators + PDT	55
Blue + Scintillators + PDT	2
Scintillators + Dosimetry	5,981

In our collaboration with Dr. Alessandro Lauria (Laboratory for Multifunctional Materials, Department of Materials, ETH-Zürich), we expected to use his research group's expertise and infrastructure to contribute new findings regarding blue scintillator-PS materials. We were particularly interested in his vast experience with hafnium dioxide (HfO_2). Dr. Lauria and his group have demonstrated that hafnia nanocrystals present stability in biological environments and high biocompatibility when doped with rare earth[145]. Hafnium dioxide nanocrystals' radioluminescence reveals a rich and evolving optical feature. A complete spectral analysis of its broad luminescence spectrum reveals several emission components in the visible and UV regions that can have their energy and intensity conveniently manipulated by titanium impurities[146]. The emission properties of titanium doped hafnia have been investigated by radioluminescence measurements, revealing an active role of calcination in increasing the intensity of the blue emission spectrum after calcination at 1000 °C. The possibility of controlling the luminescence output through the choice of the dopant concentrations, as well as of the calcination temperatures, provides a tool to obtain a reduction of nonradiative channels and an efficient charge transport to the optically active centers, thus resulting in the improvement of the luminescence efficiency under X-ray irradiation[147]. All these characteristics make HfO_2 a potential high-impact candidate for applications in medical science.

3.2 Methods

3.2.1 Expression and Purification - miniSOG

Protein expression was performed in Bl21 (DE3) pLys competent cells (Novagen) using an LB medium. Cells grew at +37 °C in the presence of 100 mg/L ampicillin. Recombinant gene expression was induced by 0.5 mM IPTG until reaching an OD_{600} of 0.8. Expression was performed at +18 °C for 16 h. Harvested cells were lysed and resuspended in PBS under constant stirring for 20 minutes at room temperature. Afterwards, cells were disrupted in 110S microfluidiser (Microfluidics, Newton, Massachusetts, U.S.A.) at 40 psi. The lysate was centrifuged at 25,000×g (rotor 45 Ti, Optima L-90K Ultracentrifuge, Beckman Coulter International S.A., Nyon, Switzerland), +4 °C for 25 minutes. The soluble fraction of the disrupted cell solution was loaded into a Ni-NTA column system (Qiagen). The column was washed with PBS with an Imidazole gradient until the protein was eluted. The protein solution was then concentrated using a 10 kDa cutoff centrifugal filter unit (Millipore, Burlington, MA, U.S.A.) and loaded into a Superdex75 10/300 GL gel filtration column (G.E. Healthcare Life Sciences, Chicago, IL, U.S.A.) coupled to an Äkta purifier system (G.E. Healthcare). The final protein concentration was determined by UV spectroscopy ($\varepsilon_{280\ nm}$ = 9,970 $M^{-1}.cm^{-1}$).

The purified miniSOG in PBS was aliquoted in 1 ml tubes and freeze-dried to be send to the EHT Muntifunctional Materials Laboratory. Before use, miniSOG was rehydrated over night with the same volume of milli-Q water. The hydrated protein was then centrifuged in 15,000×g for 10 min to remove precipitates. The final protein concentration was determined by UV spectroscopy.

3.2.2 Expression and Purification - miniSOG-PE

miniSOG- (PE) is a new construction of miniSOG in which a sequence of 6 glutamate is added to the protein C-terminal. The amino acid sequence is shown in **Table 8**. Its DNA sequence was synthesized with codon optimisation for *E. coli* expression by GenScript®

Biotech. Subsequent expression and purification procedures were carried out using the BioNMR lab's facilities following the same protocol described for miniSOG.

Table 8: miniSOG-PE aminoacid sequence.

miniSOG-
MEKSFVITDP RLPDNPIIFA SDGFLELTEY SREEILGRNG RFLQGPETDQ ATVQKIRDAI RDQREITVQL INYTKSGKKF WNLLHLQPMR DQKGELQYFI GVQLDGGGGG GEEEEEE

3.2.3 Singlet Oxygen Sensor Green (SOSG)

SOSG was purchased from ThermoFischer. A 5 mM stock solution was prepared by dissolving 100 µg of SOSG in 33 µl of methanol. Working solutions were prepared immediately before use by diluting these reagents in PBS, in the presence or absence of miniSOG, for a final concentration of 1.7 µM. A 1 mM stock solution of Fluorescein (Acros Organic) was prepared in methanol. A 1.7 µM working solution was prepared in PBS and used as a reference for the most intense SOSG fluorescence. miniSOG solution was prepared by diluting previous freeze-dried miniSOG-PBS samples in miliQ water.

3.2.4 UV-visible spectroscopy

UV-visible spectroscopy (UV-vis) was carried out on a Jasco V-660 UV-visible spectrometer in a 1 cm optical path quartz cuvette.

3.2.5 Photoluminescence spectroscopy

Photoluminescence (PL) and photoluminescence excitation (PLE) measurements were performed using a 90°-optical geometry Jasco FP-8500 spectrofluorometer (Tokyo, Japan). All photoluminescence measurements were collected at room temperature in 10 × 10 mm^2 quartz cuvettes (Thorlabs, Bergkirchen, Germany). Excitation wavelength were 372 nm for SOSG (previous LED exposure), 504 nm for SOSG and Fluorescein, and 447 nm for miniSOG. The $NaLuF_4$:Tm were excited at 260 and 356 nm, $NaLuGdF_4$:Ce were excited at 255 nm, and hafnia were excited at 275 nm.

3.2.6 Pure and Ti-doped HfO_2

The pure and Ti-doped HfO_2 nanoparticles were prepared through a microwave-assisted solvothermal synthesis, as described in reference [148]. Briefly, benzyl alcohol solutions of each precursor ($HfCl_4$ 1 M and $TiCl_4$ 0.1 M) were prepared as stock solutions. Each precursor was initially dissolved in five molar equivalents of methanol and stirred until the solution turned clear before the final addition of solvent required to reach the desired concentration. Subsequently, in a 10 mL microwave glass tube, the different stock solutions were mixed in the quantities specified in Table 9 to reach the desired composition with a total amount of precursor of 5 mmol. The mixture was then completed to 1.5 mL with benzyl alcohol and stirred. Finally, 2.5 mL of a 0.5M HCl solution in benzyl alcohol was used to yield a volume of 4 mL of clear reacting mixture. The vial was sealed with a Teflon lid and heated in a Discover SP CEM microwave (Kamp-Lintfort, Germany), with the subsequent steps 100 °C, 1 min; 200 °C, 1 min; 260 °C, 14 min. During these steps, the pressure rose to a final maximum value of 17 bars. After the synthesis, the formation of a white product was observed. The reaction mixture was then washed twice with diethyl ether, and the product was collected by centrifugation (4,000×rpm, 10 min). The centrifuged particles were dispersed in 5 mL of milli-Q water, yielding a transparent dispersion. Part of the dispersion was dried for characterization.

Table 9: Summarized solvothermal synthesis for HfO_2:Ti.

% Ti	0	0.1	0.5	0.75	2	3	6
$HfCl_4$ (1 M)	500 µl	499 µl	498 µl	496 µl	490 µl	485 µl	470 µl
$TiCl_4$ (0.1 M)	0 µl	5 µl	25 µl	37.5 µl	100 µl	150 µl	300 µl
Benzyl Alcohol	1 ml	996 µl	977 µl	967 µl	910 µl	865 µl	730 µl
Stirring							
HCl (0.5 M)	2.5 ml						

3.2.7 LED exposure

LED exposures were performed using Thorlabs M375L4 (375 nm) and M455L3 (455nm), operating at 70 mW/cm^2 and 17 mW/cm^2. The entire experiment was performed in a dark room.

3.2.8 X-ray diffraction (XRD)

All XRD measurements were performed using powders of the samples and collection in reflection mode (Cu Kα radiation at 45 kV and 40 mA) on an Empyrean diffractometer from PANalytical (Almelo, Netherlands).

3.2.9 Scanning Electron Microscopy (SEM)

SEM was carried out using a Zeiss Leo Gemini 1530 microscope using a 5 keV electron beam. The samples were prepared by dropping 10 µL of nanocrystals dispersion on lacey carbon Au grids and letting them dry. Finally, the samples were coated with a 3 nm layer of Pt.

3.2.10 Attenuation Total Reflection Infrared (ATR-IR)

ATR-IR spectra were recorded on a Bruker Alpha-P spectrometer on solid powder samples.

3.2.11 Thermogravimetric analysis (TGA)

TGA curves were measured by a Mettler Toledo TGA/DSC 3+ system using ceramic crucibles. Two measurements were carried out, one in atmospheric air and the other under a N_2 flux of 10 ml min^{-1}. For both assays, the heating rate set was 10 °C min^{-1}.

3.2.12 Atomic Force Microscopy (AFM)

AFM imaging was carried out using a Bruker Dimension Icon AFM by Dr Shivaprakash N. Ramakrishna at Laboratory for Soft Materials and Interfaces (ETH–Zurich).

3.2.13 Dynamic Light Scattering (DLS)

The hydrodynamic radius and ζ-potential of the nanoparticles were determined by the dynamic light scattering (DLS) equipment Zeta Sizer system (Malvern Instruments, U.K.) in the Laboratory of Soft Materials and Interfaces, led by Prof. Lucio Isa. Data were collected at a fixed angle and wavelength of 173° and 633 nm (He−Ne laser), respectively. The measurements were performed with three samples for each condition. The sample preparations for examining the interaction between the nanoparticles and CA or proteins were conducted as detailed in Table 10. The volume of each constituent was calculated to achieve final concentrations of PBS 1×, HfO_2:Ti(3%) 1.2 mg/ml, CA 80 µmol/l and protein 455 µmol/l.

Table 10: Summarized sample preparation for HfO2:Ti(3%) ligand and stability assay.

Sample	Milli-Q Water	PBS 10×	Ligand	HfO_2:Ti(3%)	Total volume
HfO_2:Ti(3%) in H_2O	4.7 ml	--	--	300 µl	5 ml
HfO_2:Ti(3%) in PBS	4.2 ml	500 µl	--	300 µl	5 ml
HfO_2:Ti(3%)@CA in H_2O	4.5 ml	--	200 µl (CA)	300 µl	5 ml
HfO_2:Ti(3%)@CA in PBS	4.0 ml	500 µl	200 µl (CA)	300 µl	5 ml
HfO_2:Ti(3%)@miniSOG in PBS	3 µl	7 µl	930 µl (miniSOG)	60 µl	1 ml
HfO_2:Ti(3%)@miniSOG-PE in PBS	3 µl	7 µl	930 µl (miniSOG-PE)	60 µl	1 ml

3.3 Results

3.3.1 miniSOG Characterization

Some optical tests were conducted to evaluate whether miniSOG kept its structure and function after the freeze-dry and later hydration process. The absorbance and fluorescence

spectra of miniSOG are shown in **Figure 25**. The absorbance and fluorescence spectra demonstrated the expected profile for FMN bound to miniSOG protein.

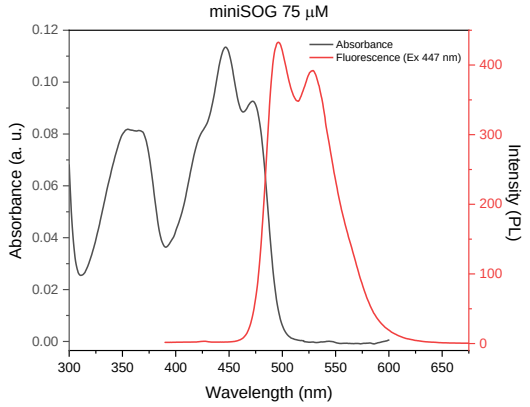

Figure 25: MiniSOG absorbance (dark grey) and fluorescence (red) profile. The fluorescence spectrum was recorded upon excitation at 447 nm.

MiniSOG capacity to produce ROS was analysed after rehydration using SOSG as a probe. The effect of irradiating miniSOG and the consequent generation of singlet oxygen ($^1O_2$) was assessed using two different LEDs corresponding to miniSOG main excitation wavelengths: UV (375 nm) and blue (455 nm). The fluorescence spectra of SOSG in the presence of 75 µM miniSOG after different times of exposure to blue LED are presented in **Figure 26a**. The increase in the fluorescence intensity after one hour of light exposure indicated that SOSG was activated by $^1O_2$. This result and the absorbance and fluorescence spectra of miniSOG (**Figure 25**) indicate its correct folding and maintenance of its function, allowing further studies with the freeze-dried and rehydrated protein.

Figure 26a also shows that SOSG presented a background 525 nm emission before irradiation. Noticeable decreases in the fluorescence intensity were observed for more prolonged exposure than one hour, suggesting photodegradation (**Figure 26b**). A more detailed assay is shown in **Figure 26c**. For a 70 mW/cm^2 irradiance and in the presence of 93 µM miniSOG, the SOSG maximum intensity progressively increased with exposure time and reached its maximum after 20 min of irradiation. After 30 min of irradiation, the sample was placed in ice and protected from light for 160 min before another fluorescence acquisition. The maintenance of the fluorescence intensity after this period (**Figure 26c**), and even after one day (data not shown), proved that SOSG could store information for a long time. A control curve was recorded for SOSG in PBS without miniSOG. It shows a relatively slight increase in the

fluorescence intensity upon light exposure, suggesting low sensitization of SOSG by the employed wavelength.

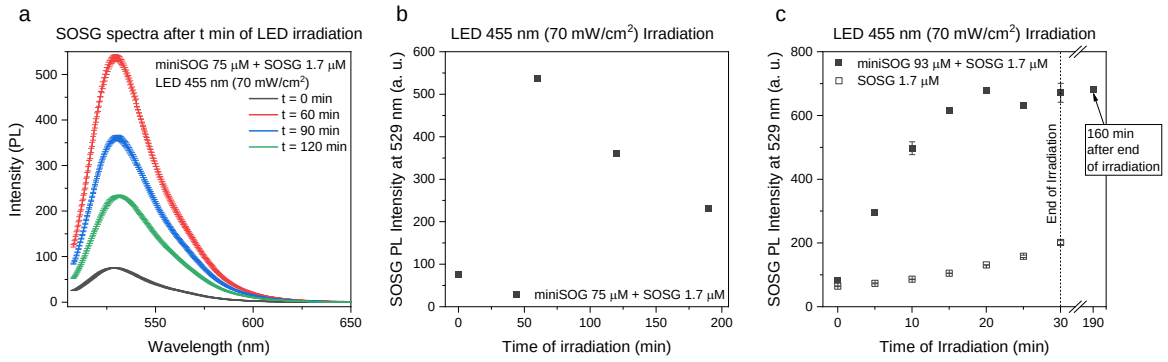

Figure 26: a) SOSG fluorescent spectra in the presence of 75 µM miniSOG after irradiation at 455 nm (70 mW/cm²) for different exposure times. b) SOSG fluorescence intensity at 529 nm in the presence of 75 µM miniSOG after 455 nm (70 mW/cm²) irradiation for 0-, 60-, 120- and 180-min. c) SOSG fluorescence intensity at 529 nm in the presence of 75 µM miniSOG after 455 nm (70 mW/cm²) irradiation for successive 5 min intervals up to 30 min, and after 160 min in the dark.

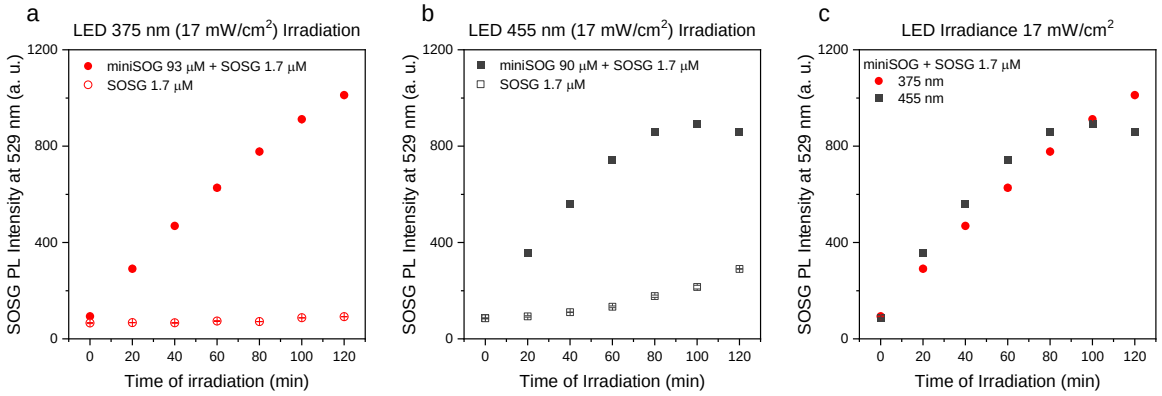

Figure 27: a) SOSG fluorescence intensity at 529 nm in the presence of 93 µM miniSOG after 375 nm (17 mW/cm²) irradiation for every 20 min up to 120 min. b) SOSG fluorescence intensity at 529 nm in the presence of 90 µM miniSOG after 455 nm (17 mW/cm²) irradiation for every 20 min up to 120 min. c) Comparison between the rise of $^1O_2$ production curves over time upon irradiation at 375 nm (red) and 455 nm (dark grey).

For the subsequent characterization, the LED irradiance was set to 17 mW/cm² (the maximum irradiance of 375 nm LED). As shown in **Figure 27a**, the 375 nm LED also induced $^1O_2$ formation by miniSOG. On the other hand, a comparison of **Figure 27a** and **b** revealed that SOSG interaction was less pronounced for this photon energy compared to 455 nm. The different interactions of SOSG for different photon energies might explain the plateau and subsequent quenching of its fluorescence observed upon 455 nm irradiation and not upon 375 nm irradiation. Since this phenomenon was observed for exposure to 455 nm, both with 17 and 70 mW/cm² (**Figure 26c** and **Figure 27b**), we concluded that it was not power-dependent.

Figure 27c compares the rise of $^1O_2$ production curves over time upon irradiation at 375 nm and 455 nm.

To better understand the behaviour of miniSOG-induced $^1O_2$ generation upon excitation at the two different wavelengths, the previous result (**Figure 27c**) was corrected by the energy of the light, SOSG baseline, and transmittance (**Figure 28**). The conversion of the irradiation time into the density of photons was calculated according to

Equation 1 below. **Figure 28a** shows similar behaviour of $^1O_2$ generation for sample exposure up to $3.0x10^{16}$ photons/cm^2, regardless of the photon energy. **Figure 28b** exhibits the difference in the intensities of the samples containing miniSOG and controls. Therefore, the contribution of SOSG fluorescence due to its interaction with light is negligible. Last, **Figure 28c** shows the same corrected intensity over the density of absorbed photons (

Equation 2). With this result, we concluded that miniSOG could produce $^1O_2$ when exposed to the 375 nm LED light, and it was also more efficient in converting absorbed photons into $^1O_2$ than when exposed to the 455 nm LED.

Equation 1

$$Density\ of\ photons = \frac{Irradiance \times Time}{Photon\ energy}$$

Equation 2

$$Density\ of\ absorbed\ photons = Density\ of\ photons \times (1 - Transmittance)$$

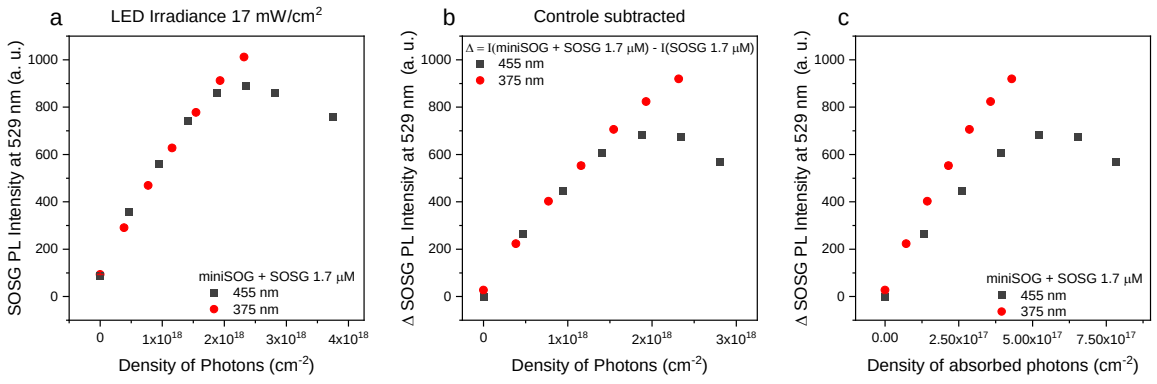

Figure 28: a) SOSG fluorescence intensity at 529 nm in the presence of miniSOG after 375 nm (red) and 455 nm (dark grey) over the density of photons. b) Subtraction of the SOSG fluorescence intensity at 529 nm in the presence of miniSOG and the control over the density of photons. c) Subtraction of the SOSG fluorescence intensity at 529 nm in the presence of miniSOG and the control over the density of absorbed photons.

Partial conclusion

The measured response of miniSOG to UV light has not been previously reported. Considering the traditional applications of PDT, a PS that is excited in the UV may not be very interesting since the penetration of UV light into the human body is even shallower than the penetration of the blue wavelength. However, considering applications with more advanced technologies, including the one proposed in this work, the possibility of exciting the PS at different wavelengths facilitates the search for new compatible scintillators. Moreover, a better understanding of the properties of each element of the system leads to the engineering of a more efficient nanoparticle-photosensitizer complex.

3.3.2 Hafnia (HfO_2)

Dr. Lauria and his Ph.D. student Xavier Guichard have widely studied Hafnia nanoparticles in the Multifunctional Materials (MFM) group at ETH Zurich. Hafnia was the material proposed in this project due to its broad emission, from 400 to 600 nm (**Figure 29a**), and its reported scintillation, mainly controlling the Ti-related luminescence output through the choice of the dopant concentrations[147]. Here, the hafnia was synthesized employing a microwave method established by Guichard [148], varying the Ti doping from 0% to 6%. Microwave synthesis overcomes solvothermal because it produces luminescent nanoparticles without a calcination step.

The luminescence as a function of Ti concentration in hafnia nanoparticle dispersions can be observed in **Figure 29b**. The assay showed that the luminescence increased with increasing Ti-doping up to 3%. In the presence of 6% Ti, the luminescence seemed quenched. The luminescence increased linearly between 1% and 3% Ti-doping. This result corroborates previous results obtained by MFM members. **Figure 29a** shows the intensity gain in PL and PLE for the hafnia doped with 3% Ti compared to the non-doped hafnia. The contour plots of the same particle formulations (**Figure 29c** and **d**) show their emission and excitation regions, highlighting the spectral artifacts. It is worth noting that both PL and PLE of the pure sample seemed similar to that of the Ti-doped sample. This could possibly originate from the adventitious presence of traces of Ti in the Hf precursor, as already reported for other precursors, namely Hf t-butoxide [149], leading to analogous optical properties.

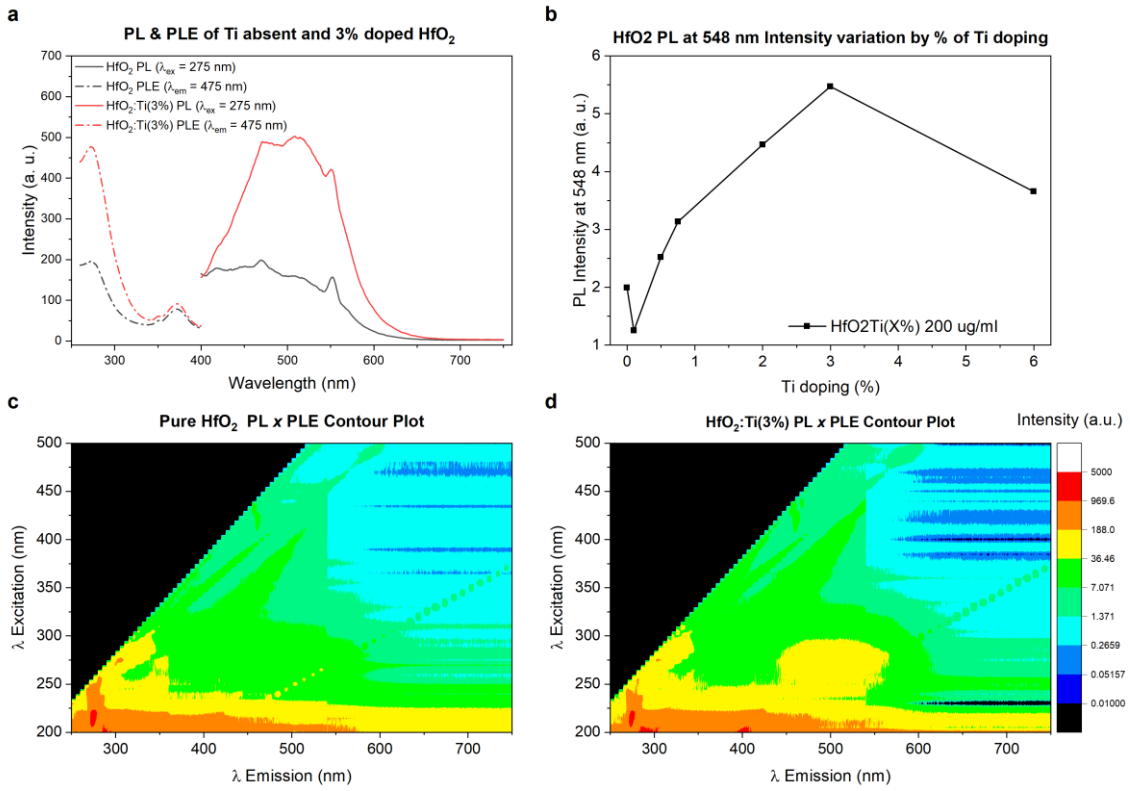

Figure 29: Study of the influence of Ti doping on the optical properties of HfO_2 nanoparticle dispersions in water (200 ug/ml). a) Comparison of excitation (dot-dash) and emission (solid line) spectra of non-doped (dark grey) and 3% Ti-doped (red) HfO_2. b) Variation of photoluminescence intensity at 548 nm as the percentage of Ti increases. Contour plots of the photoluminescence intensities for the c) HfO_2 and d) HfO_2:Ti(3%). The intensity scale is the same for c) and d).

Since the best luminescence efficiency was observed for 3% Ti-doping, the morphological and structural characterization was carried out for this composition and compared to the undoped one. **Figure 30a** shows the powder X-ray diffraction (PXRD) pattern recorded from both dried samples. The HfO_2 monoclinic structure was recognised in both samples, irrespective of doping. No additional phases, such as titanium oxide, were detected regardless of the Ti content, confirming the incorporation of Ti ions in the HfO_2 lattice. Besides identical crystal symmetry, the samples showed a similar broadening of the diffraction peaks, indicating that the dopant did not affect the crystal size. Crystal average sizes, calculated by the Sherrer formula, were 8 and 9 ± 1 nm for the HfO_2 and HfO_2:Ti(3%), respectively (**Table 11**). The absence of specific functional groups in ATR-IR analysis (**Figure 30b**) revealed no solvent polymerisation side product formation during the microwave reaction[148, 150]. This data agrees well with the absence of blue fluoresce from benzyl alcohol polymerization products, such as poly(phenylene methylene), [151] in the PL spectra (**Figure 29a**).

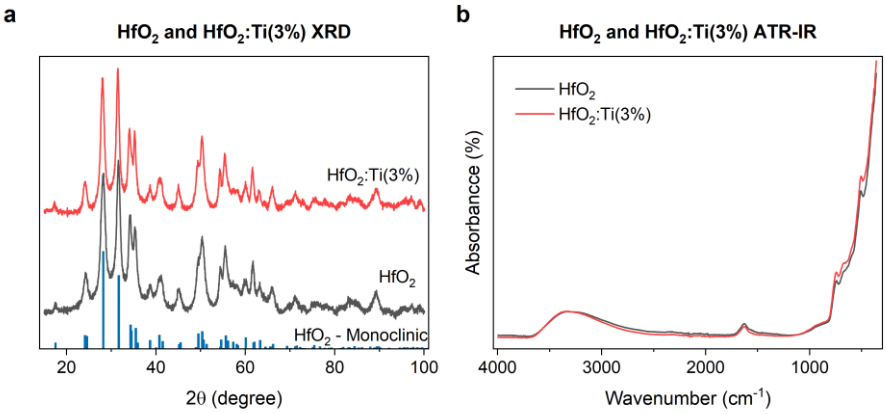

Figure 30: Study the crystalline structure and chemical composition of doped and undoped nanoparticles in powder form. a) PXRD pattern of undoped HfO_2 (dark grey) and HfO_2:Ti(3%) (red). The pattern of monoclinic (blue bars, PDF 04-014-7409) is shown as a reference. b) ATR-IR of HfO_2 (dark grey) and HfO_2:Ti(3%) (red).

Table 11: Scherrer analysis held on the (111) peak at 31.5 degrees.

	Crystal Size (nm)
HfO_2	8 ± 1
HfO_2:Ti(3%)	9 ± 1

SEM images of HfO_2:Ti(3%) (**Figure 31**) evidenced the occurrence of 40 to 60 nm particles agglomerates in the dried state. Nevertheless, as-synthesized nanoparticles were readily dispersed in water (**Figure 32**), and DLS analysis (**Table 12**) revealed a particle hydrodynamic diameter of 24 nm. Indeed, the observed clustering of the nanoparticles in SEM images may occur during drying. As expected for particles stabilized by electrostatic interactions, the colloidal behaviour of HfO_2:Ti(3%) in water was not reproducible in PBS.

Figure 32 shows the comparison of 1.2 mg/ml hafnia dispersions in pure water and high ionic strength saline of PBS. The dispersion in milli-Q water, which expressed acidic conditions[152], was clear and stable for months. Conversely, after adding PBS, the HfO_2:Ti(3%) dispersion instantly became foggy and flocculated within less than 30 min. Flocculation and precipitation occurred due to the salts in the solution and the pH shift. This observation was further supported by DLS measurements (**Table 12**). In PBS, the hydrodynamic radius increased by 3 orders of magnitude due to the severe aggregation; the PDI almost doubled, suggesting higher size polydispersity in the sample. With the addition of the buffer, the pH increased from 3.4 to 7.4, and the ζ-potential naturally turned from positive to negative as the isoelectric point (IEP) was surpassed (IEP~5) [153]. The conductivity was directly proportional to

the number of ions in the solution, which was higher in PBS. Monitoring these dispersions over a week evidenced the aggregation process of the nanoparticles in PBS (**Figure 33**), where a white precipitate was visible at the bottom of the vial, as expected when the particle surface charge was suppressed at the isoelectric pH.

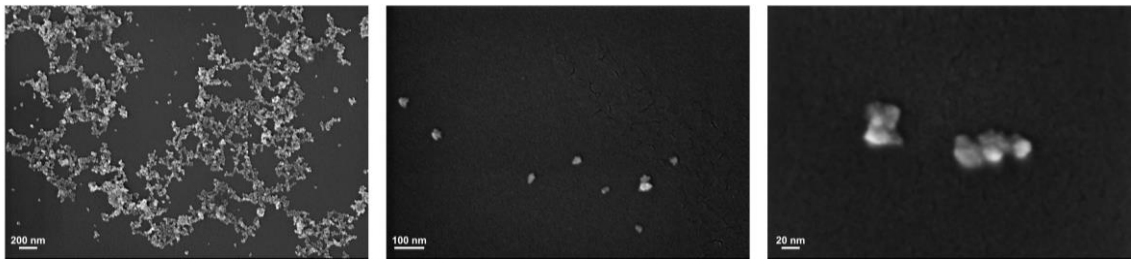

Figure 31: SEM images of HfO_2:Ti(3%) at different magnifications.

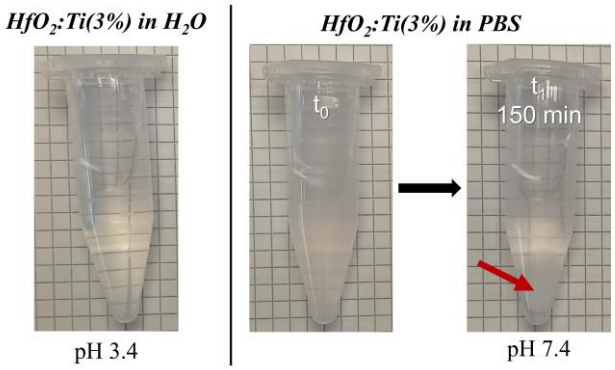

Figure 32: Stability of the HfO_2:Ti(3%) in PBS. Left: stable dispersion of the nanoparticles in milli-Q water. Right: dispersion of the nanoparticles in PBS just after mixture (t_0) and after 2 h stirring followed by 30 min resting (t_1).

3.3.3 HfO_2:Ti(3%)@Citric Acid (CA)

A functionalization step was attempted in order to prevent the HfO_2:Ti(3%) agglomeration in PBS. Low molecular weight carboxylic acids were used as particle interaction modifiers since they readily adsorb to metal oxides-aqueous interfaces. The affinity for surfaces generally follows the number of carboxylate groups. Thus, citric acid (CA), the tricarboxylic acid, was chosen to investigate its suitability as stabilizing ligand for HfO_2:Ti(3%) in PBS. Metal oxide colloidal dispersions, such as FeO_2, TiO_2, and HfO_2, have been previously studied in the presence of CA [153-155]. CA can perform as a reducing agent, size controller, and steric stabilizer when adsorbed to the particles' surfaces. Besides, citrate ions play an important role

in biology. They act as anticoagulants in the blood and as a stabilizer for apatite nanocrystals in bones [156, 157].

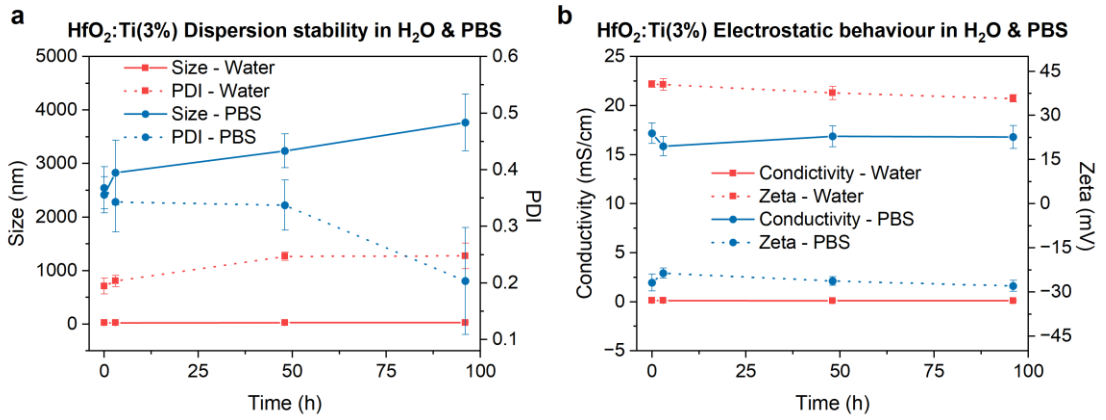

Figure 33: Evaluation of HfO_2:Ti(3%) dispersion stability in milli-Q water and PBS over a week using DLS measurements. a) Variation of the hydrodynamic size (straight line) and PDI (dash-dot) of the HfO_2:Ti(3%) in milli-Q water (red) and PBS (blue) over time. b) Variation of the conductivity (straight line) and ζ-potential (dash-dot) of the HfO_2:Ti(3%) in milli-Q water (red) and PBS (bleu) over time.

Table 12: DLS analysis of HfO_2:Ti(3%) dispersion in milli-Q water and PBS.

HfO_2:Ti(3%) in	H_2O	PBS
Hydrodynamic diameter	24.2 ± 0.1 nm	2400 ± 300 nm
PDI	0.19 ± 0.01	0.37 ± 0.03
ζ-potential	40 ± 1 mV	-27 ± 3 mV
Conductivity	0.133 ± 0.001 mS/cm	17 ± 1 mS/cm

The HfO_2:Ti(3%) nanoparticles were added to 80 mM CA solutions using either milli-Q water or PBS as a solvent. High turbidity could be instantly observed (**Figure 34** - t_0) in both cases. However, no precipitation was observed after stirring for two hours and 30 minutes resting (t_1). Even though centrifugation could accelerate their precipitation, the particles were still dispersible in milli-Q water and PBS. After a washing step, the excess CA was removed, and the colloidal dispersions became clear again. The final pH values were 2.8 and 7.1 for the milli-Q water and PBS dispersion, respectively. Curiously, DLS data (**Table 13**) showed a higher hydrodynamic radius for HfO_2:Ti(3%)@CA dispersed in milli-Q water than in PBS. Also, the PDI was higher for the coated nanoparticles in water, although both had a relatively good polydispersity (PDI < 0.3). The conductivities did not change for the coated samples,

suggesting an efficient washing of the CA in excess and that CA remained tightly bound at the surface of the nanoparticles rather than in an adsorption equilibrium.

The ζ-potential was the same for the HfO_2:Ti(3%)@CA in water and PBS. The ζ-potential of nanoparticles explains their surface charge and can be affected by the pH and ionic strength of the surrounding medium. In this case, it seems counterintuitive, yet extremely promising, that the nanoparticles coated with citric acid would have the same ζ-potential in two different pH conditions. One possible explanation is that the citric acid coating on the nanoparticles plays a buffering effect, which helps to maintain the ζ-potential at a constant value across different pH conditions. Citric acid is a weak acid with a pKa_1 of ca. 3.13 and pKa_3 of ca. 6.39 [153], which means it can act as a buffer in solutions with pH values around its pKa. In the case of the nanoparticles in milli-Q water with pH 2.8, the citric acid coating would be mostly protonated and have a positive charge, resulting in a positive ζ-potential. In the saline phosphate buffer with pH 7.1, the citric acid ligands would be mostly deprotonated and have a negative charge, resulting in negative ζ-potential. However, the buffering effect of citric acid may help to maintain the ζ-potential at a constant value of -16 mV in both conditions.

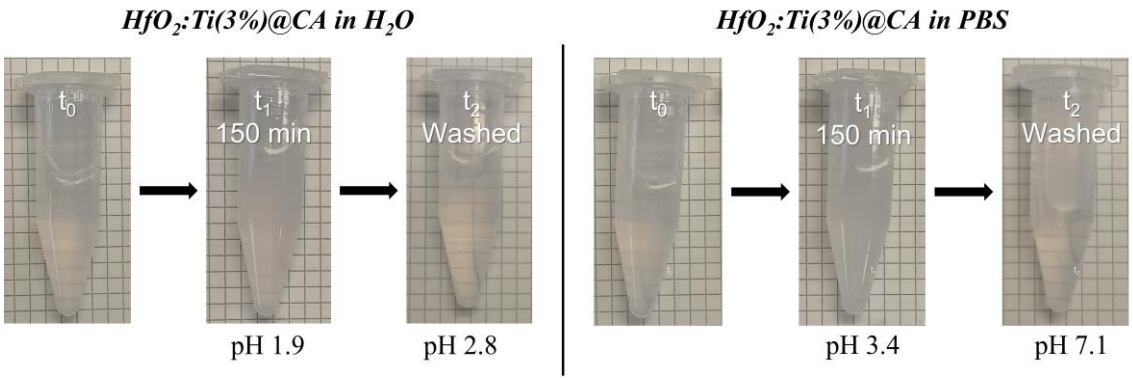

Figure 34: HfO_2:Ti(3%) functionalized with citric acid in PBS. Left: dispersion of the nanoparticles in water. Right: dispersion of the nanoparticles in PBS. t_0 was recorded right after the mixture of the nanoparticles with the citric acid solution, t_1 was recorded after 2 h stirring and 30 min resting, and t_2 was recorded after removing the excess citric acid by centrifugation and redispersion.

After 5 days (**Figure 35**), the PDI increased, and the ζ-potential decreased, indicating that the samples aged similarly in both conditions. However, within the same period, the conductivity remained the same and the hydrodynamic radius did not change, indicating the stability of the CA coating of the nanoparticles' surface. The particles coated with CA remained colloidal in PBS and milli-Q water, as they would in milli-Q water without CA. With this result, we concluded that CA coating displaced the HfO_2:Ti(3%) isoelectric point, stabilizing them in the neutral pH of PBS.

Table 13: DLS results of functionalized HfO2:Ti(3%)@CA dispersion in H_2O and PBS.

HfO_2:Ti(3%)@CA in	H_2O	PBS
Hydrodynamic diameter	193 ± 3 nm	46 ± 1 nm
PDI	0.261 ± 0.003	0.17 ± 0.01
ζ-potential	-16.3 ± 0.2 mV	-16 ± 2 mV
Conductivity	0.232 ± 0.001 mS/cm	18 ± 1 mS/cm

Carboxylic acids react with mineral surfaces through different coordination modes of the carboxylate ($-COO^-$) group to metal ions[158]. The nature of the complex formed between the ligand and the particle surface was characterized using ATR-IR. In **Figure 36**, citric acid infrared spectra in different environments can be compared. The similarity between the CA and CA in PBS spectra indicated that CA was not interacting with any salt in PBS. However, the changes in the P–O stretching (1,200-1,100 cm^{-1}) and bending (1,000-900 cm^{-1}) vibration modes observed in the PBS spectra due to the presence of HfO_2:Ti(3%) partially explained the destabilization of the particles in this medium. The same bands, present in the FTIR of PBS alone, were not observed in the presence of the nanoparticles but rose again when coated with CA. The free carboxylic (C═O) absorption band at 1,740 cm^{-1}, and the O–H stretching band at 3,287 cm^{-1}, present in the CA spectra, disappeared in the HfO_2:Ti(3%)@CA in PBS spectrum, indicating that there was no free citric acid in the mixture.

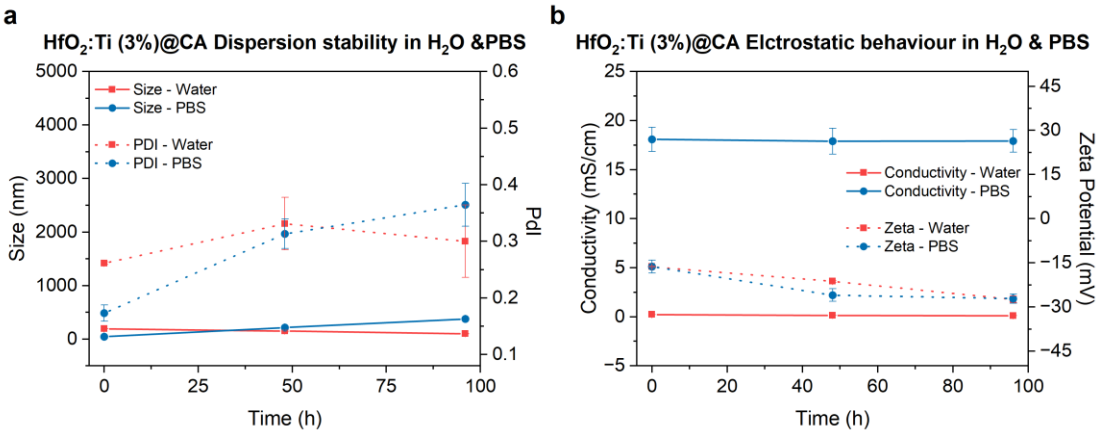

Figure 35: Evaluation of HfO_2:Ti(3%) coated with CA dispersion in water and PBS over a week using DLS measurements. a) Variation of the size (straight line) and PDI (dash-dot) of the HfO_2:Ti(3%)@CA in H_2O (red) and in PBS (bleu) throughout the time. b) Variation of the conductivity (straight line) and ζ-potential (dash-dot) of the HfO_2:Ti(3%)@CA in H_2O (red) and in PBS (bleu) throughout the time.

In addition, two bands were present for the later sample at 1,630−1,580 and 1,450−1,390 cm^{-1}, which may relate to the COO^- groups' asymmetric and symmetric stretching vibrations, respectively. Several studies have shown the correlation of the frequency separation between the COO^- antisymmetric and symmetric stretches ($\Delta\nu_{a-s}$) and the types of coordination of the COO^- group to metal cations[158-160]. The four possible modes of interaction are sketched in **Figure 36**. Our result showed a $\Delta\nu_{a-s}$ of approximately 166 cm^{-1}, which was included in the bridging bidentate range. In this mode, the carboxylate group coordinates with the metal ion through both oxygen atoms of the carboxylate group.

These promising results about HfO_2:Ti(3%) stabilization in PBS by the citric acid coordination led us to question whether the carboxylic groups present in the aminoacids' sidechain could also coordinate to HfO_2:Ti(3%).

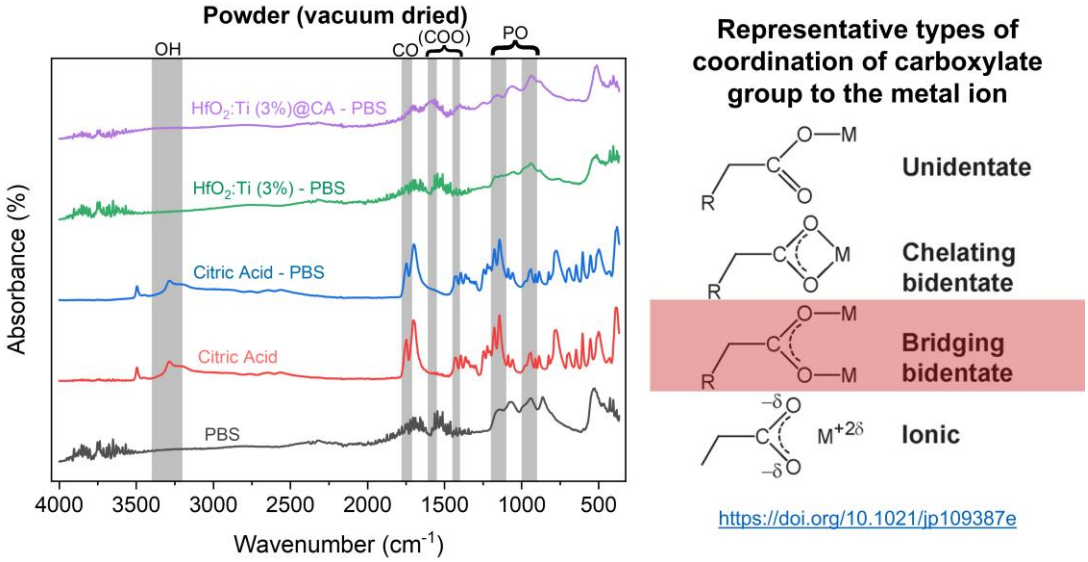

Figure 36: Investigation of the chemical bonds that promote the interaction between HfO_2:Ti(3%) and citric acid. Left: ATR-IR of PBS (dark grey), citric acid (red), citric acid in PBS (blue), HfO_2:Ti(3%) in PBS (green), and HfO_2:Ti(3%)@CA (violet). Right: Scheme of the coordination types of carboxylate group to metal ions adapted from [158]. The red rectangle highlights the CA coordination mode to HfO_2:Ti(3%).

3.3.4 miniSOG-PE

Results so far showed that carboxylic groups of citric acid can coordinate with HfO_2:Ti(3%), generating the HfO_2:Ti(3%)@CA complex. This complex behaved as a colloidal solution in PBS akin to HfO_2:Ti(3%) in milli-Q water. It is of great importance that the nanoparticles form a stable dispersion in PBS since this medium mimics the human physiologic environment. Our next attempt was to promote the binding between HfO_2:Ti(3%) and the

functional protein of interest (miniSOG) by a simple mixing procedure with no further chemical modifications. miniSOG carries 8 aspartates (D) and 8 glutamates (E) (**Figure 37b**) in its primary structure. These amino acids have a carboxylic group as sidechain and have the potential to bind to HfO_2:Ti(3%). However, most of the aminoacids' sidechains are not accessible for other interactions apart from those that determine the protein structure and function. Therefore, to increase the probability of miniSOG binding to the nanoparticles, a sequence of 6 glutamates was added to its C-terminal. We named the 6 glutamate tag Poly-E (PE). The Poly-E sequence was added to the protein DNA sequence, which was expressed by heterologous expression. Finally, the new protein was purified using size exclusion chromatography, and its structure was calculated using AlphaFold. **Figure 37a** illustrates the miniSOG-PE structure, highlighting the Poly-E glutamates' sidechains.

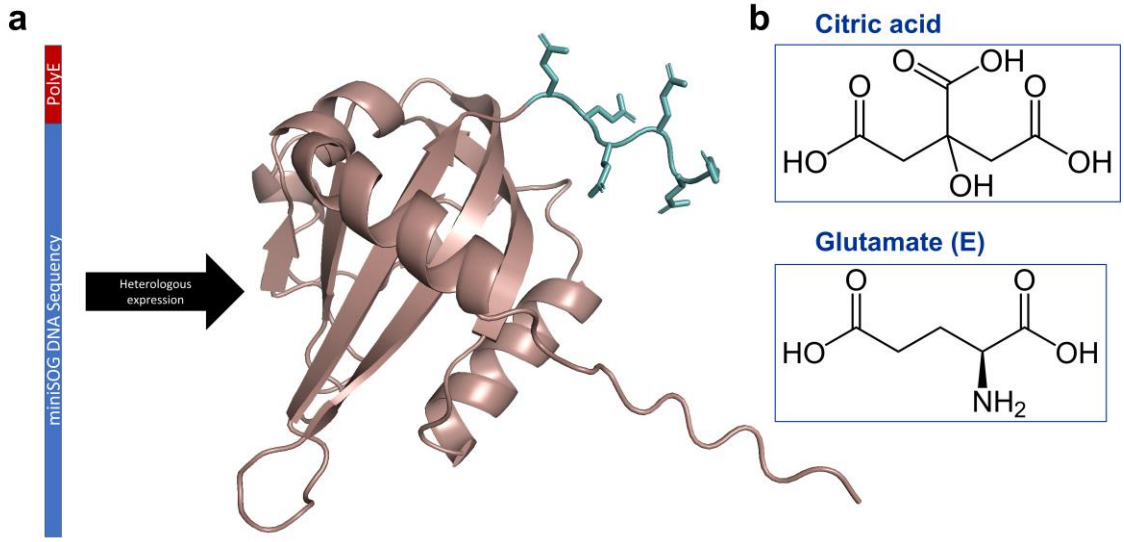

Figure 37: a) Sketch of miniSOG DNA sequence with the Poly-E modification followed by the miniSOG-PE final structure determined using AlphaFold. The light blue region highlights the six glutamates in the protein's C-terminal. b) Sketch of citric acid and glutamate molecules.

Structural and functional characterizations of miniSOG-PE are yet to be performed. Nonetheless, the optical characterization of miniSOG-PE is promising. miniSOG-PE presented the same excitation and emission bands as miniSOG (**Figure 38**). The luminescence of the protein indicated its correct folding. In this case, it also indicated protein activity. The main difference between the two proteins' optical behaviour was a relative decrease in the intensity of the emission band around 340 nm when excited at 280 nm. These are the excitation and emission bands of the luminescent amino acids: tryptophan, tyrosine, and phenylalanine. Moreover, the decrease in their intensity relative to the intensity of the FMN emission band suggests a more efficient energy transfer from the aromatic amino acids to the FMN. With this

result, we were confident to continue the miniSOG/miniSOG-PE interaction experiments with HfO_2:Ti(3%).

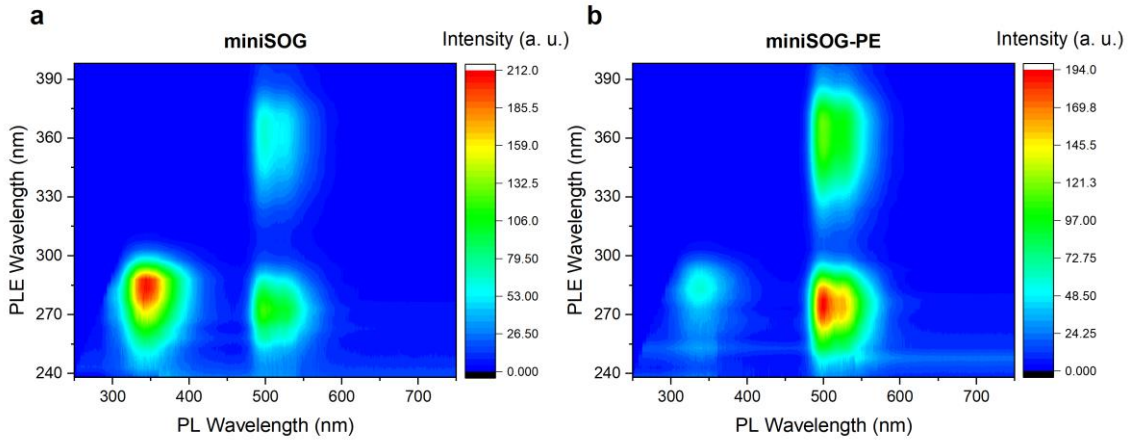

Figure 38: Contour plot of the photoluminescence 3D spectra of the a) miniSOG and b) miniSOG-PE.

3.3.5 HfO_2 + miniSOG/miniSOG-PE

The subsequent experiments investigated whether nanoparticles and proteins would interact by forming a stable connection. Mixtures of nanoparticles with proteins were prepared to evaluate the binding between the miniSOG and miniSOG-PE to the HfO_2:Ti(3%). We repeated the same procedure carried out for the CA-coated nanoparticles. **Figure 39** shows the nanoparticle mixture's flocculation with both proteins (t_0). After the stirring and resting time (t_1), the particles in the presence of miniSOG precipitated, while particles in the presence miniSOG-PE remained stable in dispersion. These two dispersions were centrifuged, and the pellet of nanoparticles with miniSOG-PE had a stronger yellow colour than the pellet of HfO_2:Ti(3%) with miniSOG. Since the yellow colour derives from the protein, it can be inferred that miniSOG-PE interacted more effectively with the HfO_2:Ti(3%) surface than the unmodified miniSOG. The resuspension in PBS (t_2) was also faster and became clearer for the nanoparticles mixed with miniSOG-PE than miniSOG. Before the washing steps, miniSOG concentration was in excess, yielding an intense yellow dispersion. After redispersion (t_2), the yellow colour could not be seen because all the surplus miniSOG was washed out, and the final miniSOG concentration was much lower.

DLS data showed a considerable size increase of HfO_2:Ti(3%) after complexation with the proteins (**Table 14**). The new system grew from the nanometric to the micrometric scale. This size increase was much higher than expected and requires further investigation. However, HfO_2:Ti(3%) with miniSOG-PE kept a low PDI, indicating a nicely dispersed sample.

HfO_2:Ti(3%) with miniSOG, on the other hand, was not a homogenous sample, according to its PDI. The ζ-potential was also more negative for the particles in the presence of miniSOG-PE than miniSOG. These data and the pellet images obtained during the washing (Figure 39) suggest a better coverage of the particles by miniSOG-PE. The conductivity of the solvent was the same for both samples and very similar to the PBS conductivity values.

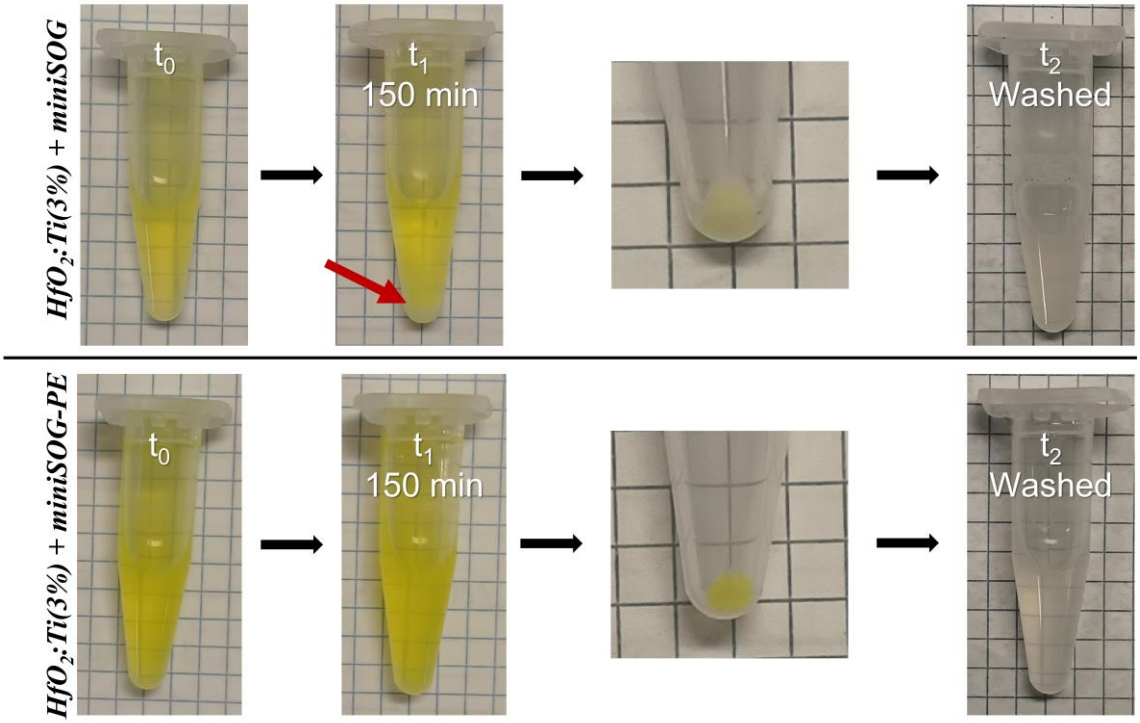

Figure 39: Stabilization of the HfO_2:Ti(3%) in PBS mixed with miniSOG (top) and miniSOG-PE (bottom). t_0 corresponds to the moment just after the dilution of the nanoparticles in the new solution, t_1 images was recorded after 2 h stirring and 30 min resting, and t_2 was recorded after centrifugation and redispersion in PBS.

Table 14: DLS results of HfO2:Ti(3%) mixed with miniSOG and miniSOG-PE in PBS.

HfO_2:Ti(3%) with	miniSOG	miniSOG-PE
Hydrodynamic diameter	1361 ± 130 nm	1128 ± 180 nm
PDI	0.51 ± 0.06	0.29 ± 0.01
ζ-potential	-13 ± 2 mV	-22 ± 2 mV
Conductivity	18 ± 1 mS/cm	18 ± 1 mS/cm

Figure 40a and b shows the DLS results as a function of time, which is likely the most exciting data. HfO_2:Ti(3%)@miniSOG-PE colloidal solution shows long-term stability despite the size increase. During five days, its behaviour was exactly like HfO_2:Ti(3%)@CA, keeping its original size and PDI and showing no evidence of aggregation. The same was not observed

for HfO_2:Ti(3%)@minSOG, which increased in size and decreased the PDI measurement precision, strongly suggesting possible sample precipitation and optical quality degradation. These data analyses made us conclude that the Poly-E tag acts as a binding anchor of the protein suitable for coordination with the nanoparticle. The more negative ζ-potential (**Figure 40c**) HfO_2:Ti(3%)@miniSOG-PE, in the early stages, may also explain the higher stability of this sample, although it has to be remarked that this value is not constant over time. This change might happen due to a very different cause, i.e., protein aging. Once again, the solvent's conductivity (**Figure 40d**) remained the same for both samples throughout the experiment.

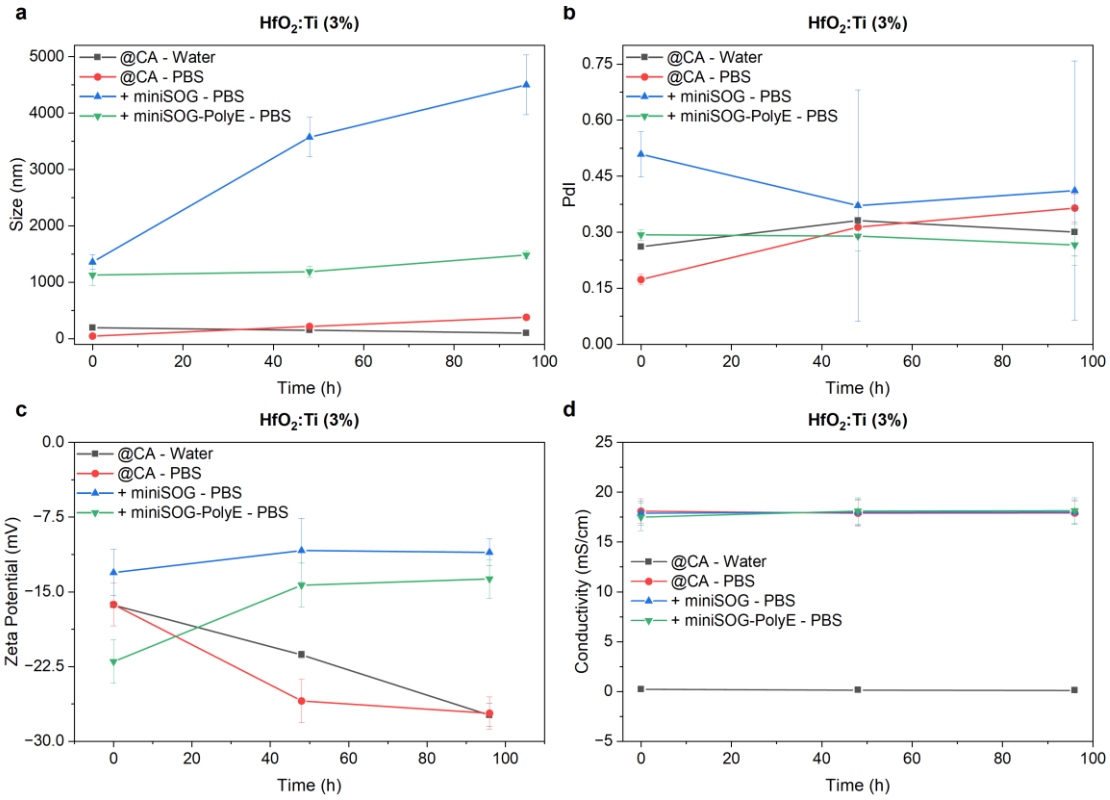

Figure 40: DLS evaluation of HfO_2:Ti(3%) mixed with miniSOG and miniSOG-PE in PBS over a week. Variation of size (a), PDI (b), ζ-potential (c), and conductivity (d).

SEM and AFM images, shown in **Figure 41,** were recorded to determine the morphology of the particle/protein adducts, but, unfortunately, they revealed inconclusive results. From SEM images, it is clear that the drying process causes the agglomeration of the nanoparticles, which can be observed for both particles dried in water and PBS with miniSOG-PE. For the particles mixed with miniSOG, a better dispersion over the substrate was observed. A light grey layer underneath the particles can be observed for both samples containing proteins, although it might reflect the even settling of water-stable unbound nanoparticles, disconnected from protein residues. Even though these analyses do not clearly confirm the DLS results, it is

important to consider that the DLS is a dynamic measurement and better represents the sample's behaviour for the proposed *in vitro* and *in vivo* applications. AFM images possibly reflect better the DLS data. A reasonable size increment could be observed for the HfO_2:Ti(3%) in the presence of the proteins. The particles' size increased from 30 to 50 and 100 nm when mixed with miniSOG and miniSOG-PE, respectively. The samples were prepared by freeze-drying, preventing severe aggregation due to surface tension during drying. Hence, a more even distribution of HfO2:Ti(3%)@miniSOG-PE could be observed. However, more experiments must be performed to further verify the role of Poly-E on protein–nanoparticle binding. Furthermore, no time was available to reproduce the SEM and AFM measurements, and these experiments are yet to be repeated.

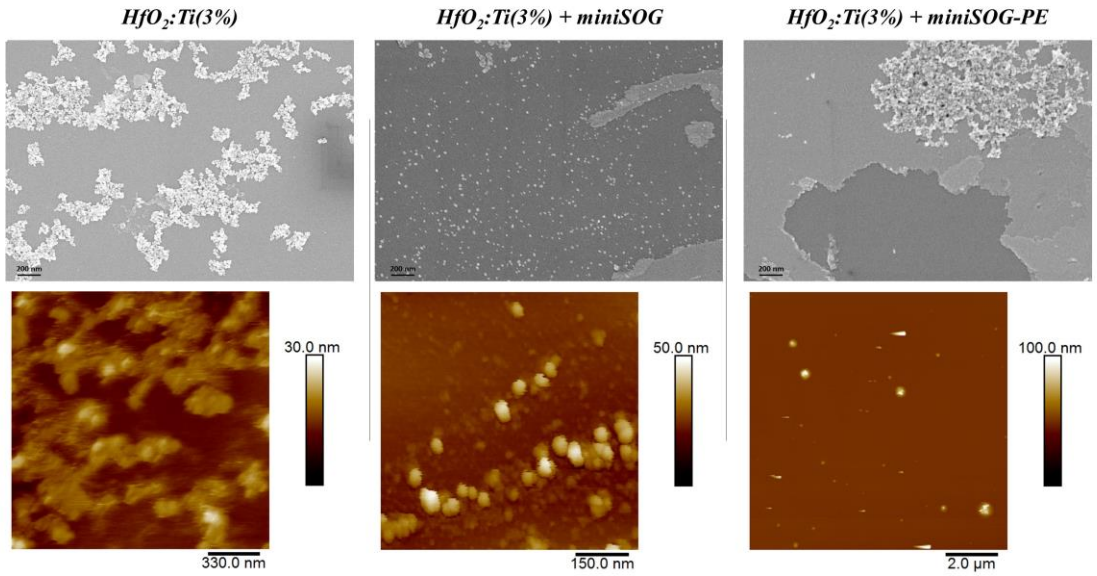

Figure 41: Top: SEM images of HfO_2:Ti(3%) (right), HfO2:Ti(3%)–miniSOG (middle) and HfO_2:Ti(3%)–miniSOG-PE. Bottom: AFM images of HfO_2:Ti(3%) (right), HfO_2:Ti(3%)–miniSOG (middle) and HfO_2:Ti(3%)–miniSOG-PE.

In order to check the functional advantage of the protein−nanoparticle adducts, we tried to study their energy transfer. After the conjugation of either miniSOG or miniSOG-PE with HfO_2:Ti(3%), the energy stored by absorption in the particle hopefully activates the nearby protein either by Förster resonance energy transfer (FRET) or by trivial energy transfer. FRET occurs through the coupling of the dipolar moments of the donor and acceptor, whereas the photon mediated trivial energy transfer occurs through separate events of donor emission and acceptor absorption of photons. Considering the particle as the donor and the proteins as the acceptor, the proteins should be excited by the emission of the HfO_2:Ti(3%). However, in a photoluminescence assay, it was extremely difficult to recognise the energy transfer phenomenon because of the high overlap of the HfO_2:Ti(3%) excitation in the UV range with

the excitation region of the proteins (**Figure 42**). In this way, an X-ray source is needed to avoid exciting proteins and particles simultaneously. The X-ray excitation studies are being optimized in a X-ray tube at the NanoDose laboratory in Ribeirão Preto, where the energy transfer measurements are being carried out.

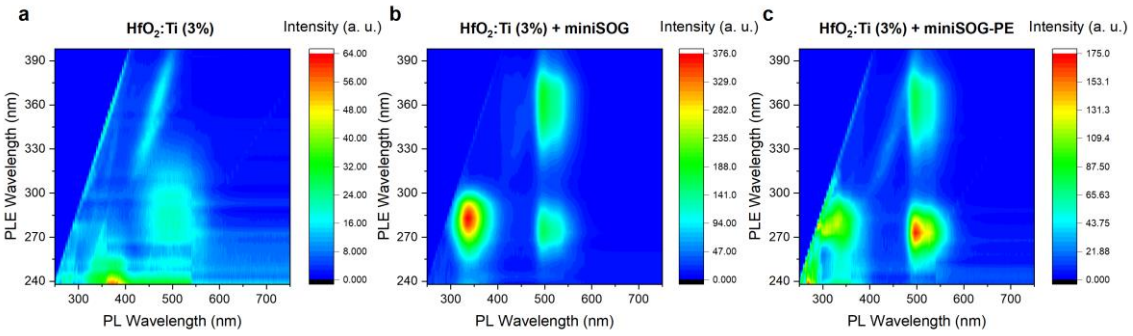

Figure 42: Contour plot of the photoluminescence intensities for the a) HfO2:Ti(3%),b) HfO2:Ti(3%)–miniSOG and c) HfO2:Ti(3%)–miniSOG-PE.

3.4 Conclusion

In this chapter, we reported new forms to functionalize blue luminescent nanoparticles with proteins to form a colloidal dispersion in PBS. The highest luminescence efficiency of HfO_2 nanoparticles doped with titanium (Ti) occured for 3% Ti concentration. The structural characterization confirmed the incorporation of Ti ions in the HfO_2 lattice without any formation of additional phases. The average crystal size was slightly larger for the Ti-doped nanoparticles than the undoped ones. Furthermore, the HfO_2:Ti(3%) nanoparticles were successfully dispersed in water, but when added to phosphate-buffered saline (PBS), they quickly underwent flocculation and precipitation due to pH changes and ionic strength. To address the stability issue in PBS, the nanoparticles were coated with citric acid (CA), which helped to maintain their ζ-potential constant across different pH conditions. The CA coating was found to bind to the nanoparticle surface via bridging bidentate bonding and stabilized the HfO_2:Ti(3%) in PBS. This stable dispersion was of significant importance as it mimicked the physiological environment, enabling potential biomedical applications.

The subsequent study aimed to bind the functional protein of interest, miniSOG, to the nanoparticles without additional chemical modifications. A sequence of 6 glutamates () was added to miniSOG's C-terminal to enhance the binding probability. During the separation step, we showed that the was essencial for a stably bounding of miniSOG to the HfO_2:Ti(3%). During photoluminescence assays, the energy transfer phenomenon between the nanoparticles

and proteins (miniSOG or miniSOG-PE) could not be easily recognized due to overlapping excitation regions in the UV range. To address this issue, an X-ray source was suggested to avoid simultaneous excitation of both the proteins and nanoparticles. Dynamic light scattering (DLS) data showed a considerable increase in nanoparticle size after complexation with the proteins, growing from the nanometric to the micrometric scale. The exact reason for this significant size increase requires further investigation. However, HfO_2:Ti(3%) coated with miniSOG-PE presented the same colloidal stability as for the particles coated with CA, indicating the success of the miniSOG modifications and its value as functionalization element.

Overall, the study demonstrated the successful doping of HfO_2 nanoparticles with Ti to enhance their luminescence efficiency, and the functionalization with citric acid facilitated stable dispersion in PBS. Moreover, the binding of miniSOG-PE to the nanoparticles showed promising potential for future biomedical applications involving energy transfer processes in a high-quality colloidal system.

Chapter 4 – General conclusions & Outcomes

Traditional photodynamic therapy (PDT) might suggest a photosensitizer (PS) activated outside the biological window to be less useful due to the limited penetration of ultraviolet-visible (UV-vis) light into human tissues. However, this perception has changed with advanced technological applications, such as the method proposed in this study. The ability to excite PS at different wavelengths expands the possibilities for finding new, compatible scintillators. A better understanding of each component's properties in the system can lead to designing more efficient nanoparticle-photosensitizer complexes.

Our goal was to develop new scintillating nanoparticles and facilitate their interaction with genetically encoded photosensitizers for X-ray-activated PDT. We intended to combine knowledge from molecular biology, physics, and nanotechnology to innovate in the field of photomedicine. Throughout the project, we used different synthesis methods to develop scintillating nanoparticles, and a variety of biophysical and biomolecular methos to protein characterization.

$LaF_3:Tb^{3+}$ nanoparticles were syhthezised by hot injection. We optimized the synthesis protocol and thermal treatment to enhance the particle size uniformity and scintillation intensity. The biophysical characterization of eGFP, KO, and KR aimed to study protein behavior under extreme conditions experienced *in vivo* during cancer therapies, such as hyperthermia, acidic environment, and ionizing radiation. The proteins proved to be stable and resilient. The high value of ScNP ζ-potential for $LaF_3:Tb^{3+}$ suggested electrostatic interactions in the nanoparticle−protein system. However, we showed that 6×His-tag likely acts as a linker for protein in Tb^{3+} doped nanoparticles, fostering stable complex formation by coordination of histidine with metal ions. We demonstrated energy transfer from ScNP to eGFP, KO, and KR. The KR−$LaF_3:Tb^{3+}$ toxicity upon irradiation was shown through *E. coli* death assays, suggesting reactive oxygen species generation.

For HfO_2:Ti nanoparticles, we used a solvothermal synthesis controlled by microwaves. This method was developed by Ph.D. Xavier Guichard at the Laboratory of Multifunctional Materials (ETH–Zurich) and yielded a fine colloidal dispersion of nanopartoicles in water. The HfO_2:Ti nanoparticles need to have their scintillation verified despite previous reports. Through adequate nanoparticle surface characterization, we understood the challenges in forming a colloidal system in PBS due to the shielding of steric and electrostatic interactions by salt presence. The information acquired allowed us to propose solutions. Functionalizing HfO_2:Ti

first with citric acid and then with genetically modified miniSOG with a 6×Glu-tag (Poly-E) emerged as a viable method to improve adherence to photosensitizers and dispersion stability of HfO_2:Ti particles, potentially increasing therapy effectiveness. The measured response of miniSOG to UV light was insightful and previously unreported. Tests with ionizing radiation showed minimal protein interaction with X-rays and no protein scintillation, as expeted. The same tests should be performed for the miniSOG–HfO_2:Ti complex. If needed, we could implement new synthesis steps for this nanoparticle to improve its scintillation.

In conclusion, our study successfully demonstrated the application of Scintillating Nanoparticles (ScNP) as energy transfer mediators from X-rays to genetically encoded photosensitizers, and the development of efficient protein functionalization methods for nanoparticles. The interaction between scintillating nanoparticles and proteins created a conjugated nanocompound with improved stability in biological media dispersion. This nanocompound's toxicity is radiation exposure-dependent, paving a novel avenue for using genetically encoded photosensitizers in X-ray PDT applications.

References

[1] Roy, A. Arundhati Roy: “Cresci com todas as meias-verdades e mentiras sobre Gandhi”. In *Cultura*, Aguilar, A., Ed.; El País: 2020.

[2] Mills, M. A.; Mills, M. P. The Science Before the War. In *The New Atlantis*, 2020; Vol. 61, pp 19-34.

[3] Parrish, J. A. The Scope of Photomedicine. In *The Science of Photomedicine*, Regan, J. D., Parrish, J. A. Eds.; Springer US, 1982; pp 3-17.

[4] Gusain, P.; Paliwal, R.; Jog, R. ANCIENT LIGHT THERAPIES: A BOON TO MEDICAL SCIENCE. In *Science and Culture*, 2018; pp 231-236.

[5] Daniell, M. D.; Hill, J. S. A History of Photodynamic Therapy. In *ANZ Journal of Surgery*, 1991; Vol. 61, pp 340-348.

[6] Podoleanu, A. G. Optical coherence tomography. *Journal of Microscopy* **2012**, *247* (3), 209-219. DOI: 10.1111/j.1365-2818.2012.03619.x.

[7] Egner, A.; Hell, S. W. Fluorescence microscopy with super-resolved optical sections. *Trends in Cell Biology* **2005**, *15* (4), 207-215. DOI: 10.1016/j.tcb.2005.02.003.

[8] Ishii, H.; Otomo, K.; Takahashi, T.; Yamaguchi, K.; Nemoto, T. Focusing new light on brain functions: multiphoton microscopy for deep and super-resolution imaging. *Neuroscience Research* **2022**, *179*, 24-30. DOI: 10.1016/j.neures.2021.11.011.

[9] Jeon, S.; Kim, J.; Lee, D.; Baik, J. W.; Kim, C. Review on practical photoacoustic microscopy. *Photoacoustics* **2019**, *15*. DOI: 10.1016/j.pacs.2019.100141.

[10] Zhenguo Wu and Liwei Jiang and Jianhua Zhao and Haishan, Z. In vivo micro-Raman spectroscopy of arbitrary-shaped region of interest under simultaneous reflectance confocal imaging guidance. In Photonics in Dermatology and Plastic Surgery 2023, 2023.

[11] Li, X. S.; Zhou, F. F.; Gu, Y. Photomedicine Lights Up the Future of Fighting Cancer. *Technology in Cancer Research & Treatment* **2019**, *18*. DOI: 10.1177/1533033819852971.

[12] Li, X. S.; Lovell, J. F.; Yoon, J.; Chen, X. Y. Clinical development and potential of photothermal and photodynamic therapies for cancer. *Nature Reviews Clinical Oncology* **2020**, *17* (11), 657-674. DOI: 10.1038/s41571-020-0410-2.

[13] Wan, M. T.; Lin, J. Y. Current evidence and applications of photodynamic therapy in dermatology. In *Clin Cosmet Investig Dermatol*, 2014; pp 145-163.

[14] Correia, J. H.; Rodrigues, J. A.; Pimenta, S.; Dong, T.; Yang, Z. Photodynamic Therapy Review: Principles, Photosensitizers, Applications, and Future Directions. In *Pharmaceutics*, 2021; Vol. 13, pp 1-16.

[15] Xiong, Y. Y.; Shepherd, S.; Tibbs, J.; Bacon, A.; Liu, W. N.; Akin, L. D.; Ayupova, T.; Bhaskar, S.; Cunningham, B. T. Photonic Crystal Enhanced Fluorescence: A Review on Design Strategies and Applications. *Micromachines* **2023**, *14* (3). DOI: 10.3390/mi14030668.

[16] Guimaraes, C. F.; Cruz-Moreira, D.; Caballero, D.; Pirraco, R. P.; Gasperini, L.; Kundu, S. C.; Reis, R. L. Shining a Light on Cancer-Photonics in Microfluidic Tumor Modeling and Biosensing. *Advanced Healthcare Materials* **2023**, *12* (14). DOI: 10.1002/adhm.202201442.

[17] Himel, M. H.; Sikder, B.; Ahmed, T.; Choudhury, S. M. Biomimicry in nanotechnology: a comprehensive review. *Nanoscale Advances* **2023**, *5* (3), 596-614. DOI: 10.1039/d2na00571a.

[18] Shimizu, K. Genetic engineered color silk: fabrication of a photonics material through a bioassisted technology. *Bioinspiration & Biomimetics* **2018**, *13* (4). DOI: 10.1088/1748-3190/aabbe9.

[19] Forestiere, C.; Pasquale, A. J.; Capretti, A.; Miano, G.; Tamburrino, A.; Lee, S. Y.; Reinhard, B. M.; Dal Negro, L. Genetically Engineered Plasmonic Nanoarrays. *Nano Letters* **2012**, *12* (4), 2037-2044. DOI: 10.1021/nl300140g.

[20] Chen, J. Q.; Ning, C. Y.; Zhou, Z. N.; Yu, P.; Zhu, Y.; Tan, G. X.; Mao, C. B. Nanomaterials as photothermal therapeutic agents. *Progress in Materials Science* **2019**, *99*, 1-26. DOI: 10.1016/j.pmatsci.2018.07.005.

[21] Alfarouk, K. O.; Stock, C. M.; Taylor, S.; Walsh, M.; Muddathir, A. K.; Verduzco, D.; Bashir, A. H. H.; Mohammed, O. Y.; Elhassan, G. O.; Harguindey, S.; et al. Resistance to cancer chemotherapy: failure in drug response from ADME to P-gp. *Cancer Cell International* **2015**, *15*. DOI: 10.1186/s12935-015-0221-1.

[22] Organization, W. H. Global Antimicrobial Resistance Surveillance System: Manual for Early Implementation. 2015.

[23] St Laurent, B.; Miller, B.; Burton, T. A.; Amaratunga, C.; Men, S.; Sovannaroth, S.; Fay, M. P.; Miotto, O.; Gwadz, R. W.; Anderson, J. M.; et al. Artemisinin-resistant Plasmodium falciparum clinical isolates can infect diverse mosquito vectors of Southeast Asia and Africa. *Nature Communications* **2015**, *6*. DOI: 10.1038/ncomms9614.

[24] Sabino, C. P.; Ribeiro, M. S.; Wainwright, M.; Dos Anjos, C.; Sellera, F. P.; Dropa, M.; Nunes, N. B.; Brancini, G. T. P.; Braga, G. U. L.; Arana-Chavez, V. E.; et al. The Biochemical Mechanisms of Antimicrobial Photodynamic Therapy(1). *Photochemistry and Photobiology* **2023**, *99* (2), 742-750. DOI: 10.1111/php.13685.

[25] Casas, A.; Di Venosa, G.; Hasan, T.; Batlle, A. Mechanisms of Resistance to Photodynamic Therapy. *Current Medicinal Chemistry* **2011**, *18* (16), 2486-2515. DOI: 10.2174/092986711795843272.

[26] Borgia, F.; Giuffrida, R.; Caradonna, E.; Vaccaro, M.; Guarneri, F.; Cannavo, S. P. Early and Late Onset Side Effects of Photodynamic Therapy. *Biomedicines* **2018**, *6* (1). DOI: 10.3390/biomedicines6010012.

[27] Ding, H. Y.; Yu, H. J.; Dong, Y.; Tian, R. H.; Huang, G.; Boothman, D. A.; Sumer, B. D.; Gao, J. M. Photoactivation switch from type II to type I reactions by electron-rich micelles for improved photodynamic therapy of cancer cells under hypoxia. *Journal of Controlled Release* **2011**, *156* (3), 276-280. DOI: 10.1016/j.jconrel.2011.08.019.

[28] Calixto, G. M. F.; Bernegossi, J.; de Freitas, L. M.; Fontana, C. R.; Chorilli, M. Nanotechnology-Based Drug Delivery Systems for Photodynamic Therapy of Cancer: A Review. *Molecules* **2016**, *21* (3). DOI: 10.3390/molecules21030342.

[29] Shcherbakova, D. M.; Shemetov, A. A.; Kaberniuk, A. A.; Verkhusha, V. V. Natural Photoreceptors as a Source of Fluorescent Proteins, Biosensors, and Optogenetic Tools. *Annual Review of Biochemistry, Vol 84* **2015**, *84*, 519-550. DOI: 10.1146/annurev-biochem-060614-034411.

[30] Seong, J.; Lin, M. Z. Optobiochemistry: Genetically Encoded Control of Protein Activity by Light. *Annual Review of Biochemistry, Vol 90, 2021* **2021**, *90*, 475-501. DOI: 10.1146/annurev-biochem-072420-112431.

[31] Hoff, W. D.; Xie, A.; Hellingwerr, K. J. Global conformational changes upon receptor stimulation in photoactive yellow protein. *Biophysical Journal* **1998**, *74* (2), A291-A291.

[32] Chudakov, D. M.; Matz, M. V.; Lukyanov, S.; Lukyanov, K. A. Fluorescent Proteins and Their Applications in Imaging Living Cells and Tissues. *Physiological Reviews* **2010**, *90* (3), 1103-1163. DOI: 10.1152/physrev.00038.2009.

[33] Nemet, I.; Ropelewski, P.; Imanishi, Y. Applications of phototransformable fluorescent proteins for tracking the dynamics of cellular components. *Photochemical & Photobiological Sciences* **2015**, *14* (10), 1787-1806. DOI: 10.1039/c5pp00174a.

[34] Bulina, M. E.; Lukyanov, K. A.; Britanova, O. V.; Onichtchouk, D.; Lukyanov, S.; Chudakov, D. M. Chromophore-assisted light inactivation (CALI) using the phototoxic fluorescent protein KillerRed. *Nature Protocols* **2006**, *1* (2), 947-953. DOI: 10.1038/nprot.2006.89.

[35] Jolle, C.; Deglon, N.; Pythoud, C.; Bouzier-Sore, A. K.; Pellerin, L. Development of Efficient AAV2/DJ-Based Viral Vectors to Selectively Downregulate the Expression of Neuronal or Astrocytic Target Proteins in the Rat Central Nervous System. *Frontiers in Molecular Neuroscience* **2019**, *12*. DOI: 10.3389/fnmol.2019.00201.

[36] Onukwufor, J. O.; Trewin, A. J.; Baran, T. M.; Almast, A.; Foster, T. H.; Wojtovich, A. P. Quantification of reactive oxygen species production by the red fluorescent proteins KillerRed, SuperNova and mCherry. *Free Radical Biology and Medicine* **2020**, *147*, 1-7. DOI: 10.1016/j.freeradbiomed.2019.12.008.

[37] Westberg, M.; Etzerodt, M.; Ogilby, P. R. Rational design of genetically encoded singlet oxygen photosensitizing proteins. *Current Opinion in Structural Biology* **2019**, *57*, 56-62. DOI: 10.1016/j.sbi.2019.01.025.

[38] Bulina, M. E.; Chudakov, D. M.; Britanova, O. V.; Yanushevich, Y. G.; Staroverov, D. B.; Chepurnykh, T. V.; Merzlyak, E. M.; Shkrob, M. A.; Lukyanov, S.; Lukyanov, K. A. A genetically encoded photosensitizer. In *Nat Biotechnol*, 2006a; Vol. 24, pp 95-99.

[39] Bulina, M. E.; Lukyanov, K. A.; Britanova, O. V.; Onichtchouk, D.; Lukyanov, S.; Chudakov, D. M. Chromophore-assisted light inactivation (CALI) using the phototoxic fluorescent protein KillerRed. In *Chromophore-assisted light inactivation (CALI) using the phototoxic fluorescent protein KillerRed*, 2006b; Vol. 1, pp 947-953.

[40] Viswanath, D.; Won, Y. Y. Combining Radiotherapy (RT) and Photodynamic Therapy (PDT): Clinical Studies on Conventional RT-PDT Approaches and Novel Nanoparticle-Based RT-PDT Approaches under Preclinical Evaluation. *Acs Biomaterials Science & Engineering* **2022**, *8* (9), 3644-3658. DOI: 10.1021/acsbiomaterials.2c00287.

[41] Kim, J.; Kim, H.; Chang, J. H. Endoscopic Probe for Ultrasound-Assisted Photodynamic Therapy of Deep-Lying Tissue. *Ieee Access* **2020**, *8*, 179745-179753. DOI: 10.1109/access.2020.3026372.

[42] Guidelli, I. N. F. a. M. M. I. a. L. H. S. N. a. M. C. M. a. E. J. Magnetic nanoparticles covered with polycyclic aromatic hydrocarbons as singlet oxygen carriers for combining photodynamic therapy and magnetic hyperthermia. *Journal of Photochemistry and Photobiology A: Chemistry* **2023**, *444*, 114902. DOI: https://doi.org/10.1016/j.jphotochem.2023.114902.

[43] Parrish, J. A. The Scope of Photomedicine. In *The Science of Photomedicine*, Springer Science & Business Media, 2012.

[44] Zou, X.; Yao, M.; Ma, L.; Hossu, M.; Han, X.; Juzenas, P. X-ray-Induced Nanoparticle-Based Photodynamic Therapy. In *Nanomedicine*, 2014; Vol. 9, p 2339−2351.

[45] Ma, L.; Zou, X.; Chen, W. A New X-ray Activated Nanoparticle. In *J. Biomed. Nanotechnol.*, 2014; Vol. 10, p 1501−1508.

[46] Hajagos, T. J.; Chao, L.; Cherepy, N. J.; Pei, Q. High-Z Sensitized Plastic Scintillators: A Review. In *Adv Mater*, Adv Mater. 2018 Jul;30(27); Vol. 30.

[47] Berry, R.; Getzin, M.; Gjesteby, L.; Wang, G. X-Optogenetics and U-Optogenetics: Feasibility and Possibilities. In *Photonics*, 2015; Vol. 2, pp 23-39.

[48] Ahmad, M.; Pratx, G.; Bazalova, M.; Xing, L. X-Ray Luminescence and X-Ray Fluorescence Computed Tomography: New Molecular Imaging Modalities. In *IEEE Access*, 2014; Vol. 2, pp 1051-1061.

[49] Sun, C.; Pratx, G.; Carpenter, C. M.; Liu, H. G.; Cheng, Z.; Gambhir, S. S.; Xing, L. Synthesis and Radioluminescence of PEGylated Eu3+-doped Nanophosphors as Bioimaging Probes. *Advanced Materials* **2011**, *23* (24), H195-H199. DOI: 10.1002/adma.201100919.

[50] Singh, P.; Kachhap, S.; Singh, S. K. Lanthanide-based hybrid nanostructures: Classification, synthesis, optical properties, and multifunctional applications. *Coordination Chemistry Reviews* **2022**, *472*. DOI: 10.1016/j.ccr.2022.214795.

[51] Bunzli, J. C. G. Lanthanide-doped nanoscintillators. *Light-Science & Applications* **2022**, *11* (1). DOI: 10.1038/s41377-022-00987-2.

[52] Nyk, M.; Kumar, R.; Ohulchanskyy, T. Y.; Bergey, E. J.; Prasad, P. N. High Contrast in Vitro and in Vivo Photoluminescence Bioimaging Using Near Infrared to Near Infrared Up-Conversion in TM3+ and Yb3+ Doped Fluoride Nanophosphors. *Nano Letters* **2008**, *8* (11), 3834-3838. DOI: 10.1021/nl802223f.

[53] Chen, G. Y.; Ohulchanskyy, T. Y.; Kumar, R.; Agren, H.; Prasad, P. N. Ultrasmall Monodisperse NaYF4:Yb3+/Tm3+ Nanocrystals with Enhanced Near-Infrared to Near-Infrared Upconversion Photoluminescence. *Acs Nano* **2010**, *4* (6), 3163-3168. DOI: 10.1021/nn100457j.

[54] Zhou, J.; Sun, Y.; Du, X. X.; Xiong, L. Q.; Hu, H.; Li, F. Y. Dual-modality in vivo imaging using rare-earth nanocrystals with near-infrared to near-infrared (NIR-to-NIR) upconversion luminescence and magnetic resonance properties. *Biomaterials* **2010**, *31* (12), 3287-3295. DOI: 10.1016/j.biomaterials.2010.01.040.

[55] Carpenter, C. M.; Sun, C.; Pratx, G.; Rao, R.; Xing, L. Hybrid x-ray/optical luminescence imaging: Characterization of experimental conditions. *Medical Physics* **2010**, *37* (8), 4011-4018. DOI: 10.1118/1.3457332.

[56] Pratx, G.; Carpenter, C. M.; Sun, C.; Rao, R. P.; Xing, L. Tomographic molecular imaging of x-ray-excitable nanoparticles. *Optics Letters* **2010**, *35* (20), 3345-3347. DOI: 10.1364/ol.35.003345.

[57] Pratx, G.; Carpenter, C. M.; Sun, C.; Xing, L. X-Ray Luminescence Computed Tomography via Selective Excitation: A Feasibility Study. *Ieee Transactions on Medical Imaging* **2010**, *29* (12), 1992-1999. DOI: 10.1109/tmi.2010.2055883.

[58] Byrne, J. D.; Betancourt, T.; Brannon-Peppas, L. Active targeting schemes for nanoparticle systems in cancer therapeutics. *Advanced Drug Delivery Reviews* **2008**, *60* (15), 1615-1626. DOI: 10.1016/j.addr.2008.08.005.

[59] Colby, A. H.; Kirsch, J.; Patwa, A. N.; Liu, R.; Hollister, B.; McCulloch, W.; Burdette, J. E.; Pearce, C. J.; Oberliels, N. H.; Colson, Y. L.; et al. Radiolabeled Biodistribution of Expansile Nanoparticles: Intraperitoneal Administration Results in Tumor Specific Accumulation. *Acs Nano* **2023**. DOI: 10.1021/acsnano.2c08451.

[60] Karnkaew, A.; Chen, F.; Zhan, Y. H.; Majewski, R. L.; Cai, W. B. Scintillating Nanoparticles as Energy Mediators for Enhanced Photodynamic Therapy. *Acs Nano* **2016**, *10* (4), 3918-3935. DOI: 10.1021/acsnano.6b01401.

[61] Bizarri, G. Scintillation mechanisms of inorganic materials: From crystal characteristics to scintillation properties. *Journal of Crystal Growth* **2010**, *312* (8), 1213-1215. DOI: 10.1016/j.jcrysgro.2009.12.063.

[62] Kamkaew, A.; Chen, F.; Zhan, Y.; Majewski, R. L.; Cai, W. Scintillating Nanoparticles as Energy Mediators for Enhanced. In *ACSnano*, 2016; Vol. 10, p 3918−3935.

[63] Lakowicz, J. *Principles of Fluorescence Spectroscopy*; Springer, 2013.

[64] Villa, I.; Villa, C.; Cramoanzano, R.; Secchi, V.; Tawfilas, M.; Trombetta, E.; Porretti, L.; Brambilla, A.; Campione, M.; Torrente, Y.; et al. Functionalized Scintillating Nanotubes for Simultaneous Radio- and Photodynamic Therapy of Cancer. In *ACS Appl. Mater. Interfaces*, 2021; Vol. 13, p ACS Appl. Mater. Interfaces.

[65] Micheletto, M. C.; Guidelli, E. J.; Costa, A. J. Interaction of Genetically Encoded Photosensitizers with Scintillating Nanoparticles for X-ray Activated Photodynamic Therapy. *Acs Applied Materials & Interfaces* **2021**, *13* (2), 2289-2302. DOI: 10.1021/acsami.0c19041.

[66] Gorbachev, D. A.; Staroverov, D. B.; Lukyanov, K. A.; Sarkisyan, K. S. Genetically Encoded Red Photosensitizers with Enhanced Phototoxicity. *International Journal of Molecular Sciences* **2020**, *21* (22). DOI: 10.3390/ijms21228800.

[67] Williams, D. C.; El Bejjani, R.; Ramirez, P. M.; Coakley, S.; Kim, S. A.; Lee, H.; Wen, Q.; Samuel, A.; Lu, H.; Hilliard, M. A.; et al. Rapid and Permanent Neuronal Inactivation In Vivo via Subcellular Generation of Reactive Oxygen with the Use of KillerRed. *Cell Reports* **2013**, *5* (2), 553-563. DOI: 10.1016/j.celrep.2013.09.023.

[68] Trauner, D.; Morstein, J. Fixing a Photosensitizer Unlocks and Localizes Its Lethality. *Acs Central Science* **2019**, *5* (10), 1636-1638. DOI: 10.1021/acscentsci.9b00887.

[69] Makhijani, K.; To, T. L.; Ruiz-Gonzalez, R.; Lafaye, C.; Royant, A.; Shu, X. K. Precision Optogenetic Tool for Selective Single- and Multiple-Cell Ablation in a Live Animal Model System. *Cell Chemical Biology* **2017**, *24* (1), 110-119. DOI: 10.1016/j.chembiol.2016.12.010.

[70] Wojtovich, A. P.; Foster, T. H. Optogenetic control of ROS production. *Redox Biology* **2014**, *2*, 368-376. DOI: 10.1016/j.redox.2014.01.019.

[71] Tuijtel, M. W.; Koster, A. J.; Faas, F. G. A.; Sharp, T. H. Correlated Cryo Super-Resolution Light and Cryo-Electron Microscopy on Mammalian Cells Expressing the Fluorescent Protein rsEGFP2. *Small Methods* **2019**, *3* (12). DOI: 10.1002/smtd.201900425.

[72] Hilgers, F.; Bitzenhofer, N. L.; Ackermann, Y.; Burmeister, A.; Grunberger, A.; Jaeger, K. E.; Drepper, T. Genetically Encoded Photosensitizers as Light-Triggered Antimicrobial Agents. *International Journal of Molecular Sciences* **2019**, *20* (18). DOI: 10.3390/ijms20184608.

[73] Ryumina, A. P.; Serebrovskaya, E. O.; Shirmanova, M. V.; Snopova, L. B.; Kuznetsova, M. M.; Turchin, I. V.; Ignatova, N. I.; Klementieva, N. V.; Fradkov, A. F.; Shakhov, B. E.; et al. Flavoprotein miniSOG as a genetically encoded photosensitizer for cancer cells. *Biochimica Et Biophysica Acta-General Subjects* **2013**, *1830* (11), 5059-5067. DOI: 10.1016/j.bbagen.2013.07.015.

[74] Shimomura, O.; Johnson, F. H.; Saiga, Y. EXTRACTION, PURIFICATION AND PROPERTIES OF AEQUORIN, A BIOLUMINESCENT PROTEIN FROM LUMINOUS HYDROMEDUSAN, AEQUOREA. *Journal of Cellular and Comparative Physiology* **1962**, *59* (3), 223-&. DOI: 10.1002/jcp.1030590302.

[75] Chalfie, M.; Tu, Y.; Euskirchen, G.; Ward, W. W.; Prasher, D. C. GREEN FLUORESCENT PROTEIN AS A MARKER FOR GENE-EXPRESSION. *Science* **1994**, *263* (5148), 802-805. DOI: 10.1126/science.8303295.

[76] Tsien, R. Y. The Green Fluorescent Protein. *Annual Review of Biochemistry* **1998**, *67* (1), 509-544. DOI: 10.1146/annurev.biochem.67.1.509 , note = PMID: 9759496.

[77] Lippincott-Schwartz, J.; Patterson, G. H. Development and use of fluorescent protein markers in living cells. *Science* **2003**, *300* (5616), 87-91. DOI: 10.1126/science.1082520.

[78] Heim, R.; Prasher, D. C.; Tsien, R. Y. WAVELENGTH MUTATIONS AND POSTTRANSLATIONAL AUTOXIDATION OF GREEN FLUORESCENT PROTEIN. *Proceedings of the National Academy of Sciences of the United States of America* **1994**, *91* (26), 12501-12504. DOI: 10.1073/pnas.91.26.12501.

[79] Yang, T. T.; Cheng, L. Z.; Kain, S. R. Optimized codon usage and chromophore mutations provide enhanced sensitivity with the green fluorescent protein. *Nucleic Acids Research* **1996**, *24* (22), 4592-4593. DOI: 10.1093/nar/24.22.4592.

[80] Cormack, B. P.; Valdivia, R. H.; Falkow, S. FACS-optimized mutants of the green fluorescent protein (GFP). *Gene* **1996**, *173* (1), 33-38. DOI: 10.1016/0378-1119(95)00685-0.

[81] Arpino, J. A. J.; Rizkallah, P. J.; Jones, D. D. Crystal Structure of Enhanced Green Fluorescent Protein to 1.35 angstrom Resolution Reveals Alternative Conformations for Glu222. *Plos One* **2012**, *7* (10). DOI: 10.1371/journal.pone.0047132.

[82] Lukyanov, K. A.; Serebrovskaya, E. O.; Lukyanov, S.; Chudakov, D. M. Fluorescent proteins as light-inducible photochemical partners. *Photochemical & Photobiological Sciences* **2010**, *9* (10), 1301-1306. DOI: 10.1039/c0pp00114g.

[83] Pletneva, N. V.; Pletnev, V. Z.; Sarkisyan, K. S.; Gorbachev, D. A.; Egorov, E. S.; Mishin, A. S.; Lukyanov, K. A.; Dauter, Z.; Pletnev, S. Crystal Structure of Phototoxic Orange Fluorescent Proteins with a Tryptophan-Based Chromophore. *Plos One* **2015**, *10* (12). DOI: 10.1371/journal.pone.0145740.

[84] Carpentier, P.; Violot, S.; Blanchoin, L.; Bourgeois, D. Structural basis for the phototoxicity of the fluorescent protein KillerRed. *Febs Letters* **2009**, *583* (17), 2839-2842. DOI: 10.1016/j.febslet.2009.07.041.

[85] Vegh, R. B.; Solntsev, K. M.; Kuimova, M. K.; Cho, S.; Liang, Y.; Loo, B. L. W.; Tolbert, L. M.; Bommarius, A. S. Reactive oxygen species in photochemistry of the red fluorescent protein "Killer Red". *Chemical Communications* **2011**, *47* (17), 4887-4889. DOI: 10.1039/c0cc05713d.

[86] Reid, B. G.; Flynn, G. C. Chromophore formation in green fluorescent protein. *Biochemistry* **1997**, *36* (22), 6786-6791. DOI: 10.1021/bi970281w.

[87] Jiang, H. N.; Li, Y.; Cui, Z. J. Photodynamic Physiology-Photonanomanipulations in Cellular Physiology with Protein Photosensitizers. *Frontiers in Physiology* **2017**, *8*. DOI: 10.3389/fphys.2017.00191.

[88] Tang, Y. G.; Hu, J.; Elmenoufy, A. H.; Yang, X. L. Highly Efficient FRET System Capable of Deep Photodynamic Therapy Established on X-ray Excited Mesoporous LaF3:Tb Scintillating Nanoparticles. *Acs Applied Materials & Interfaces* **2015**, *7* (22), 12261-12269. DOI: 10.1021/acsami.5b03067.

[89] Gipson, K.; Kucera, C.; Stadther, D.; Stevens, K.; Ballato, J.; Brown, P. The Influence of Synthesis Parameters on Particle Size and Photoluminescence Characteristics of Ligand Capped Tb3+:LaF3. *Polymers* **2011**, *3* (4), 2039-2052. DOI: 10.3390/polym3042039.

[90] Carnall, W. T.; Fields, P. R.; Rajnak, K. ELECTRONIC ENERGY LEVELS OF TRIVALENT LANTHANIDE AQUO IONS .3. TB3+. *Journal of Chemical Physics* **1968**, *49* (10), 4447-&. DOI: 10.1063/1.1669895.

[91] Tan, M. L.; del Rosal, B.; Zhang, Y. Q.; Rodriguez, E. M.; Hu, J.; Zhou, Z. G.; Fan, R. W.; Ortgies, D. H.; Fernandez, N.; Chaves-Coira, I.; et al. Rare-earth-doped fluoride nanoparticles with engineered long luminescence lifetime for time-gated in vivo optical imaging in the second biological window. *Nanoscale* **2018**, *10* (37), 17771-17780. DOI: 10.1039/c8nr02382d.

[92] Neufeld, M. J.; Lutzke, A.; Pratx, G.; Sun, C. High-Z Metal-Organic Frameworks for X-ray Radiation-Based Cancer Theranostics. *Chemistry-a European Journal* **2021**, *27* (10), 3229-3237. DOI: 10.1002/chem.202003523.

[93] Souris, J. S.; Leoni, L.; Zhang, H. J.; Pan, A. R.; Tanios, E.; Tsai, H. M.; Balyasnikova, I. V.; Bissonnette, M.; Chen, C. T. X-ray Activated Nanoplatforms for Deep Tissue Photodynamic Therapy. *Nanomaterials* **2023**, *13* (4). DOI: 10.3390/nano13040673.

[94] He, L. R.; Yu, X. J.; Li, W. W. Recent Progress and Trends in X-ray-Induced Photodynamic Therapy with Low Radiation Doses. *Acs Nano* **2022**, *16* (12), 19691-19721. DOI: 10.1021/acsnano.2c07286.

[95] *Imagej.net. 2020. Imagej. [online] Available at: https://imagej. net/Welcome (accessed 1 April 2020].* (accessed.

[96] Expasy.org. (2020). Ex*PASy: SIB Bioinformatics Resource Portal - Home.* [online] Available at: https://www.expasy.org/ [Accessed 1 Feb. 2020].

[97] Greenfield, N. J. Using circular dichroism spectra to estimate protein secondary structure. *Nature Protocols* **2006**, *1* (6), 2876-2890. DOI: 10.1038/nprot.2006.202.

[98] Macdonald, P. J.; Chen, Y.; Mueller, J. D. Chromophore maturation and fluorescence fluctuation spectroscopy of fluorescent proteins in a cell-free expression system. *Analytical Biochemistry* **2012**, *421* (1), 291-298. DOI: 10.1016/j.ab.2011.10.040.

[99] Vegh, R. B.; Bravaya, K. B.; Bloch, D. A.; Bommarius, A. S.; Tolbert, L. M.; Verkhovsky, M.; Krylov, A. I.; Solntsev, K. M. Chromophore Photoreduction in Red Fluorescent Proteins Is Responsible for Bleaching and Phototoxicity. *Journal of Physical Chemistry B* **2014**, *118* (17), 4527-4534. DOI: 10.1021/jp500919a.

[100] Liu, J. X.; Wang, F.; Qin, Y.; Feng, X. L. Advances in the Genetically Engineered KillerRed for Photodynamic Therapy Applications. *International Journal of Molecular Sciences* **2021**, *22* (18). DOI: 10.3390/ijms221810130.

[101] Trewin, A. J.; Berry, B. J.; Wei, A. Y.; Bahr, L. L.; Foster, T. H.; Wojtovich, A. P. Light-induced oxidant production by fluorescent proteins. In *Free Radical Biology and Medicine*, 2018; Vol. 128, pp 157-164.

[102] Porter, P. G. B. a. G. Triplet State Quantum Yields for Some Aromatic Hydrocarbons and Xanthene Dyes in Dilute Solution , urldate = 2023-07-06. *Proceedings of the Royal Society of London. Series A, Mathematical and Physical Sciences* **1967**, *299* (1458), 348--353.

[103] Evrogen.com. (2020). Ev*rogen KillerRed: Detailed description.* [online] Available at: http://evrogen.com/products/KillerRed/KillerRed_Detailed_description.shtml [Accessed 17 Feb. 2020].

[104] Evrogen.com. (2020). Ev*rogen KillerOrange: Detailed description.* [online] Available at: http://evrogen.com/products/KillerOrange/KillerOrange_Detailed_description.shtml [Accessed 17 Feb. 2020].

[105] Sarkisyan, K. S.; Zlobovskaya, O. A.; Gorbachev, D. A.; Bozhanova, N. G.; Sharonov, G. V.; Staroverov, D. B.; Egorov, E. S.; Ryabova, A. V.; Solntsev, K. M.; Mishin, A. S.; et al. KillerOrange, a Genetically Encoded Photosensitizer Activated by Blue and Green Light. *Plos One* **2015**, *10* (12). DOI: 10.1371/journal.pone.0145287.

[106] Kim, M.; Kim, G.; Kim, D.; Yoo, J.; Kim, D. K.; Kim, H. Numerical Study on Effective Conditions for the Induction of Apoptotic Temperatures for Various Tumor Aspect Ratios Using a Single Continuous-Wave Laser in Photothermal Therapy Using Gold Nanorods. *Cancers* **2019**, *11* (6). DOI: 10.3390/cancers11060764.

[107] Li, M.; Mukerji, R.; Leong, K. Smart Theranostic Nanosystems. S*mart Pharmaceutical Nanocarriers*: 2016; pp 523-549.

[108] Tannock, I. F.; Rotin, D. ACID PH IN TUMORS AND ITS POTENTIAL FOR THERAPEUTIC EXPLOITATION. *Cancer Research* **1989**, *49* (16), 4373-4384.

[109] Grigorenko, B. L.; Khrenova, M. G.; Kulakova, A. M.; Nemukhin, A. V. Intermediates of the Autocatalytic Reaction of the Formation of a Chromophore in a Green Fluorescent Protein. *Russian Journal of Physical Chemistry B* **2020**, *14* (3), 457-461. DOI: 10.1134/s1990793120030161.

[110] Okuno, E.; Yoshimura, E. F*ísica das radiações*. Oficina de Textos: São Paulo, 2010.

[111] Reisz, J. A.; Bansal, N.; Qian, J.; Zhao, W. L.; Furdui, C. M. Effects of Ionizing Radiation on Biological Molecules-Mechanisms of Damage and Emerging Methods of Detection. *Antioxidants & Redox Signaling* **2014**, *21* (2), 260-292. DOI: 10.1089/ars.2013.5489.

[112] Townley, H. E.; Kim, J.; Dobson, P. J. In vivo demonstration of enhanced radiotherapy using rare earth doped titania nanoparticles. *Nanoscale* **2012**, *4* (16), 5043-5050. DOI: 10.1039/c2nr30769c.

[113] Liu, Y. F.; Chen, W.; Wang, S. P.; Joly, A. G.; Westcott, S.; Woo, B. K. X-ray luminescence of LaF3 : Tb3+ and LaF3 : Ce3+, Tb3+ water-soluble nanoparticles. *Journal of Applied Physics* **2008**, *103* (6). DOI: 10.1063/1.2890148.

[114] Kai, C.; Chao, G.; Bo, P.; Wei, W. The Influence of SiO₂ Shell on Fluorescent Properties of LaF₃:Nd³⁺ /SiO₂ Core/Shell Nanoparticles. *Journal of Nanomaterials* **2010**, *2010*, 238792. DOI: 10.1155/2010/238792.

[115] Arsalani, S.; Guidelli, E. J.; Araujo, J.; Bruno, A. C.; Baffa, O. Green Synthesis and Surface Modification of Iron Oxide Nanoparticles with Enhanced Magnetization Using Natural Rubber Latex. *Acs Sustainable Chemistry & Engineering* **2018**, *6* (11), 13756-13765. DOI: 10.1021/acssuschemeng.8b01689.

[116] Zhang, L. S.; Li, W.; Hu, X. H.; Peng, Y. L.; Hu, J. Q.; Kuang, X. Y.; Song, L. L.; Chen, Z. G. Facile one-pot sonochemical synthesis of hydrophilic ultrasmall LaF3:Ce,Tb nanoparticles with green luminescence. *Progress in Natural Science-Materials International* **2012**, *22* (5), 488-492. DOI: 10.1016/j.pnsc.2012.07.007.

[117] Gao, D. L.; Zheng, H. R.; Zhang, X. Y.; Gao, W.; Tian, Y.; Li, J. A.; Cui, M. Luminescence enhancement and quenching by codopant ions in lanthanide doped fluoride nanocrystals. *Nanotechnology* **2011**, *22* (17). DOI: 10.1088/0957-4484/22/17/175702.

[118] Luo, Y.; Xia, Z. G.; Liao, L. B. Phase formation evolution and upconversion luminescence properties of LaOF:Yb3+/Er3+ prepared via a two-step reaction. *Ceramics International* **2012**, *38* (8), 6907-6910. DOI: 10.1016/j.ceramint.2012.05.005.

[119] Hoo, C. M.; Starostin, N.; West, P.; Mecartney, M. L. A comparison of atomic force microscopy (AFM) and dynamic light scattering (DLS) methods to characterize nanoparticle size distributions. *Journal of Nanoparticle Research* **2008**, *10*, 89-96. DOI: 10.1007/s11051-008-9435-7.

[120] Prokop, A.; Kozlov, E.; Carlesso, G.; Davidson, J. M. Hydrogel-based colloidal polymeric system for protein and drug delivery: Physical and chemical characterization, permeability control and applications. *Filled Elastomers Drug Delivery Systems* **2002**, *160*, 119-173.

[121] Kong, D. Y.; Wang, Z. L.; Lin, C. K.; Quan, Z. W.; Li, Y. Y.; Li, C. X.; Lin, J. Biofunctionalization of CeF3 : Tb3+ nanoparticles. *Nanotechnology* **2007**, *18* (7). DOI: 10.1088/0957-4484/18/7/075601.

[122] Dejneka, M.; Samson, B. Rare-earth-doped fibers for telecommunications applications. *Mrs Bulletin* **1999**, *24* (9), 39-45. DOI: 10.1557/s0883769400053057.

[123] Lochhead, M. J.; Bray, K. L. RARE-EARTH CLUSTERING AND ALUMINUM CODOPING IN SOL-GEL SILICA - INVESTIGATION USING EUROPIUM(III) FLUORESCENCE SPECTROSCOPY. *Chemistry of Materials* **1995**, *7* (3), 572-577. DOI: 10.1021/cm00051a019.

[124] Guidelli, E. J.; Ramos, A. P.; Zaniquelli, M. E. D.; Nicolucci, P.; Baffa, O. Synthesis and characterization of silver/alanine nanocomposites for radiation detection in medical applications: the influence of particle size on the detection properties. *Nanoscale* **2012**, *4* (9), 2884-2893. DOI: 10.1039/c2nr30090g.

[125] Balazs, A. C.; Emrick, T.; Russell, T. P. Nanoparticle polymer composites: Where two small worlds meet. *Science* **2006**, *314* (5802), 1107-1110. DOI: 10.1126/science.1130557.

[126] Wasserberg, D.; Cabanas-Danes, J.; Prangsma, J.; O'Mahony, S.; Cazade, P. A.; Tromp, E.; Blum, C.; Thompson, D.; Huskens, J.; Subramaniam, V.; et al. Controlling Protein Surface Orientation by Strategic Placement of Oligo-Histidine Tags. *Acs Nano* **2017**, *11* (9), 9068-9083. DOI: 10.1021/acsnano.7b03717.

[127] Yuzhakova, D. V.; Shirmanova, M. V.; Klimenko, V. V.; Lukina, M. M.; Gavrina, A. I.; Komarova, A. D.; Gorbachev, D. A.; Sapogova, N. V.; Lukyanov, K. A.; Kamensky, V. A. PDT with genetically encoded photosensitizer miniSOG on a tumor spheroid model: A comparative study of continuous-wave and pulsed irradiation. *Biochimica Et Biophysica Acta-General Subjects* **2021**, *1865* (12). DOI: 10.1016/j.bbagen.2021.129978.

[128] Proshkina, G. M.; Shramova, E. I.; Shilova, O. N.; Ryabova, A. V.; Deyev, S. M. Phototoxicity of flavoprotein miniSOG induced by bioluminescence resonance energy transfer in genetically encoded system NanoLuc-miniSOG is comparable with its LED-excited phototoxicity. *Journal of Photochemistry and Photobiology B-Biology* **2018**, *188*, 107-115. DOI: 10.1016/j.jphotobiol.2018.09.006.

[129] Ruiz-Gonzalez, R.; White, J. H.; Cortajarena, A. L.; Agut, M.; Nonell, S.; Flors, C. Fluorescent proteins as singlet oxygen photosensitizers: mechanistic studies in photodynamic inactivation of bacteria. In *Conference on Reporters, Markers, Dyes, Nanoparticles, and Molecular Probes for Biomedical Applications V*, San Francisco, CA, Feb 04-06, 2013; 2013; Vol. 8596. DOI: 10.1117/12.2000695.

[130] Shu, X. K.; Lev-Ram, V.; Deerinck, T. J.; Qi, Y. C.; Ramko, E. B.; Davidson, M. W.; Jin, Y. S.; Ellisman, M. H.; Tsien, R. Y. A Genetically Encoded Tag for Correlated Light and Electron Microscopy of Intact Cells, Tissues, and Organisms. *Plos Biology* **2011**, *9* (4). DOI: 10.1371/journal.pbio.1001041.

[131] Herrou, J.; Crosson, S. Function, structure and mechanism of bacterial photosensory LOV proteins. *Nature Reviews Microbiology* **2011**, *9* (10), 713-723. DOI: 10.1038/nrmicro2622.

[132] Salomon, M.; Christie, J. M.; Knieb, E.; Lempert, U.; Briggs, W. R. Photochemical and mutational analysis of the FMN-binding domains of the plant blue light receptor, phototropin. *Biochemistry* **2000**, *39* (31), 9401-9410. DOI: 10.1021/bi000585+.

[133] Torra, J.; Lafaye, C.; Signor, L.; Aumonier, S.; Flors, C.; Shu, X. K.; Nonell, S.; Gotthard, G.; Royant, A. Tailing miniSOG: structural bases of the complex photophysics of a flavin-binding singlet oxygen photosensitizing protein. *Scientific Reports* **2019**, *9*. DOI: 10.1038/s41598-019-38955-3.

[134] Crosson, S.; Rajagopal, S.; Moffat, K. The LOV domain family: Photoresponsive signaling modules coupled to diverse output domains. *Biochemistry* **2003**, *42* (1), 2-10. DOI: 10.1021/bi026978l.

[135] Swartz, T. E.; Corchnoy, S. B.; Christie, J. M.; Lewis, J. W.; Szundi, I.; Briggs, W. R.; Bogomolni, R. A. The photocycle of a flavin-binding domain of the blue light photoreceptor phototropin. *Journal of Biological Chemistry* **2001**, *276* (39), 36493-36500. DOI: 10.1074/jbc.M103114200.

[136] Jones, M. A.; Feeney, K. A.; Kelly, S. M.; Christie, J. M. Mutational analysis of phototropin 1 provides insights into the mechanism underlying LOV2 signal transmission. *Journal of Biological Chemistry* **2007**, *282* (9), 6405-6414. DOI: 10.1074/jbc.M605969200.

[137] Endres, S.; Wingen, M.; Torra, J.; Ruiz-Gonzalez, R.; Polen, T.; Bosio, G.; Bitzenhofer, N. L.; Hilgers, F.; Gensch, T.; Nonell, S.; et al. An optogenetic toolbox of LOV-based photosensitizers for light-driven killing of bacteria. *Scientific Reports* **2018**, *8*. DOI: 10.1038/s41598-018-33291-4.

[138] Baier, J.; Maisch, T.; Maier, M.; Engel, E.; Landthaler, M.; Baumler, W. Singlet oxygen generation by UVA light exposure of endogenous photosensitizers. *Biophysical Journal* **2006**, *91* (4), 1452-1459. DOI: 10.1529/biophysj.106.082388.

[139] Massey, V. The chemical and biological versatility of riboflavin. *Biochemical Society Transactions* **2000**, *28*, 283-296. DOI: 10.1042/0300-5127:0280283.

[140] Abrahamse, H.; Hamblin, M. R. New photosensitizers for photodynamic therapy. *Biochemical Journal* **2016**, *473*, 347-364. DOI: 10.1042/bj20150942.

[141] Zhang, P. Y.; Huang, H. Y.; Banerjee, S.; Clarkson, G. J.; Ge, C.; Imberti, C.; Sadler, P. J. Nucleus-Targeted Organoiridium-Albumin Conjugate for Photodynamic Cancer Therapy. *Angewandte Chemie-International Edition* **2019**, *58* (8), 2350-2354. DOI: 10.1002/anie.201813002.

[142] Avci, P.; Gupta, A.; Sadasivam, M.; Vecchio, D.; Pam, Z.; Pam, N.; Hamblin, M. R. Low-Level Laser (Light) Therapy (LLLT) in Skin: Stimulating, Healing, Restoring. *Seminars in Cutaneous Medicine and Surgery* **2013**, *32* (1), 41-52.

[143] Kim, M. M.; Darafsheh, A. Light Sources and Dosimetry Techniques for Photodynamic Therapy. *Photochemistry and Photobiology* **2020**, *96* (2), 280-294. DOI: 10.1111/php.13219.

[144] National Lybrary of Medicine. *National Center for Biotechnology Information*. https://pubmed.ncbi.nlm.nih.gov/.

[145] Villa, I.; Villa, C.; Monguzzi, A.; Babin, V.; Tervoort, E.; Nikl, M.; Niederberger, M.; Yvan, T.; Vedda, A.; Lauria, A. Demonstration of cellular imaging by using luminescent and anti-cytotoxic europium-doped hafnia nanocrystals. *Nanoscale* **2018**, *10* (17), 7933-7940. DOI: 10.1039/c8nr00724a.

[146] Villa, I.; Lauria, A.; Moretti, F.; Fasoli, M.; Dujardin, C.; Niederberger, M.; Vedda, A. Radio-luminescence spectral features and fast emission in hafnium dioxide nanocrystals. *Physical Chemistry Chemical Physics* **2018**, *20* (23), 15907-15915. DOI: 10.1039/c8cp01230j.

[147] Villa, I.; Moretti, F.; Fasoli, M.; Rossi, A.; Hattendorf, B.; Dujardin, C.; Niederberger, M.; Vedda, A.; Lauria, A. The Bright X-Ray Stimulated Luminescence of HfO2 Nanocrystals Activated by Ti Ions. *Advanced Optical Materials* **2020**, *8* (1). DOI: 10.1002/adom.201901348.

[148] Guichard, X. H.; Bernasconi, F.; Lauria, A. Charge Compensation in Europium-Doped Hafnia Nanoparticles: Solvothermal Synthesis and Colloidal Dispersion. *Crystals* **2021**, *11* (9), 1042.

[149] Villa, I.; Vedda, A.; Fasoli, M.; Lorenzi, R.; Kranzlin, N.; Rechberger, F.; Ilari, G.; Primc, D.; Hattendorf, B.; Heiligtag, F. J.; et al. Size-Dependent Luminescence in Hfo(2) Nanocrystals: Toward White Emission from Intrinsic Surface Defects. *Chemistry of Materials* **2016**, *28* (10), 3245-3253. DOI: 10.1021/acs.chemmater.5b03811.

[150] Olliges-Stadler, I.; Rossell, M. D.; Niederberger, M. Co-operative Formation of Monolithic Tungsten Oxide-Polybenzylene Hybrids via Polymerization of Benzyl Alcohol and Study of the Catalytic Activity of the Tungsten Oxide Nanoparticles. *Small* **2010**, *6* (8), 960-966. DOI: 10.1002/smll.200902289.

[151] Braendle, A.; Perevedentsev, A.; Cheetham, N. J.; Stavrinou, P. N.; Schachner, J. A.; Mosch-Zanetti, N. C.; Niederberger, M.; Caseri, W. R. Homoconjugation in Poly(Phenylene Methylene) s: A Case Study of Non-pi-Conjugated Polymers with Unexpected Fluorescent Properties. *Journal of Polymer Science Part B-Polymer Physics* **2017**, *55* (9), 707-720. DOI: 10.1002/polb.24305.

[152] Frantz, C.; Lauria, A.; Manzano, C. V.; Guerra-Nunez, C.; Niederberger, M.; Storrer, C.; Michler, J.; Philippe, L. Nonaqueous Sol-Gel Synthesis of Anatase Nanoparticles and Their Electrophoretic Deposition in Porous Alumina. *Langmuir* **2017**, *33* (43), 12404-12418. DOI: 10.1021/acs.langmuir.7b02103.

[153] Shinohara, S.; Eom, N.; Teh, E. J.; Tamada, K.; Parsons, D.; Craig, V. S. J. The Role of Citric Acid in the Stabilization of Nanoparticles and Colloidal Particles in the Environment: Measurement of Surface Forces between Hafnium Oxide Surfaces in the Presence of Citric Acid. *Langmuir* **2018**, *34* (8), 2595-2605. DOI: 10.1021/acs.langmuir.7b03116.

[154] da Silva, G. B.; Marciello, M.; Morales, M. D.; Serna, C. J.; Vargas, M. D.; Ronconi, C. M.; Costo, R. Studies of the Colloidal Properties of Superparamagnetic Iron Oxide Nanoparticles Functionalized with Platinum Complexes in Aqueous and PBS Buffer Media. *Journal of the Brazilian Chemical Society* **2017**, *28* (5), 731-739. DOI: 10.21577/0103-5053.20160221.

[155] Mudunkotuwa, I. A.; Grassian, V. H. Citric Acid Adsorption on TiO2 Nanoparticles in Aqueous Suspensions at Acidic and Circumneutral pH: Surface Coverage, Surface Speciation, and Its Impact on Nanoparticle-Nanoparticle Interactions. *Journal of the American Chemical Society* **2010**, *132* (42), 14986-14994. DOI: 10.1021/ja106091q.

[156] Hu, Y. Y.; Rawal, A.; Schmidt-Rohr, K. Strongly bound citrate stabilizes the apatite nanocrystals in bone. *Proceedings of the National Academy of Sciences of the United States of America* **2010**, *107* (52), 22425-22429. DOI: 10.1073/pnas.1009219107.

[157] Mann, K. G.; Whelihan, M. F.; Butenas, S.; Orfeo, T. Citrate anticoagulation and the dynamics of thrombin generation. *Journal of Thrombosis and Haemostasis* **2007**, *5* (10), 2055-2061. DOI: 10.1111/j.1538-7836.2007.02710.x.

[158] Amans, D.; Malaterre, C.; Diouf, M.; Mancini, C.; Chaput, F.; Ledoux, G.; Breton, G.; Guillin, Y.; Dujardin, C.; Masenelli-Varlot, K.; et al. Synthesis of Oxide Nanoparticles by Pulsed Laser Ablation in Liquids Containing a Complexing Molecule: Impact on Size Distributions and Prepared Phases. *Journal of Physical Chemistry C* **2011**, *115* (12), 5131-5139. DOI: 10.1021/jp109387e.

[159] Nara, M.; Tanokura, M. Infrared spectroscopic study of the metal-coordination structures of calcium-binding proteins. *Biochemical and Biophysical Research Communications* **2008**, *369* (1), 225-239. DOI: 10.1016/j.bbrc.2007.11.188.

[160] Oomens, J.; Steill, J. D. Free carboxylate stretching modes. *Journal of Physical Chemistry A* **2008**, *112* (15), 3281-3283. DOI: 10.1021/jp801806e.